

ELECTRIC FORCE MICROSCOPY OF CHARGE
TRAPPING IN THIN-FILM PENTACENE
TRANSISTORS

A Dissertation

Presented to the Faculty of the Graduate School

of Cornell University

in Partial Fulfillment of the Requirements for the Degree of

Doctor of Philosophy

by

Erik Matthew Muller

August 2005

© 2005 Erik Matthew Muller

ALL RIGHTS RESERVED

ELECTRIC FORCE MICROSCOPY OF CHARGE TRAPPING IN THIN-FILM PENTACENE TRANSISTORS

Erik Matthew Muller, Ph.D.

Cornell University 2005

Charge trapping in pentacene thin film transistors is investigated using electric force microscopy. The observed spatial distribution of trapped charge strongly suggests that charge traps not correlated with grain boundaries as expected.

Pentacene is a cyclic aromatic hydrocarbon that forms a well-ordered polycrystalline material in the thin film phase. Pentacene has shown some of the highest mobilities of any organic semiconductor. Hole mobility is thought to be limited by charge trapping. The origin of charge trapping, whether a bulk phenomenon or associated with grain boundaries, is poorly understood.

Thin-film field-effect transistors using thermally deposited pentacene were fabricated and studied using a custom built electric force microscope. The design, construction and performance of the microscope is presented.

The microscope is capable of both contact and non-contact imaging modes for atomic force microscopy. Electrical measurements are made in non-contact mode utilizing frequency shift detection (dynamic mode). Theory describing the interaction between a metal-coated cantilever and an organic semiconductor is presented.

Imaging the spatial distribution of the charge density in a thin-film pentacene transistor showed the trapping of long-lived traps are not homogeneous and not

confined to the grain boundaries. Efforts to make ultrathin pentacene transistors is presented to further determine the role of the grain boundaries in charge trapping.

BIOGRAPHICAL SKETCH

Erik Matthew Muller was born on October 24, 1976 in Bellflower, California. He graduated from Valley Christian High School in 1994. Staying in Southern California, he completed his undergraduate studies at the University of California, San Diego where he earned his Bachelor of Science degree in Physics in 1998. Erik's undergraduate research included the study of the magnetic properties of thin films with Professor Frances Hellman.

Erik decided to enter the physics graduate program at Cornell University, where he quickly experienced a dramatic change in climate. There, he joined the group of Professor John Marohn in the Department of Chemistry and Chemical Biology in early 2001 as Professor Marohn's third graduate student. His doctoral research was conducted under the the guidance of Professor Marohn, his advisor, Professor Dan Ralph (Physics), the chair of his special committee, Professor Paul McEuen (Physics), and Professor Tomás Arias (Physics). He completed his Ph.D. in physics in August 2005.

To my family
for their unconditional love and support

ACKNOWLEDGEMENTS

I would like to express my sincere gratitude to Professor John Marohn for his guidance and support, and for making doctoral education both fun and challenging. I would also like to thank my committee, Professor D. Ralph, Professor P. McEuen and Professor T. Arias for their insights and support.

I am also very grateful to the Department of Chemistry and Chemical Biology and the Physics Department for funding this research.

I would like to thank Bill Silveira for his dedication and help towards designing and building the microscope. Without his talents much of this work would not be possible. Thanks to all of the Marohn Group, Sean Garner, Neil Jenkins, Tina Ng, Seppe Kuehn, Jahan Dawlaty and Michael Jaquith – you have created a great atmosphere, in which to conduct research and were always willing to help.

Many thanks to Professor George Malliaras and the members of his group, particularly, Dr. Ricardo Ruiz and Yunjia Zhang, for their useful discussions and assistance with samples. I would also like to thank Michael Woodside, Markus Brink and Jun Zhu for making discussions about electric force microscopy fun and sometimes funny. Robert Snedeker was an invaluable resource during the design and construction of the microscope and I am truly grateful for his help.

Finally, I would like to thank my family for their unconditional love and support: My mom, Brigit, who is always willing to proof read despite not knowing what she is reading about; my dad, Carl, who is always making sure my computer is as fast as can be; my sister, Amy, who supports me despite my dorkiness; and my wife, Yizhi, who is always at my side (sometimes with a biscuit).

TABLE OF CONTENTS

1	Introduction	1
1.1	Organic Electronic Materials	5
1.2	Charge Trapping	8
1.3	Microscopic characterization of organic electronic materials	13
	References	13
2	Pentacene - Description, Transistors and Performance	18
2.1	The pentacene molecule	18
2.2	Thin-film Transistor	19
2.3	Substrates	23
2.4	Deposition	29
2.5	Characterization	32
	References	38
3	Electric Force Microscopy	40
3.1	Introduction to Electric Force Microscopy	40
3.2	Charge Trapping in EFM	41
3.2.1	Metal Plates	42
3.2.2	Organic Device with Two Co-planar Electrodes	44
3.2.3	Organic Field-Effect Transistor with Trapped Charge	47
3.2.4	Nonuniform Distribution of Trapped Charge	51
3.2.5	Deviations from the Parallel Plate Geometry	53
3.3	Cantilever Response to Thermal Fluctuations	54
3.4	The Electric Force Microscope – Components Overview	59
3.5	EFM - Peripheral Components	60
3.5.1	Vibration Isolation	60
3.5.2	Electrical Connections and Wiring	63
3.5.3	Vacuum System	65
3.5.4	Cryogenic System	65
3.5.5	Computer Systems, GPIB and Data Acquisition	66
3.6	EFM - Core Components	67
3.6.1	Probe	67
3.6.2	Fiber Optic Interferometer	67
3.6.3	Frequency Shift Detection	85
3.6.4	Coarse Approach	91
3.6.5	Scanning	94
3.6.6	Cantilever	95
3.7	Measurement Techniques	96
	References	99

4	Charge Trap Experiments	102
4.1	Sample Description	102
4.2	EFM - Trap Detection Protocol	105
4.3	Trap Imaging I	106
4.4	Trap Imaging II	109
4.5	Trap Density	110
	References	117
5	Ultrathin Pentacene Transistors and Future Directions	119
	References	125
A	Bottom Contact Recipe	126
B	Shadow Mask Recipe	129

LIST OF FIGURES

1.1	Number of pentacene transistor journal articles	2
1.2	Organic thin film transistor	4
1.3	The three categories of organic electronic materials.	6
1.4	Bias stress current decay in a pentacene transistor.	9
2.1	The pentacene molecule	19
2.2	Impurity defects in pentacene	20
2.3	Introduction to thin-film transistors	20
2.4	Bottom contact fabrication process	24
2.5	Oxide quality comparison	26
2.6	Transistor substrate wafer layout	28
2.7	Effects of cleaning with pirana	31
2.8	Pentacene topography over metal and SiO ₂	33
2.9	Current-voltage characteristics for a standard pentacene thin film transistor	35
2.10	Pentacene topography over metal and SiO ₂	36
2.11	Current-voltage characteristics for an interdigitated pentacene thin film transistor	37
3.1	Cantilever/sample models	42
3.2	Cantilever/trapped charge models	48
3.3	Block diagram for the electric including all the support instrumentation	60
3.4	Picture of the EFM	61
3.5	Top plate and probe mount	62
3.6	Power spectrum of room vibrations	63
3.7	Vacuum can	68
3.8	Picture of the probe head	69
3.9	Fiber optic interferometer block diagram	71
3.10	Representation of the light lost due to the escape angle out of the optical fiber	74
3.11	Phasor diagram for the interference pattern from the fiber-optic interferometer	77
3.12	Plot of the theoretical interferometer output	79
3.13	Plot of the experimental interferometer output	80
3.14	RF injection effects on spectral density	81
3.15	RF injection power and frequency dependence	83
3.16	Interferometer summary	84
3.17	Cantilever response to drive piezo	86
3.18	Analog frequency demodulation circuit	87
3.19	Positive feedback filter	88
3.20	Sensitivity of analog frequency demodulation	89

3.21	Analog Phase-locked Loop Drift	90
3.22	Frequency jitter	91
3.23	Coarse approach mechanism	92
3.24	SEM pictures of cantilever tips	95
3.25	Cantilever resonance frequency versus tip-Sample Voltage	97
3.26	Sample tilt correction circuit	98
4.1	Experimental setup and topography	103
4.2	Simple model of tip sample interaction	106
4.3	Trap imaging protocol 1	107
4.4	Trap imaging I protocol	108
4.5	Shielding	108
4.6	Trap imaging protocol II	109
4.7	EFM images of charge trapping	111
4.8	Trap density linescans	112
4.9	Traps density histograms	114
4.10	Summary table of trapping theories	115
5.1	Pentacene islands	121
5.2	Shadow masks diagram	122
5.3	Shadow mask result	122
5.4	Current-voltage characteristics for a top contact pentacene thin film transistor	123

CHAPTER 1

INTRODUCTION

Organic electronic materials have been promoted for use in low-cost novel devices that are otherwise not possible using inorganic semiconductors, such as smart tags or large-area and/or flexible displays [1,2]. Organic electronic materials have been known for a long time [3,4], but they have only recently been used in products commercially available and have been mostly in the form of organic light-emitting diode displays, but not at a promised low cost. The recent surge in commercially available products is mostly due to advances in chemical synthesis [5,6]. The commercial appeal of organic electronic devices is the potential to develop low-cost novel applications that are not otherwise suitable for crystalline inorganic semiconductors such as silicon or gallium arsenide. Among these devices are high-efficiency light emitting diodes [7–10], solar cells [11,12], large-area displays and solution-processable thin-film transistors [8,13–20].

Pentacene, a model organic semiconductor, rivals amorphous silicon in mobility and is compatible with plastic flexible substrates. However, the commercialization of pentacene-based devices is challenging because it is sensitive to air and moisture and it is not solution processable. Its high mobility, reported to be upwards of $3 \text{ cm}^2/\text{Vs}$ [24], has placed it in a dominant position for scientific study in search of the fundamental mechanisms determining its performance. Fig. 1.1 shows the number of journal articles per year that refer to pentacene transistors according to the Inspec database. Plotted on the right of Fig. 1.1 is the highest reported mobility in pentacene for that year. The first use of pentacene in a thin film field effect transistor [21] yielded a hole mobility of $0.002 \text{ cm}^2/\text{Vs}$ which is hardly noteworthy and is perhaps the reason the next article did not appear until several

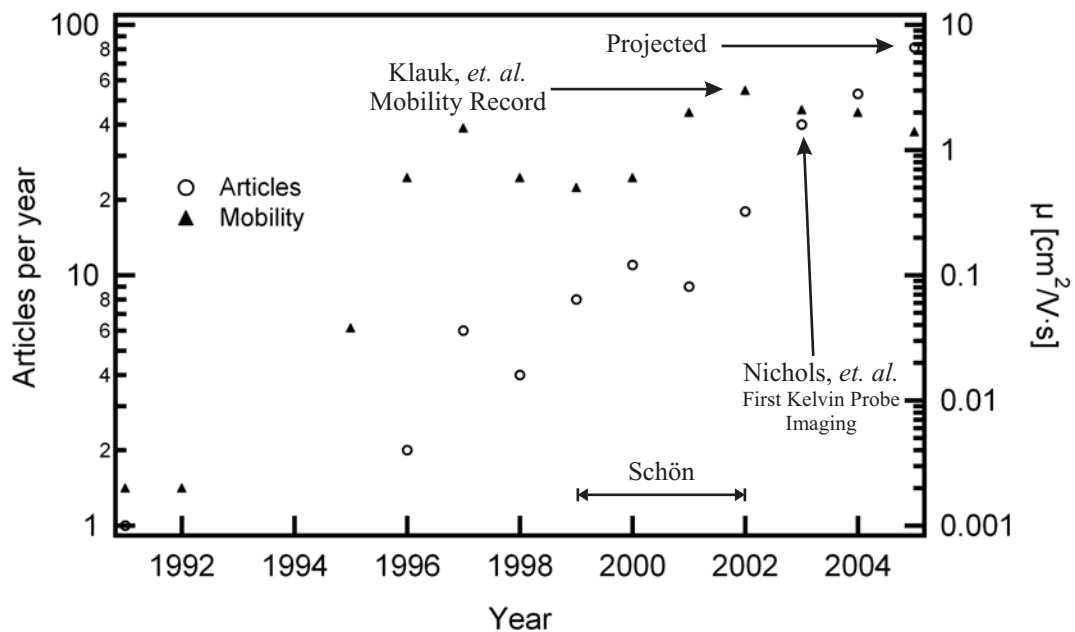


Figure 1.1: The total number of journal articles mentioning pentacene transistors per year according to the Inspec search engine. The highest reported mobility in each year is plotted on the right axis. The mobility record was placed in 2002 by Klauk *et. al.* at $3 \text{ cm}^2/\text{Vs}$. The year 2005 is a projected number; the current number of articles reporting on Inspec is 27.

years later. In 1996, two articles appeared that improved on the mobility to an extent which thrust pentacene into the forefront of organic electronic materials. The reported mobilities of $0.038 \text{ cm}^2/\text{Vs}$ [22] and $0.6 \text{ cm}^2/\text{Vs}$ [23] were attributed to a highly ordered morphology. From this point on, the amount of research studying pentacene transistors skyrocketed (note the log scale in Fig. 1.1). All of this work has not significantly increased the mobility from the initial jump in 1996. The current record for the hole mobility of $3 \text{ cm}^2/\text{Vs}$ was seen by Klauk, *et. al.* [24] which is near the estimated theoretical limit for pentacene at around $10 \text{ cm}^2/\text{Vs}$ [25]. Determining the theoretical limit for the mobility in pentacene is difficult because transport mechanism is not well understood [26–28].

The motivation to study pentacene is not derived from chasing the mobility record but to understand how to maintain the device performance in real-world conditions. Pentacene is a model compound for studying charge trapping because it has a well defined chemical structure and forms well ordered films. This requires a detailed microscopic understanding of charge trapping, charge transport and contact effects in device-grade materials. Fig. 1.2 illustrates the issues important in optimizing organic based thin-film transistors.

The mobility of holes through the accumulation layer of the transistor *and* the contacts determine the amount of current carried by the transistor. Because of the irreproducibility of organic based devices [29], separating contact and bulk effects from current voltage measurements is challenging and typically not done. As a result, bulk current voltage measurements typically underestimate the mobility of holes in the bulk if there is a large contact resistance.

For a polycrystalline material, such as the thin-film form of pentacene, there can be similar resistance barriers between grain boundaries which adversely affect

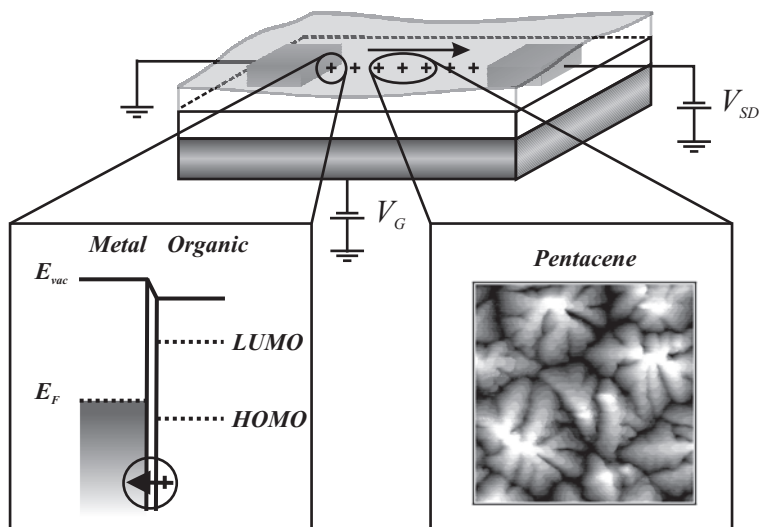


Figure 1.2: Organic thin-film transistor. Applying a voltage to the gate electrode generates an electric field across the insulator which can either accumulate or deplete charges from the semiconductor-insulator interface. The formation of this charged channel allows current to flow from a source to a drain electrode; the gate voltage switches the channel open or closed. The performance of the transistor depends on charge injection, which is determined by energy level alignment and is affected by interface dipoles (left box), as well as on charge flow through the polycrystalline pentacene film (right box; $1\ \mu\text{m} \times 1\ \mu\text{m}$ image).

the mobility (see right box of Fig. 1.2). These barriers are thought to manifest themselves as charge traps and there is a debate in the scientific community as to their origin and correlation with grain boundaries. The association with grain boundaries arises from the phenomenological observation that the mobility in some organic materials depends on crystallite grain size [30–34]. However, many other factors are also associated with effects on mobility such as substrate roughness [33, 34], exposure to oxygen and moisture [35, 36], and pentacene purity [37]. The sensitivity of thin-film transistors to oxygen, moisture and pentacene purity point to a bulk effect, chemically changing the pentacene molecule creating charge traps. This type of degradation could also be associated with grain boundaries if the grain boundaries are more reactive than the rest of the film.

This thesis describes the development, construction and utilization of an electric force microscope, capable of observing charge, voltage and capacitance to image the charge trap distribution locally and determine the correlation, if any, to the pentacene topography in a thin film transistor.

This chapter will proceed with a short introduction to organic electronic materials followed by a description of charge trapping in pentacene thin film transistors.

1.1 Organic Electronic Materials

The interesting electronic behavior of many organic molecules arises from a delocalization, or conjugation, of the π electrons over the entire molecule. From a practical standpoint, this just means there is an alternating single and double bonds along the carbon backbone of the molecule. Organic electronic materials made from such molecules generally fall into one of three categories shown in Fig. 1.3.

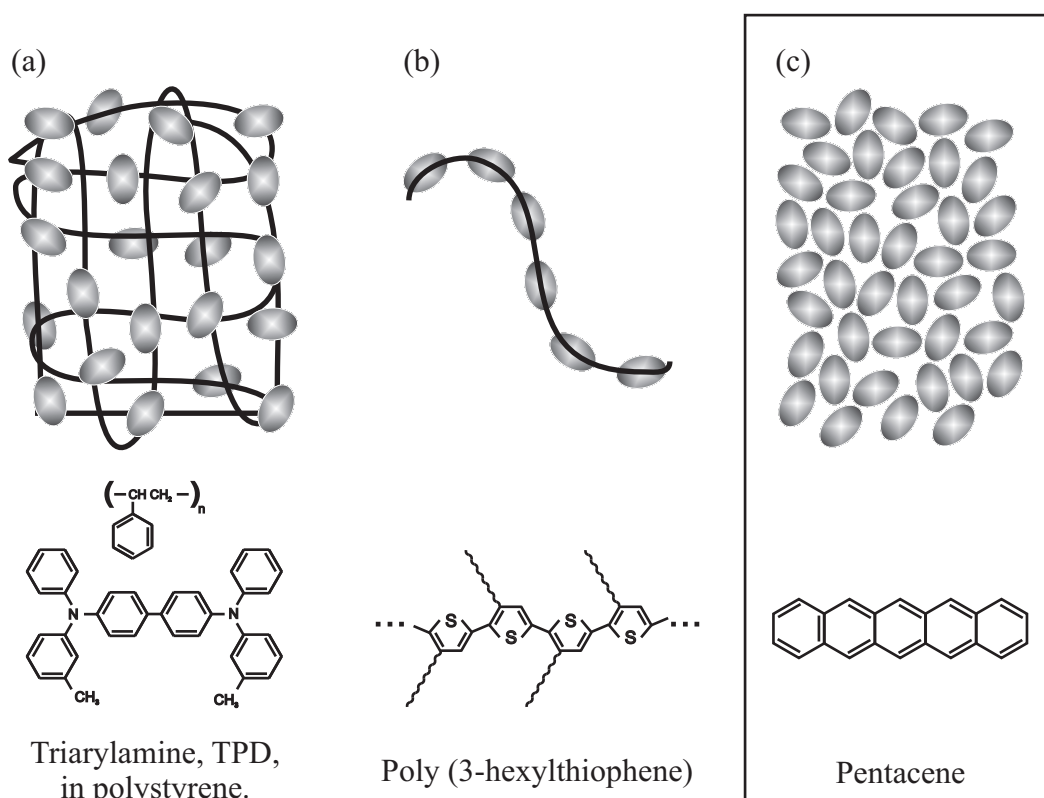


Figure 1.3: (a) Molecularly doped polymer system, (b) polymer system and (c) small molecules

The first category is called molecularly doped (or dispersed) polymers where small conjugated organic molecules are dispersed in an insulating polymer host such as polystyrene. Conduction occurs through thermally assisted tunneling between neighboring conjugated molecules. Tuning the concentration of conjugated molecules varies the average distance between molecules greatly affecting the mobility, up to 8 orders of magnitude. The model system for this type of organic material are TPD molecules dispersed in an insulating polymer host. TPD is a well studied material and has been commercially used in xerography for many years. These materials have most of the favorable characteristics associated with organic semiconductors, namely that they are solution processable and compatible with flexible substrates. However, their mobilities tend to be quite low – in the range of $10^{-10} - 10^{-4} \text{ cm}^2/\text{Vs}$ [4].

The second category is simply called polymers. These polymers, such as polythiophene, have a conjugated backbone where the conjugation length can be chemically tuned by adding non-conjugated side chains or spacers causing an interruption in the conjugation. Oligomers of these polymers also fall into this category. This is the ideal system for chemists because it is solution processable and the electronic/optical properties can be readily tuned using chemical synthesis [6]. However, conjugated polymer systems are plagued with low mobilities without going to great lengths in purification and/or doping. Many of these materials can be spin-cast to form devices.

Pentacene falls into the third category of organic materials called small molecules. The conjugated molecules are typically evaporated or sublimed onto substrates forming polycrystalline thin films. These materials can be highly purified and yield some of the highest mobilities. High mobility devices made of these

materials cannot be spin-cast from solution as good crystals typically do not form. There has been many efforts to make pentacene soluble [38], however the mobilities are not quite as good as the thermally evaporated pentacene. More specific information relating to the growth and performance of pentacene thin-film transistors will be discussed in Chapter 2.

1.2 Charge Trapping

An unspoken consensus seemed to have developed in the community of scientists studying pentacene that the charge trapping occurs mostly at grain boundaries—despite most of the evidence being circumstantial. The observation in oligothiophenes that the mobility is dependent on grain size strongly suggests that the number of grain boundaries plays an important role in determining the mobility [39,40]. In fact, grain boundaries are often invoked in introductory and concluding paragraphs as a source of charge trapping [41–47]. The observation that the electrical performance of pentacene thin-film transistors is dependent on humidity [35, 48] and purity [37] may also suggest a creation of traps within the grain boundaries. The idea of bias stress and its origin is the topic of much research which will be summarized below.

The signature of bias stress is a slow decrease in the source-drain current when the device remains on for an extended time. This has been observed in polymer systems [49] as well as in pentacene, as shown in Fig. 1.4. The most noticeable feature is that the decay times are very long as charge slowly gets trapped inside the device. The source of these charge traps can be states inside the gate dielectric layer, the pentacene/dielectric interface, or in the pentacene film itself. Bias stress in pentacene typically refers to a slow structural or electrical change induced by

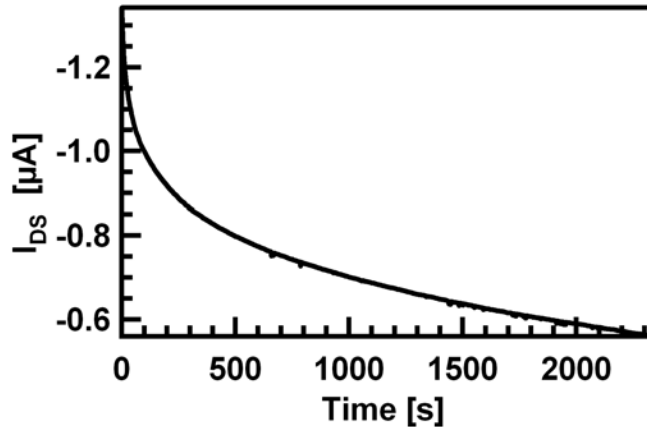


Figure 1.4: A plot of the bias stress current decay with time in a pentacene thin film transistor. Source drain current through a 50 nm thick pentacene transistor with $I_{SD} = -80$ V and $V_G = -60$ V is plotted versus time. $t = 0$ immediately following the application of the gate voltage.

the charge carriers creating traps within the semiconductor.

The findings of Street *et. al.* [50] support a bipolaron mechanism that is responsible for the trap states induced by bias stress in poly(9-9'-dioctyl-flourene-co-bithiophene)(F8T2). Their studies compared the bias stress current using two different gate dielectrics with vastly different trap densities enabling them to rule out states in the dielectric as a source for stress effects. Additionally, the application of light reversed the stress effects, thereby eliminating the possibility of slow structural changes which would typically require annealing to reverse. The observation of a bipolaron mechanism in F8T2 sets a precedent in organic materials.

Bipolaron formation is the combination of two holes, h to form a bipolaron, $(hh)_{BP}$,



From this reaction, a rate equation for the hole concentration, N_h can be formed,

$$\frac{dN_h}{dt} = -kN_h^2 + bN_{BP} \quad (1.2)$$

where k and b are rate constants and the second term on the right is from the breakup of a bipolaron into two holes. All of the data measuring dN_h/dt fit to Eq. 1.2, providing strong evidence for a bipolaron trapping mechanism. In addition, elimination of stress effects by the application of light is consistent with optically excited charge carriers which can neutralize the metastable bipolaron.

A possible origin for bipolarons in pentacene was suggested by Northup and Chabinye [28], although not experimentally observed. Using *ab initio* gas-phase calculations they determined the effect of hydrogen- and oxygen-induced defect states in pentacene. Gap states are introduced by removing one of the double bonds in the central benzene ring to participate in bonding with other atoms. One such defect would be to form $C_{22}H_{15}$ by the addition of a hydrogen atom to the central carbon. Another defect results from the addition of an -OH group to one of the central carbons, forming $C_{22}H_{15}O$. Both of these defects remove one of the p_z orbitals from participating in the conjugation of the pentacene molecule. The dissociation of H_2O can result in both of these two defects and may explain the sensitivity of pentacene to humidity. When these defects were introduced into the crystal structure of pentacene they led to charge defects and hole trapping sites in the presence of an external electric field.

Tsipser and Soos [27], present a theoretical description of how each pentacene's local dielectric environment affects the energy levels of that pentacene molecule. They calculated how the energy of an isolated pentacene cation compares to a pentacene cation surrounded by a dielectric material. A rough approximation can be made by considering the polarization energy of a pentacene cation surrounded

by neutral pentacene molecules having a relative dielectric constant of ϵ_r . This is compared to the energy of an isolated pentacene cation.

The energy density is given by

$$dU = \frac{1}{2} \mathbf{D} \cdot \mathbf{E} dV \quad (1.3)$$

where dV is a differential volume element, \mathbf{D} , is the electric displacement vector, and \mathbf{E} is the electric field. The electric field outside the pentacene molecule is

$$\mathbf{E} = \frac{q}{4\pi\epsilon} \frac{1}{r^2} \hat{r} \quad (1.4)$$

The energy stored in the dielectric material can be calculated by substituting $dV = 4\pi r^2 dr$ and $\mathbf{D} = \epsilon \mathbf{E}$, then integrating from the edge of the pentacene molecule to infinity

$$U(\epsilon) = \frac{q}{4\pi\epsilon} \int_R^\infty \frac{1}{r^2} dr = \frac{q^2}{2R} \frac{1}{4\pi\epsilon} \quad (1.5)$$

Subtracting off the energy of the system with no dielectric present will give the polarization energy

$$P = U(\epsilon) - U(\epsilon_0) = \frac{q^2}{2R} \frac{1}{4\pi} \left(\frac{1}{\epsilon} - \frac{1}{\epsilon_0} \right) \quad (1.6)$$

Introducing the dielectric constant, $\kappa = \epsilon_r = \epsilon/\epsilon_0$ and by dividing by the charge, the polarization energy can be written in units of voltage

$$P_{\pm} = \frac{q}{2R} \frac{1}{4\pi} \left(1 - \frac{1}{\kappa} \right) \quad (1.7)$$

The dielectric constant for pentacene is $\kappa \sim 3$. An effective size of the pentacene molecule is estimated from the lattice vectors

$$\mathbf{a} = (7.900, 0.000, 0.000) \quad (1.8)$$

$$\mathbf{b} = (0.4444, 6.044, 0.000) \quad (1.9)$$

$$\mathbf{c} = (-6.153, -2.858, 14.502) \quad (1.10)$$

The volume of the unit cell is given by

$$V_{\text{cell}} = \mathbf{a} \cdot (\mathbf{b} \times \mathbf{c}) = 6.924 \times 10^{-28} \text{ m}^3 \quad (1.11)$$

There are two pentacene molecules per unit cell, so the effective diameter of one pentacene molecule can be found as

$$D \approx \left(\frac{V_{\text{cell}}}{2} \right)^{1/3} = 7.02 \times 10^{-10} \text{ m} \quad (1.12)$$

Using $R = D/2$, the polarization, in terms of voltage is found to be

$$P_{\pm} = 1.37 \text{ V} \quad (1.13)$$

This is roughly the same value of $P_{\pm} = 1.00\text{V}$ calculated by Tsiper and Soos. Their calculation also shows that the polarization energy in the bulk varies about 10% compared to the polarization energy at surfaces or interfaces. This suggests the $\simeq 100\text{mV}$ deep traps might easily occur at surfaces and interfaces due to variations in dielectric constant alone. The picture to be drawn from this analysis is not that a mobile hole must pay a cost of 1.37 eV to move from one pentacene molecule to the next, but that the mobile hole moves between pentacene molecules and must drag this polarization with it. A trap can occur if the dielectric environments differ significantly creating a large barrier to the hole moving.

It is difficult to discern among these different hypotheses with bulk measurements. Perhaps grain boundaries are more susceptible to these types of defects or these defects could be bulk phenomena. This provides solid motivation to study pentacene devices microscopically by directly imaging the spatial distribution of charge traps.

1.3 Microscopic characterization of organic electronic materials

The inability of bulk measurement techniques to definitively determine the location of the charge traps has led to the need for a microscopic technique that is sensitive to charge and compatible with these materials. Many microscopic techniques have been employed to study organic electronic materials including electric force microscopy (EFM), conducting probe atomic force microscopy (CP-AFM), near-field scanning optical microscopy (NSOM), and scanning tunneling microscopy (STM). High vacuum EFM is the only technique that is capable of imaging charge, potential and capacitance directly in a working device. By working in vacuum, the sensitivity is increased and provides an environment free of much of the oxygen and water which degrade organic based devices.

Chapter 3 will cover in detail the microscope built to investigate charge trapping in pentacene. Pentacene thin film transistors and their experimental development are discussed in the next chapter.

References

- [1] A. R. Völkel, R. A. Street, and D. Knipp, “Carrier transport and density of state distributions in pentacene transistors,” *Phys. Rev. B*, vol. 66, no. 19, pp. 347–355, 2002.
- [2] S. R. Forrest, “The path to ubiquitous and low-cost organic electronic appliances on plastic,” *Nature*, vol. 428, pp. 911–918, 2004.
- [3] M. Pope and C. E. Swenberg, *Electronic Processes in Organic Crystals*, vol. 39. New York: Oxford University Press, 1982.
- [4] P. M. Borsenberger and D. S. Weiss, *Organic Photoreceptors for Xerography*. New York: Marcel Dekker, Inc., 1998.

- [5] R. D. McCullough, R. D. Lowe, S. Tristram-Nagle, M. Jayaraman, D. L. Anderson, and P. C. Ewbank, "Design and control of conducting polymer architectures: Synthesis and properties of regiochemically well-defined poly(3-alkylthiophenes)," *Synth. Met.*, vol. 55, pp. 1198–1203, 1993.
- [6] U. Mitschke and P. Bauerle, "The electroluminescence of organic materials," *J. Mater. Chem.*, vol. 10, no. 7, pp. 1471–1507, 2000.
- [7] J. H. Burroughes, D. D. C. Bradley, A. R. Brown, R. N. Marks, K. Mackay, R. H. Friend, P. L. Burns, and A. B. Holmes, "Light emitting diodes based on conjugated polymers," *Nature*, vol. 347, pp. 539–541, 1990.
- [8] H. Sirringhaus, N. Tessler, and R. H. Friend, "Integrated optoelectronic devices based on conjugated polymers," *Science*, vol. 280, pp. 1741–1744, 1998.
- [9] R. H. Friend, R. W. Gymer, A. B. Holmes, J. H. Burroughes, R. N. Marks, C. Taliani, D. D. C. Bradley, D. A. D. Santos, J. L. Bredas, M. Logdlund, and W. R. Salaneck, "Electroluminescence in conjugated polymers," *Nature*, vol. 397, no. 6715, pp. 121–128, 1999.
- [10] P. Peumans, A. Yakimov, and S. R. Forrest, "Small molecular weight organic thin-film photodetectors and solar cells," *J. Appl. Phys.*, vol. 93, no. 7, pp. 3693–3723, 2003.
- [11] C. W. Tang, "Two-layer organic photovoltaic cell," *Appl. Phys. Lett.*, vol. 48, no. 2, pp. 183–185, 1986.
- [12] P. Stroehriegl and J. V. Grazulevicius, "Charge-transporting molecular glasses," *Adv. Mater.*, vol. 14, no. 20, pp. 1439–1452, 2002.
- [13] G. Horowitz, X. Pend, D. Fickou, and F. Garnier, "The oligothiophene-based field-effect transistor: How it works and how to improve it," *J. Appl. Phys.*, vol. 67, no. 1, pp. 528–532, 1990.
- [14] A. Dodabalapur, L. Torsi, and H. E. Katz, "Organic transistors: Two dimensional transport and improved electrical characteristics," *Science*, vol. 268, pp. 270–271, 1995.
- [15] A. Dodabalapur, L. Torsi, H. E. Katz, and R. C. Haddon, "Organic heterostructure field-effect transistors," *Science*, vol. 269, pp. 1560–1562, 1995.
- [16] L. Torsi, A. Dodabalapur, L. J. Rothberg, A. W. P. Fung, and H. E. Katz, "Intrinsic transport properties and performance limits of organic field-effect transistors," *Science*, vol. 272, pp. 1462–1464, 1996.
- [17] Z. Bao, A. Dodabalapur, and A. J. Lovinger, "Soluble and processable regioregular poly(3-hexylthiophene) for thin film field-effect transistor applications with high mobility," *Appl. Phys. Lett.*, vol. 69, no. 26, pp. 4108–4110, 1996.

- [18] S. F. Nelson, Y.-Y. Lin, D. J. Gundlach, and T. N. Jackson, "Temperature independent transport in high-mobility pentacene transistors," *Appl. Phys. Lett.*, vol. 72, no. 15, pp. 1854–1856, 1998.
- [19] H. E. Katz and Z. Bao, "The physical chemistry of organic field-effect transistors," *J. Phys. Chem. B*, vol. 104, no. 4, pp. 671–678, 2000.
- [20] C. D. Dimitrakopoulos and P. R. L. Malenfant, "Organic thin film transistors for large area electronics," *Adv. Mater.*, vol. 14, no. 2, pp. 99–117, 2002.
- [21] G. Horowitz, X.-Z. Peng, D. Fichou, and F. Garnier, "Organic thin-film transistors using pi -conjugated oligomers: influence of the chain length," *J. Mol. Electron*, vol. 7, no. 2, pp. 85–9, 1991.
- [22] C. D. Dimitrakopoulos, A. R. Brown, and A. Pomp, "Molecular beam deposited thin films of pentacene for organic field effect transistor applications," *J. Appl. Phys.*, vol. 80, no. 4, pp. 2501–2508, 1996.
- [23] J. G. Laquindanum, H. E. Katz, A. J. Lovinger, and A. Dodabalapur, "Morphological origin of high mobility in pentacene thin-film transistors," *Chem. Mater.*, vol. 8, no. 11, p. 2542, 1996.
- [24] H. Klauk, M. Halik, U. Zschieschang, G. Schmid, W. Radlik, and W. Weber, "High-mobility polymer gate dielectric pentacene thin film transistors," *J. Appl. Phys.*, vol. 92, no. 9, p. 5259, 2002.
- [25] W.-Q. Deng and W. A. Goddard III, "Predictions of hole mobilities in oligoacene organic semiconductors from quantum mechanical calculations," *J. Phys. Chem. B*, vol. 108, no. 25, pp. 8614–8621, 2004.
- [26] J. H. Kang, D. da Silva, J. L. Bredas, and X. Y. Zhu, "Shallow trap states in pentacene thin films from molecular sliding," *Appl. Phys. Lett.*, vol. 86, no. 15, 2005.
- [27] E. V. Tsiper and Z. G. Soos, "Electronic polarization in pentacene crystals and thin films," *Phys. Rev. B*, vol. 68, no. 8, 2003.
- [28] J. E. Northrup and M. L. Chabinyk, "Gap states in organic semiconductors: hydrogen- and oxygen-induced states in pentacene," *Phys. Rev. B*, vol. 68, no. 4, p. 041202, 2003.
- [29] Y. L. Shen, A. R. Hosseini, M. H. Wong, and G. G. Malliaras, "How to make ohmic contacts to organic semiconductors," *ChemPhysChem*, vol. 5, no. 1, pp. 16–25, 2004.
- [30] D. J. Gundlach, Y. Y. Lin, T. N. Jackson, S. F. Nelson, and D. G. Schlom, "Pentacene organic thin-film transistors - molecular ordering and mobility," *IEEE Electr. Device L.*, vol. 18, no. 3, pp. 87–89, 1997.

- [31] Y. Y. Lin, D. J. Gundlach, S. F. Nelson, and T. N. Jackson, "Pentacene-based organic thin-film transistors," *IEEE T. Electron Dev.*, vol. 44, no. 8, pp. 1325–1331, 1997.
- [32] D. J. Gundlach, T. N. Jackson, D. G. Schlom, and S. F. Nelson, "Solvent-induced phase transition in thermally evaporated pentacene films," *Appl. Phys. Lett.*, vol. 74, no. 22, pp. 3302–3304, 1999.
- [33] D. Knipp, R. A. Street, A. Volkel, and J. Ho, "Pentacene thin film transistors on inorganic dielectrics: morphology, structural properties, and electronic transport," *J. Appl. Phys.*, vol. 93, no. 1, pp. 347–355, 2003.
- [34] D. Knipp, R. A. Street, and A. R. Volkel, "Morphology and electronic transport of polycrystalline pentacene thin-film transistors," *Appl. Phys. Lett.*, vol. 82, no. 22, pp. 3907–3909, 2003.
- [35] Z. T. Zhu, J. T. Mason, R. Dieckmann, and G. G. Malliaras, "Humidity sensors based on pentacene thin-film transistors," *Appl. Phys. Lett.*, vol. 81, no. 24, pp. 4643–4645, 2002.
- [36] Y. Qiu, Y. C. Hu, G. F. Dong, L. D. Wang, J. F. Xie, and Y. N. Ma, "H₂O effect on the stability of organic thin-film field-effect transistors," *Appl. Phys. Lett.*, vol. 83, no. 8, pp. 1644–1646, 2003.
- [37] O. D. Jurchescu, J. Baas, and T. T. M. Palstra, "Effect of impurities on the mobility of single crystal pentacene," *Appl. Phys. Lett.*, vol. 84, no. 16, pp. 3061–3063, 2004.
- [38] C. D. Sheraw, T. N. Jackson, D. L. Eaton, and J. E. Anthony, "Functionalized pentacene active layer organic thin-film transistors," *Adv. Mater.*, vol. 15, no. 23, pp. 2009–2011, 2003.
- [39] G. Horowitz and M. E. Hajlaoui, "Mobility in polycrystalline oligothiophene field-effect transistors dependent on grain size," *Adv. Mater.*, vol. 12, no. 14, pp. 1046–1050, 2000.
- [40] G. Horowitz and M. E. Hajlaoui, "Grain size dependent mobility in polycrystalline organic field-effect transistors," *Synth. Met.*, vol. 122, no. 1, pp. 185–189, 2001.
- [41] S. Y. Jung and Z. Yao, "Organic field-effect transistors with single and double pentacene layers," *Appl. Phys. Lett.*, vol. 86, no. 8, 2005.
- [42] D. V. Lang, X. Chi, T. Siegrist, A. M. Sergent, and A. P. Ramirez, "Bias-dependent generation and quenching of defects in pentacene," *Phys. Rev. Lett.*, vol. 93, no. 7, 2004.

- [43] T. Minari, T. Nemoto, and S. Isoda, "Fabrication and characterization of single-grain organic field-effect transistor of pentacene," *J. Appl. Phys.*, vol. 96, no. 1, pp. 769–772, 2004.
- [44] Y. S. Yang and T. Zyung, "Preparation and electronic defect characteristics of pentacene organic field effect transistors," *Macromol. Res.*, vol. 10, no. 2, pp. 75–79, 2002.
- [45] Y. S. Yang, S. H. Kim, J. I. Lee, H. Y. Chu, L. M. Do, H. Lee, J. Oh, T. Zyung, M. K. Ryu, and M. S. Jang, "Deep-level defect characteristics in pentacene organic thin films," *Appl. Phys. Lett.*, vol. 80, no. 9, pp. 1595–1597, 2002.
- [46] L. F. Drummy, C. Kubel, D. Lee, A. White, and D. C. Martin, "Direct imaging of defect structures in pentacene nanocrystals," *Adv. Mater.*, vol. 14, no. 1, pp. 54–57, 2002.
- [47] V. Y. Butko, X. Chi, D. V. Lang, and A. P. Ramirez, "Field-effect transistor on pentacene single crystal," *Appl. Phys. Lett.*, vol. 83, no. 23, pp. 4773–4775, 2003.
- [48] D. W. Li, E. J. Borkent, R. Nortrup, H. Moon, H. Katz, and Z. N. Bao, "Humidity effect on electrical performance of organic thin-film transistors," *Appl. Phys. Lett.*, vol. 86, no. 4, 2005.
- [49] G. Horowitz, R. Hajlaoui, D. Fichou, and A. El Kassmi, "Gate voltage dependent mobility of oligothiophene field-effect transistors," *J. Appl. Phys.*, vol. 85, no. 6, pp. 3202–3206, 1999.
- [50] R. A. Street, A. Salleo, and M. L. Chabinyc, "Bipolaron mechanism for bias-stress effects in polymer transistors," *Phys. Rev. B*, vol. 68, no. 8, p. 085316, 2003.

CHAPTER 2
PENTACENE - DESCRIPTION, TRANSISTORS AND
PERFORMANCE

2.1 The pentacene molecule

The pentacene molecule is an cyclic aromatic hydrocarbon ($C_{22}H_{14}$) that resembles five fused benzene rings. It is highly planar where the p_z orbitals from each of the carbon atoms forms molecular orbital that are delocalized over the entire molecule. The energy difference between the highest occupied molecular orbital (HOMO) and the lowest unoccupied molecular orbital (LUMO) of pentacene films has been reported to be in the range of 2 eV [1, 2]. Fig. 2.1(a) shows the structure of the pentacene molecule along with its dimensions. Fig. 2.1(b) shows the delocalized p_z electrons that extend over the entire molecule. Fig. 2.1(b) is a conceptualization to convey the idea that the electrons are free to move in this region of space.

Pentacene forms a herring-bone arrangement when deposited onto a surface of sufficient quality (low surface roughness, hydrophobic and clean) as shown in Fig. 2.1(c) [3]. It is interesting to note that the typical direction of current flow in electrical devices made from pentacene is not along the length of the molecule. The unit cell has a triclinic basis with two pentacene molecules per unit cell [3]. The interaction between pentacene molecules is mostly due to relatively weak Van der Waals forces. The interaction between molecules plays an important role in understanding the electrical properties, as many of the trapping hypotheses invoke the structural quality of the film. The extent to which structural variations affect the electrical properties is the subject of much theoretical work [4-6].

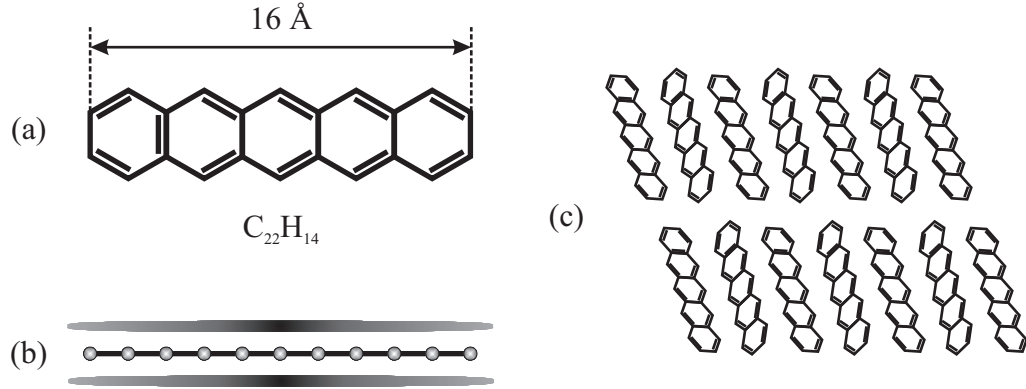


Figure 2.1: (a) The chemical structure of the pentacene molecule, (b) a side view of the pentacene molecule showing the delocalized p_z electrons, and (c) the herring-bone packing arrangement of pentacene molecules in the thin-film phase.

The two center carbon atoms are the most reactive resulting in common forms of impurities in device grade pentacene. Two possible impurities that can be found in pentacene film are shown in Fig. 2.2. The first, shown in Fig. 2.2(a) involves the addition of a hydrogen atom to each of the central carbon atoms. The second, shown in Fig. 2.2(b), involves the addition of an -OH group to the central carbon atoms. Not only do these two impurities break the conjugation by using the p_z orbital, they also remove the planarity of the molecule. It has been shown using high pressure liquid chromatography that pentacene purchased from Aldrich contains a easily measurable amount of 6,13-pentacenequinone, shown in Fig. 2.2 [7].

2.2 Thin-film Transistor

The metal-oxide-semiconductor field effect transistor (MOSFET) is one of the basic components of most modern microelectronics. MOSFETs are well suited to

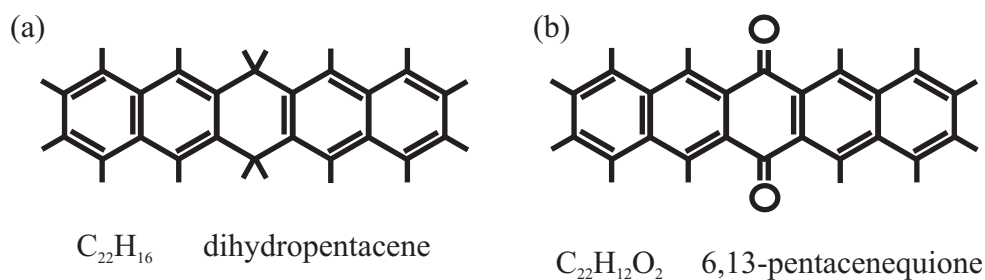


Figure 2.2: Two possible defects causing impurity in pentacene thin films. (a) Dihydropentacene results from an addition of a hydrogen atom to each of the central carbons and (b) 6,13-pentacenequinone results from the addition of an -OH group to both central carbon atoms.

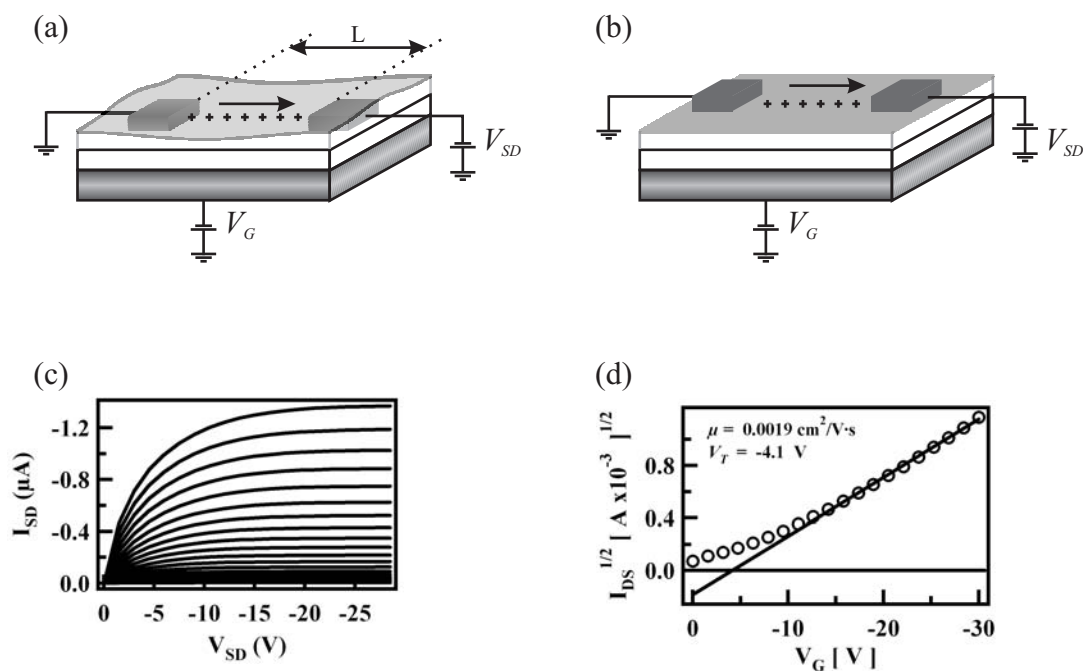


Figure 2.3: Introduction to thin-film transistors. (a) Bottom contact geometry, (b) top contact geometry, (c) current voltage characteristics, and (d) $I_{SD,sat}$ vs. V_G used to determine the mobility.

low conductivity semiconductors such as amorphous silicon and semiconducting organic materials. Amorphous silicon and organics, particularly pentacene, share common values of performance such as the conductivity and mobility. However, a major difference is that amorphous silicon is held together by covalent bonding and organics are held together by weak van der Waals forces. This difference manifests itself as structural changes in the organic due to the presence of charges, i.e. the molecule stretches or contracts due to the breaking of chemical bonds as charge resides on or off the molecule. This small structural change is localized and is called a polaron moving through the organic. Many review articles summarize the operation of MOSFETs using organic materials as their active components [8]. The term organic field effect transistor (OFET) is commonly used to describe MOSFETs that use organic materials.

A MOSFET is essentially a parallel plate capacitor where one plate consists of the charge carriers in the semiconductor and the other plate is a metal gate electrode. The density of charge carriers in the organic is therefore modulated by the gate voltage. Contacts are made to the organic and use the charge carriers to form a conducting channel. Two device geometries commonly used with organics are shown in Fig 2.3. A large electrode is used as a back gate which can be made of heavily doped silicon, conducting polymers [9], or anything conductive. Electrically separating the gate from the semiconductor is a gate insulator or dielectric layer. The source and drain electrodes, as well as the organic, are then deposited on the dielectric layer.

Fig 2.3(a) shows a bottom-contact field effect transistor (BC-FET) configuration where the source and drain electrode are defined before the addition of the organic layer. The main advantage of a BC-FET is that the source and drain

electrodes can be defined using optical or e-beam lithography enabling gap lengths down to 30 nm or smaller [10]. The main disadvantage is that, for many organics, the source and drain electrodes form a poor contact to the organic material [11,12].

Fig 2.3(b) shows a top contact field effect transistor (TC-FET) configuration where the organic is added prior to defining the source and drain electrodes. The advantages/disadvantages of a TC-FET are exactly opposite of those of a BC-FET. Most organics are not compatible with the solvents used in optical and e-beam lithography, requiring an alternate route to define source and drain electrodes. This is usually achieved through shadow masking which limits the device gap to 10 μm or larger – 10 μm devices are very difficult to reliably fabricate. Despite the difficulty in defining the source and drain electrodes, the TC-FET has a huge advantage by making good ohmic contact to most organic materials, particularly pentacene [12].

The electrical properties of an organic MOSFET are described using a similar treatment as with inorganic MOSFET. The main difference is that organic MOSFETs operate through injection of majority charge carriers into the accumulation layer, whereas inorganic MOSFETs typically inject minority carriers into an inversion layer. A plot showing the source-drain current, I_{SD} , versus the source drain voltage, V_{SD} , at various gate voltages, V_G is shown in Fig. 2.3(c). The mobility is determined in the saturation regime according to [8]

$$I_{SD, \text{sat}} = \frac{W}{2L} \mu C_i (V_G - V_T)^2 \quad (2.1)$$

where $I_{SD, \text{sat}}$ is the current at saturation, W is the width of the transistor gap, L is the length of the transistor gap, μ is the hole mobility, C_i is the capacitance per unit area of the gate dielectric. The threshold voltage, V_T accounts for any voltage drops across the gate dielectric or at the insulator/semiconductor interface due to

trapped charge or dipoles.

Fig. 2.3(d) shows the square root of $I_{SD,sat}$ versus V_G . Fitting this plot to Eq. 2.1 yields the hole mobility in the saturation regime and also V_T . The parallel plate geometry makes the determination of C_i quite easy by using the following equation,

$$C_i = \frac{\epsilon_0 \kappa}{d} \quad (2.2)$$

where ϵ_0 is the permittivity of free space, κ is the dielectric constant of the gate dielectric; $\kappa = 3.9$ for SiO_2 . Here, d is the thickness of the gate dielectric which is typically ~ 325 nm for devices used in these experiments. This yields a typical value of C_i :

$$C_i = \frac{(8.85 \times 10^{12} \text{ F} \cdot \text{m}^{-1}) \cdot 3.9}{325 \text{ nm}} = 1.062 \times 10^{-8} \text{ F} \cdot \text{cm}^{-2} \quad (2.3)$$

The next section outlines the fabrication process of making the thin film field effect transistor substrates used in these experiments.

2.3 Substrates

Transistors in both bottom- and top- contact configurations were fabricated for use in these trap imaging experiments. The requirements of our microscope put design limitations on the device geometries which will be addressed throughout this section. Bottom contact device fabrication will be discussed first followed by the fabrication of shadow masks to make top contact devices. All device substrates were fabricated at the Cornell Nanofabrication Facility (CNF).

The development of the bottom-contact recipe has been passed down through a couple of research groups and the specific history is not known. Most of the trap

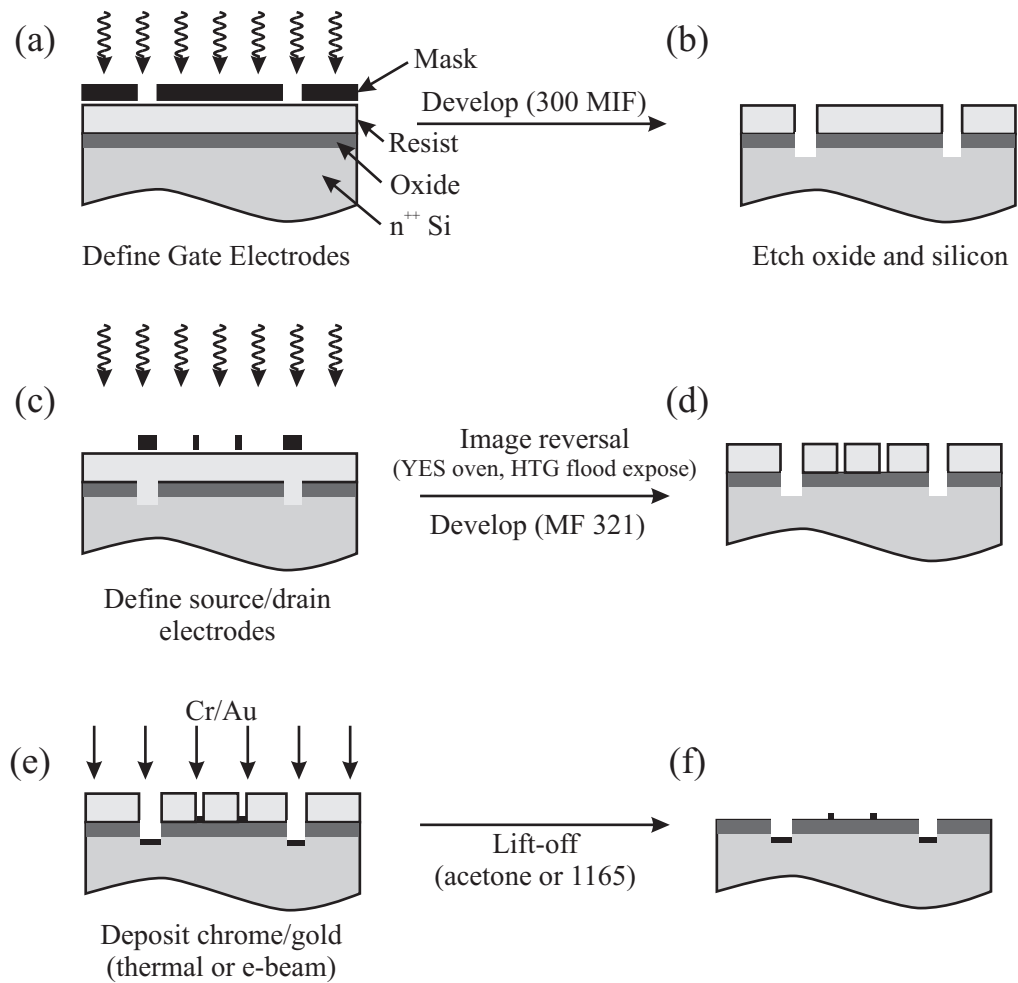


Figure 2.4: The nanofabrication process used to make bottom contact device substrates

imaging experiments were performed using the bottom-contact configuration. The main steps to the fabrication process are outlined in Fig. 2.4.

The fabrication process starts with a commercial prime silicon wafer with low resistivity ($0.001 - 0.005 \Omega \cdot \text{cm}$). The low resistivity silicon is used as the back gate. A thermal oxide is grown to a thickness of $\sim 300 \text{ nm}$ (not shown) using a wet oxidation process at 900°C for 90 min. This layer acts as a good quality dielectric layer insulating the source and drain electrodes from the gate electrode. The oxidation process begins by performing a MOS clean of the wafers which is a specific series of chemicals designed to remove trace metals and organic material prior to placing them in the furnace. The first step in the MOS clean is a base rinse for 10 min in a 10:2:1 solution of H_2O , H_2O_2 and NH_4OH followed by a rinse in deionized (DI) water. The second step is an acid rinse for 10 min in a 10:2:1 solution of H_2O , H_2O_2 and H_2SO_4 followed by a rinse in DI water. The wafers are then considered “MOS Clean” for approximately 6 hours. The wafers can be placed in the furnace anytime during this 6-hour period. About 10 wafers are stacked in the furnace at one time with one additional sacrificial wafer used at each end. The outside wafers do not have good uniformity.

The oxidation step is an arduous task and an attempt to bypass this step by purchasing wafer with oxide already grown on them yielded poor results. The purchased oxide was 200 nm of thermally grown oxide from Silicon Quest. The quality of the oxide was tested by evaporating small gold pads directly on the oxide and increasing the voltage between the gold pad and the gate until there was a failure. The maximum electric field at breakdown of both the Silicon Quest oxide and CNF oxide is $\sim 5 \text{ MV/cm}$ which is consistent with industry standards and previously quoted values [13].

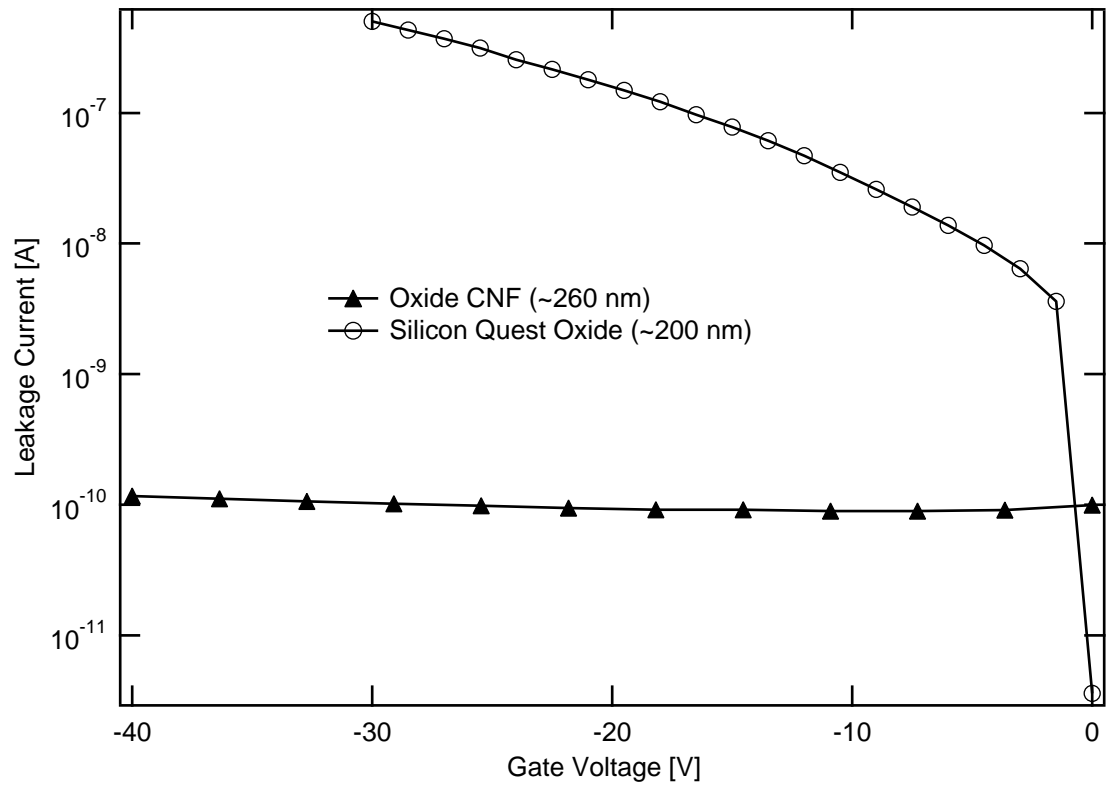


Figure 2.5: The gate leakage current through the gate oxide layer in both Silicon Quest oxide and oxide grown at CNF. The total area through which the current flows is *estimated* as $20 \times 10^{-6} \text{m}^2$

Fig. 2.5 shows the leakage current through both purchased oxide and oxide grown at CNF through contact pads of the same area. Note the log scale. The leakage current through the CNF oxide is flat at 10^{-10} A for the entire range of gate voltages that we use in our experiments. The leakage current through the silicon quest oxide, however, is 2-3 orders of magnitude higher, increasing with the gate voltage. The oxide thickness is different but not enough to account for the large difference in leakage current. Even though using a commercial oxide from Silicon Quest saves a dreaded MOS clean and oxide growth in the transistor fabrication process, the purchased oxide does not perform to a satisfactory standard to be used in our devices.

Contact to the gate from the top of the devices simplifies the experimental setup for use in a probe station or the electric force microscope. The gate electrodes are defined using contact photolithography. The oxide is completely etched away and about 500 nm of silicon is also etched to assure good contact (see Fig. 2.4(a) and Fig. 2.4(b)).

The source and drain electrodes are also defined using contact photolithography with image reversal. The image reversal gives a negatively sloped side profile to the photoresist and is important for lift-off (see Fig. 2.4(c) and Fig. 2.4(d)).

An adhesion layer of chrome, typically 5 nm, and gold, typically 50 nm, is thermally evaporated over the entire wafer at a rate of $0.5 - 1$ Å/s. Lift-off is done in acetone or 1165 remover for at least 4 hours (see Fig. 2.4(e) and Fig. 2.4(f)). The complete recipe is in Appendix A.

The resulting wafer layout, shown in Fig. 2.6(a), allows for twenty-one individual devices to be arranged on a standard 100 mm (4") wafer. Separating the devices can be tricky. The preferred technique is to use a wafer dicer that cuts

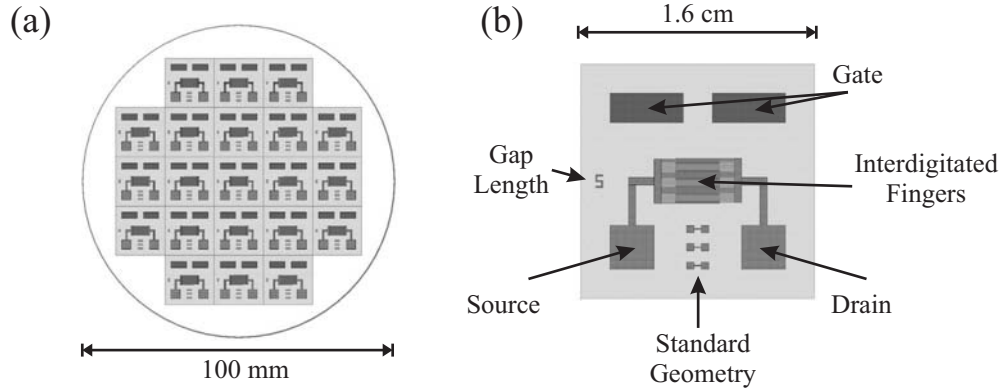


Figure 2.6: (a) The layout of 21 individual devices on a on 4” wafer. (b) The individual parts making up one single device. Each device includes three transistors that are in the standard geometry (i.e. non-interdigitated, W:L ratio = 10)

the individual devices out of the wafer. It is important to protect the devices from scratches and dust by applying a coat of photoresist prior to dicing. An alternate technique (i.e. used when the wafer dicer at CNF is being repaired) is to scribe the wafer and just snap the pieces off. This generally results in breaks right though the center of many devices.

The layout of an individual transistor substrate is shown in Fig. 2.6(b). The requirements of the electric force microscope limit us to substrates that are 1.6 cm or smaller while still enabling access to the electrodes beyond the scan head of the microscope. To achieve this, the source, drain, and gate contacts are brought near the edge of the device. The contacts must also be at least 2 mm away from the edge to avoid unnecessary gate leakage. The very center of the device contains roughly 60 interdigitated gold fingers that make up the source and drain electrodes. This makes the active area approximately 3×3 mm square. The gold fingers are $40\mu\text{m}$ wide resulting in about 70 device gaps. The number of gaps vary slightly

depending on the gap length, L . The large area enables an easier location of a single gap with the electric force microscope. The device substrate includes three transistors that are in the typical configuration, i.e. the gap width to gap length ratio is 10. These are included for the purpose of testing that the interdigitated geometry has similar characteristics as the standard geometry. It is generally true that the standard device performs similarly to the interdigitated device, except that the gate leakage is larger with the interdigitated geometry because of the larger area. The substrates are now ready for pentacene deposition which is described in Sec. 2.4.

Some work was done developing a shadow mask to define top-contact source and drain electrodes. The basic idea is to fabricate two square holes separated by a small beam in a silicon wafer. This beam defines the transistor gap. In this case the pentacene would first be deposited (see Sec. 2.4) onto a clean wafer containing only the oxide layer. The shadow mask is clamped to the device wafer and gold is thermally evaporated through the mask defining the source and drain electrodes. The complete recipe for the shadow mask can be found in Appendix B. The reliability of shadow masking was rather poor and is discussed in detail in chapter 5.

2.4 Deposition

Pentacene was purchased from Aldrich and used without further purification. It is a light- and oxygen-sensitive purple powder that is kept in a dark bottle inside a desiccator when not being used.

Prior to evaporation, the substrates are cleaned by sonication for 10 min in acetone, then 10 min in isopropanol. They are sprayed with acetone and isopropanol

while spinning at 3000 rpm and allowed to dry while still spinning. The last step in the clean process is a 10 min UV-ozone clean. Small variations to this clean procedure have been used and all seem to work similarly – other solvents have been tried such as chloroform and methanol, as well as cleaning them mechanically with soap, water and a swab.

The cleaning procedure cannot include any acid or base because of the presence of the gold electrode in the bottom-contact configuration. However, an attempt to clean the substrates using a Piranha solution was tried on the suggestion of CNF staff and because the cleaning procedure in the previous paragraph does not get the sample perfectly clean as can be seen by the AFM image of a gold electrode in Fig. 2.7(a). The sample was then placed in the Piranha solution for 30 min. The Piranha solution attacked the gold electrode and made the surface extremely clean, but extremely rough.

After cleaning, the substrates were taken immediately to the evaporation chamber and placed under vacuum. The vacuum chamber is allowed to reach a pressure of $\sim 10^{-6}$ torr prior to evaporation. A crucible containing a small amount of pentacene powder is heated to a temperature of $\sim 230^{\circ}\text{C}$, the sublimation temperature of pentacene in vacuum. It is important to heat the pentacene slowly as it tends to spit resulting in an unpredictable sublimation rate and ultimately poor films. A typical deposition rate is $\sim 0.1 \text{ \AA/s}$ or slower. A typical thin-film thickness is $\sim 50\text{nm}$. Under these conditions, polycrystalline grain sizes on the scale of $1 - 3 \mu\text{m}$ can be expected to grow on the SiO_2 . Grain sizes on the gold electrode are always very small, nm typically.

An alternative deposition procedure was followed to achieve larger grain sizes and for the purpose of burning off any remaining water or any organics minimizing

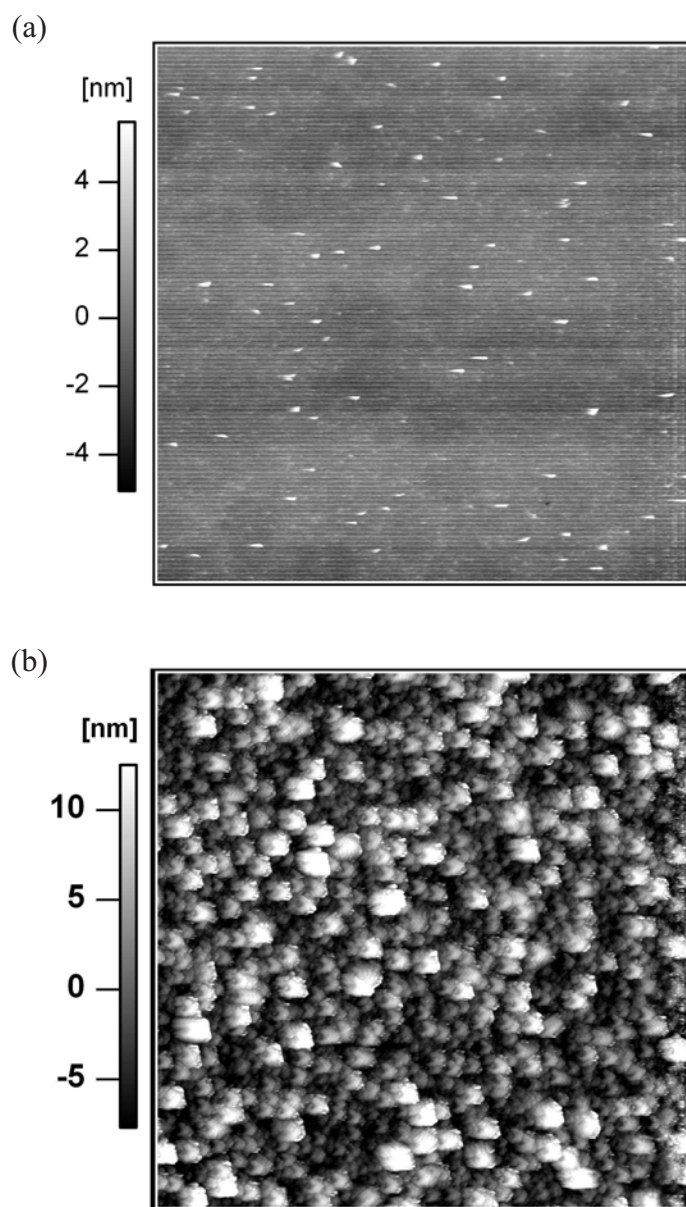


Figure 2.7: (a) Gold electrode prior to cleaning with Piranha solution and (b) the effect of the Piranha solution on the roughness of the gold electrode.

the number of pinning centers. Prior to deposition, that substrate was heated to 180°C then allowed to cool to 60°C. Depositing at an elevated temperature gives the pentacene molecules more kinetic energy, allowing them to sample more of the surface before sticking. It usually takes about 6-8 hours for the substrate to cool since it is under vacuum, providing no place for the heat to dissipate. The deposition is performed holding the substrate at 60°C. This procedure was typically followed when growing the thin 1-4 monolayer films and was required to get island sizes on the scale of 4 – 5 μm .

2.5 Characterization

The first step to understanding what is important about pentacene thin-film transistors as they relate to microscopic studies is to understand their bulk electrical characteristics.

The electrical characterization of the pentacene thin film transistors consists mainly of extracting the mobility from the current voltage characteristics using Eq. 2.1. Almost all of the bottom-contact devices made using our technique yield a mobility in the range of 0.01 – 0.001 cm^2/Vs , which is not uncommon for a bottom contact film with an untreated surface [14].

One of the main goals of this experiment is to understand how the topography is correlated with the trap location. The experiment began with an investigation of the topography to understand its correlation with the trap location. The growth of pentacene is well known to form a polycrystalline film with grain sizes from 200 nm to 20 μm when thermally deposited on SiO_2 [15]. The typical topography of the pentacene film grown for these experiments is shown in Fig. 2.8. Fig. 2.8(a) shows the pentacene film on the gold electrode, which shows much smaller grains

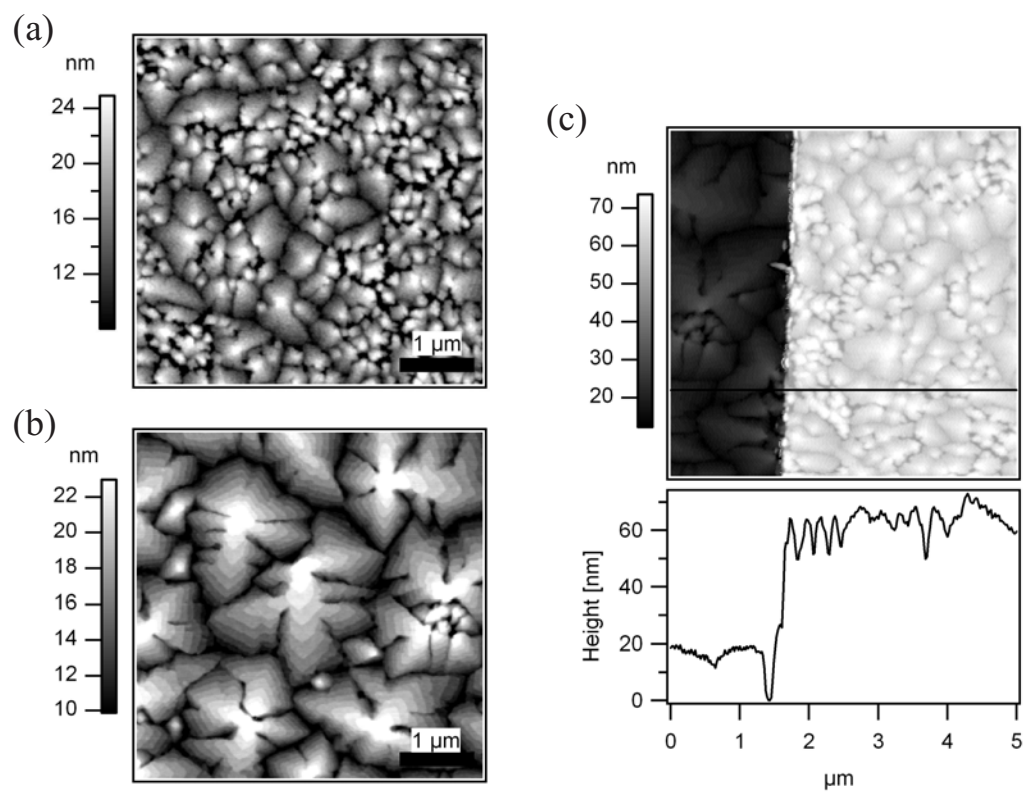


Figure 2.8: (a) Pentacene Topography over metal and (b) over SiO_2 . (c) Topography at the interface between the gold and SiO_2 showing the mismatch in the grain sizes. The line profile shows the height mismatch.

compared to the pentacene grown on the SiO₂ (Fig. 2.8(b)). This mismatch in grain sizes causes a problem at the interface of the contact electrode where the charges must be injected and leads to high contact resistance [12]. Additionally, if the electrodes are not recessed, there is a height mismatch, suggesting implications for injection. Fig. 2.8(c) shows both the height mismatch and the grain size mismatch.

Fig. 2.9 (a) shows the I-V characteristics for a standard non-interdigitated pentacene thin-film transistor. The source-drain current shows good saturation. Near V_{SD} , the low slope of I_{SD} indicates poor contact resistance. The square root of the source-drain current at saturation versus the gate voltage is shown in figure Fig. 2.9(b). The mobility and threshold voltage is calculated using Eq. 2.1 and have values of 0.01 cm²/Vs and -5.1 V respectively.

A procedure for recessing the source and drain electrodes was implemented to both aid in the electric force microscopy imaging (see Chap. 3) and to eliminate the height mismatch mentioned in the previous paragraph. As can be seen from topography and line profile of Fig. 2.10(a), recessing the electrodes did produce a flat device. However, there is still a poor matching of the grain sizes at the contact, which is magnified in Fig. 2.10(b). There even appears to be a small build-up of pentacene on the gold side of the contact interface and a small valley of pentacene on the SiO₂ side of the contact interface.

Fig. 2.11 (a) shows the current-voltage characteristics for an interdigitated pentacene thin-film transistor. The source-drain current shows good saturation. The square root of the source-drain current at saturation versus the gate voltage is shown in figure Fig. 2.11(b). The mobility and threshold voltage is calculated using Eq. 2.1 and have values of 0.012 cm²/Vs and -17 V respectively.

No real noticeable increase or decrease in the device mobility were apparent;

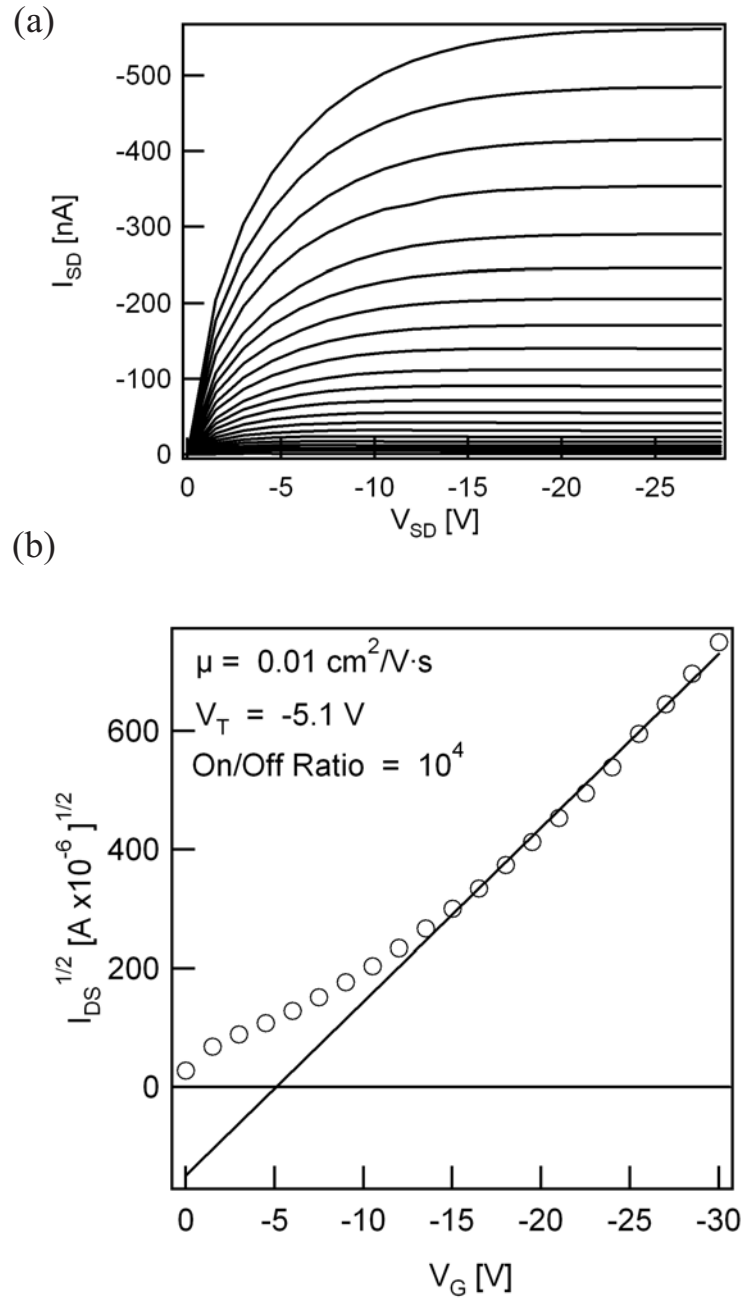


Figure 2.9: (a) Current-voltage characteristics for a pentacene (25 nm thick) thin-film transistor with $W = 600 \mu\text{m}$, $L = 60 \mu\text{m}$ and an oxide thickness of $T = 200 \text{ nm}$. The gate voltage goes from 0 to -30 V in -1.5V steps. (b) The square root of the source-drain current at saturation versus the gate voltage. The mobility, threshold voltage and on/off ratio is calculated from the saturation regime.

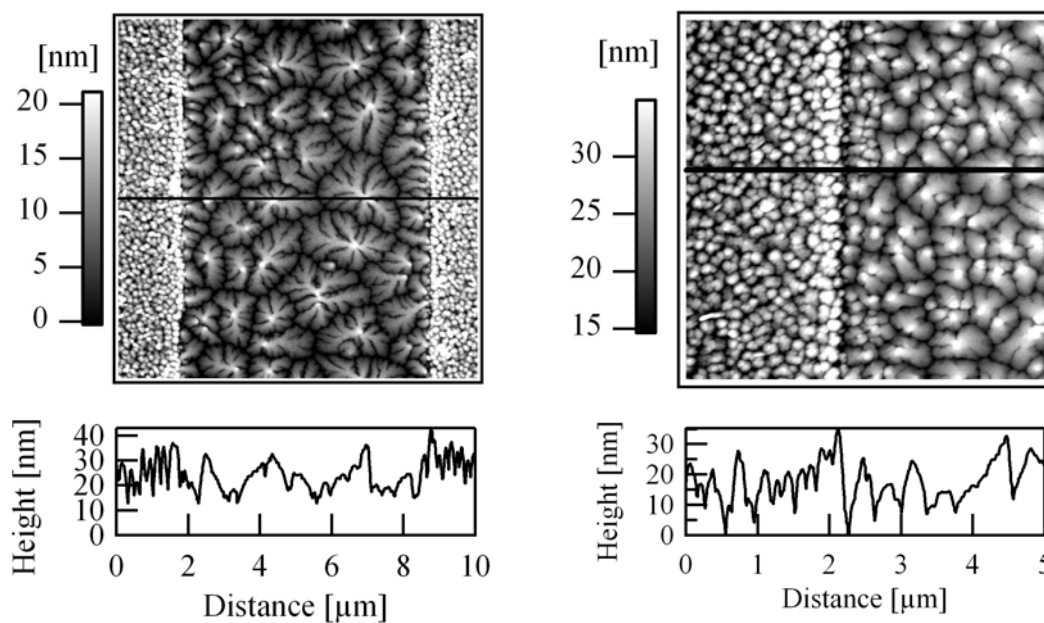


Figure 2.10: Pentacene Topography over the entire transistor gap. The gain size mismatch can be seen at the metal-SiO₂ interface. (b) An enlarged image at the metal-SiO₂ interface showing the buildup of pentacene and many small grains at the interface.

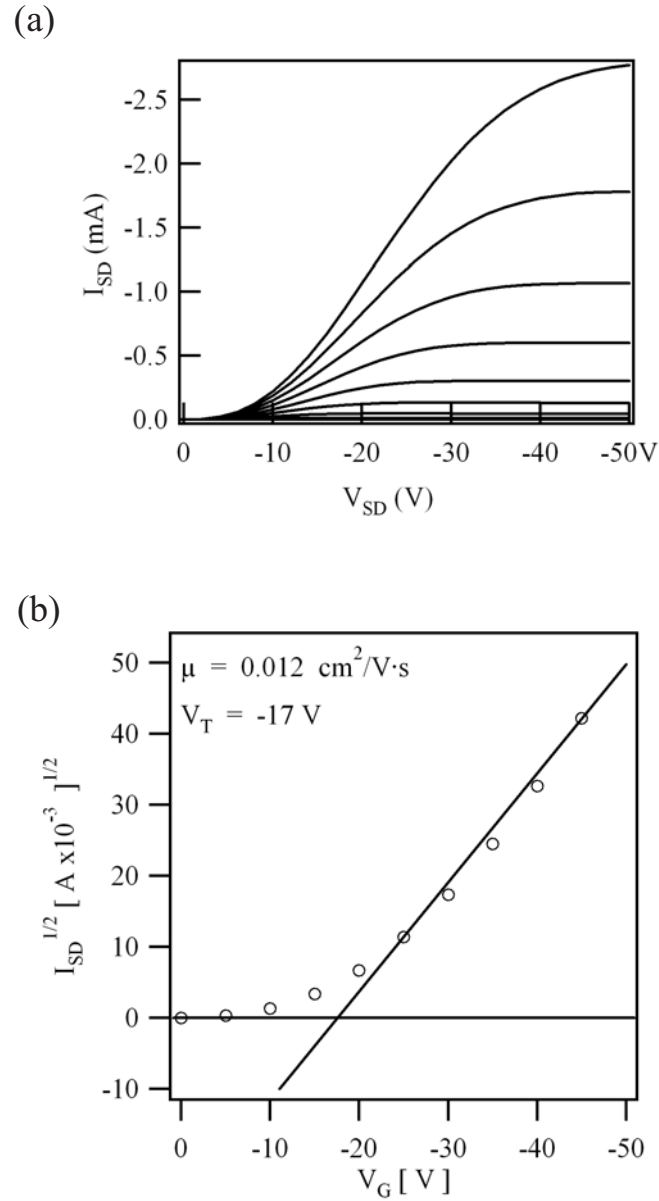


Figure 2.11: (a) Current-voltage characteristics for a pentacene (50 nm thick) thin-film transistor with $W = 20.1$ cm, $L = 6.5$ μm and an oxide thickness of $T = 275$ nm. The gate voltage goes from 0 to -50 V in -5 V steps. (b) The square root of the source-drain current at saturation versus the gate voltage. The mobility and threshold voltage are calculated from the saturation regime.

however there were negative effects on the contact resistance, expressed as the slow rising source-drain current at low source-drain voltages. In contrast, the transistor did reach good saturation. The recessed electrodes were used in the electric force microscopy experiments because the benefits of the flat device out-weighed the costs of having bad contacts, given that contacts and injection are not the focus of these experiments.

It can also be concluded from the current-voltage characteristics that a majority of the charge traps have been filled in the time it takes to sweep one current voltage curve, which is typically under 1 minute. If traps were continuing to fill, there would be a noticeable drop in the current in the saturation regimes. It was noticed that there is a very long time scale decay to the source drain current as traps continue to fill, however, the majority are filled on the timescale of 1 minute or less.

The next section will describe the instrument used to image charge trapping in these pentacene thin-film transistors.

References

- [1] L. Sebastian, G. Weiser, and H. Bassler, "Charge transfer transitions in solid tetracene and pentacene studied by electroabsorption," *Chem. Phys.*, vol. 61, no. 1-2, pp. 125–35, 1981.
- [2] S. Park, S. Kim, J. Kim, C. Whang, and S. Im, "Optical and luminescence characteristics of thermally evaporated pentacene films on si," *Appl. Phys. Lett.*, vol. 80, no. 16, p. 2872, 2002.
- [3] C. D. Dimitrakopoulos, A. R. Brown, and A. Pomp, "Molecular beam deposited thin films of pentacene for organic field effect transistor applications," *J. Appl. Phys.*, vol. 80, no. 4, pp. 2501–2508, 1996.
- [4] R. Endres, C. Fong, L. Yang, G. Witte, and C. Woll, "Structural and electronic properties of pentacene molecule and molecular pentacene solid," *Comp. Mater. Sci.*, vol. 29, no. 3, pp. 362–370, 2004.

- [5] M. L. Tiago, J. E. Northrup, and S. G. Louie, “Ab initio calculation of the electronic and optical properties of solid pentacene,” *Phys. Rev. B*, vol. 67, no. 11, pp. 115212–1–6, 2003.
- [6] J. E. Northrup and M. L. Chabinyo, “Gap states in organic semiconductors: hydrogen- and oxygen-induced states in pentacene,” *Phys. Rev. B*, vol. 68, no. 4, p. 041202, 2003.
- [7] O. D. Jurchescu, J. Baas, and T. T. M. Palstra, “Effect of impurities on the mobility of single crystal pentacene,” *Appl. Phys. Lett.*, vol. 84, no. 16, pp. 3061–3063, 2004.
- [8] G. Horowitz, “Organic field-effect transistors,” *Adv. Mater.*, vol. 10, no. 5, pp. 365–77, 1998.
- [9] H. Sirringhaus, T. Kawase, R. Friend, T. Shimoda, M. Inbasekaran, W. Wu, and E. Woo, “High-resolution inkjet printing of all-polymer transistor circuits,” *Science*, vol. 290, no. 5499, pp. 2123–2126, 2000.
- [10] Y. J. Zhang, J. R. Petta, S. Ambily, Y. L. Shen, D. C. Ralph, and G. G. Malliaras, “30 nm channel length pentacene transistors,” *Adv. Mater.*, vol. 15, no. 19, pp. 1632–1635, 2003.
- [11] J. A. Nichols, D. J. Gundlach, and T. N. Jackson, “Potential imaging of pentacene organic thin-film transistors,” *Appl. Phys. Lett.*, vol. 83, no. 12, pp. 2366–2368, 2003.
- [12] K. P. Puntambekar, P. V. Pesavento, and C. D. Frisbie, “Surface potential profiling and contact resistance measurements on operating pentacene thin-film transistors by kelvin probe force microscopy,” *Appl. Phys. Lett.*, vol. 83, no. 26, pp. 5539–5541, 2003.
- [13] H. Klauk, D. Gundlach, M. Bonse, C.-C. Kuo, and T. Jackson, “A reduced complexity process for organic thin film transistors,” *Appl. Phys. Lett.*, vol. 76, no. 13, pp. 1692–4, 2000.
- [14] Y. L. Shen, A. R. Hosseini, M. H. Wong, and G. G. Malliaras, “How to make ohmic contacts to organic semiconductors,” *ChemPhysChem*, vol. 5, no. 1, pp. 16–25, 2004.
- [15] R. Ruiz, B. Nickel, N. Koch, L. C. Feldman, R. F. Haglund, A. Kahn, and G. Scoles, “Pentacene ultrathin film formation on reduced and oxidized si surfaces,” *Phys. Rev. B*, vol. 67, no. 12, 2003.

ELECTRIC FORCE MICROSCOPY

3.1 Introduction to Electric Force Microscopy

The versatility of the atomic force microscope (AFM) [1] has made it an invaluable tool useful across many fields of study, from physics and chemistry to biology. The electric force microscope (EFM) used in this experiment is a type of AFM sensitive to electrostatic forces between a sharp metalized cantilever tip and the sample. The EFM is capable of measuring local capacitance and potential with a resolution that is set by the tip radius, the tip-sample separation, and the long range nature of the electrostatic interaction. While the resolution may be limited to ~ 100 nm, it is sensitive to potential shifts due to charges at buried interfaces [2,3]. By taking advantage of the force sensitivity of cantilevers, the sensitivity of the EFM is solely matched by scanning single electron transistors, which only operate at cryogenic temperatures. The sensitivity of an EFM operating in vacuum and at room temperature easily reaches single charge sensitivity [4–8].

The microscopic study of pentacene thin film transistors investigating contacts is limited to only two prior studies. The first, done by the Frisbie group at the University of Minnesota [9], compared the contact effects for both top and bottom contact devices using Kelvin probe force microscopy. They showed that bottom contact devices have a large voltage drop at the contact, whereas the top contact devices do not. The conclusion was that bottom contact devices are contact limited and top contact devices are bulk limited.

The Jackson group investigated how band lineup between the contact metal and pentacene affects injection [10]. They observed voltage drops at the contact

using different types of metal as electrodes. They concluded that band lineup is important for efficient charge injection.

These two studies show the value that microscopy studies have in proving or disproving commonly held assumptions, such as the notion that bottom contacts make poor contact to pentacene. This type of information is nearly impossible to deduce from bulk measurements.

The purpose of the experiments presented in this document are not meant to study contacts or transport, but to concentrate on charge trapping [2]. A description of the concepts, design, construction and utilization of an electric force microscope to study charge trapping will be the focus of this chapter.

3.2 Charge Trapping in EFM

This section outlines theory developed in the Marohn Lab to explain current EFM data on organic systems, including transport contact effects, and trapping [3, 11, 12].

The central assumptions surrounding the trapping theories is that the traps are either isolated at the grain boundaries or that they are homogeneously distributed throughout the pentacene. The physical and chemical origins of these traps are not known.

The simplest electric force microscope measurement involves bringing a metal-coated cantilever near a surface and measuring the mechanical resonance frequency of the cantilever as a function of the voltage applied between the cantilever and the sample surface. This measurement was applied to films of organic electronic materials present in co-planar two-terminal devices and field effect transistors. In this section the free energy, force, and force gradient experienced by the cantilever

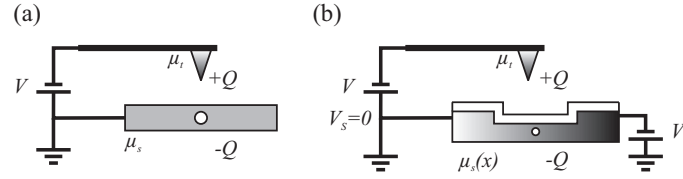


Figure 3.1: (a) Cantilever near a metal sample. (b) Cantilever positioned over a two-terminal device.

when studying such organic electronic devices are derived.

3.2.1 Metal Plates

Analysis of the situation is sketched in Fig. 3.1(a). A metal-coated cantilever tip having chemical potential μ_t is brought near a metal *sample* with chemical potential μ_s . The sample is grounded and a voltage V is applied to the tip. As a result of the tip-sample chemical potential difference and the applied voltage, a charge Q is transferred from the sample to the tip. The energy to charge the system at constant temperature, the Helmholtz free energy, is given by

$$A(Q, T) = \frac{Q^2}{2C} + \frac{Q}{e} (\mu_s - \mu_t). \quad (3.1)$$

Here C is the tip-sample capacitance. The first term is the energy stored in the electric field generated between the tip and the substrate, and the second term is the change in free energy associated with transferring electrons between materials with different chemical potentials.

The voltage is conjugate to the charge, and is given by the derivative

$$V = \left(\frac{\partial A}{\partial Q} \right)_{T,z} = \frac{Q}{C} + \frac{\Delta\mu}{e}, \quad (3.2)$$

where $\Delta\mu = \mu_s - \mu_t$. When the cantilever is set to vibrate, charge will attempt to move between the plates to maintain constant voltage. This is possible if the time

constant of the circuit is sufficiently small compared to the period of oscillation. Assuming this to be the case, the force experienced by the cantilever is obtained by differentiating the grand canonical free energy, which is obtained from A by a Legendre transformation:

$$\Omega(V, T) = A - QV. \quad (3.3)$$

The term $-QV$ accounts for the energy required to move the charge through the battery. In writing Ω , Q must be eliminated as a dependent variable. This is done in the usual way, by using Eq. 3.2 to write Q as a function of V and using the resulting expression to recast A in terms of V . The result is

$$\Omega(V, T) = -\frac{1}{2}C\left(V - \frac{\Delta\mu}{e}\right)^2. \quad (3.4)$$

If the cantilever vibrates slowly enough that the process of moving charge between the metal cantilever tip and the metal substrate may be considered isothermal, then the electrical force on the cantilever is given by the derivative of the grand canonical free energy with respect to the vertical displacement z of the tip,

$$F = -\left(\frac{\partial\Omega}{\partial z}\right)_{T,V} = \frac{1}{2}\frac{\partial C}{\partial z}\left(V - \frac{\Delta\mu}{e}\right)^2. \quad (3.5)$$

For small deflections, the cantilever may be modeled as a one dimensional harmonic oscillator having a spring constant k_0 . Balancing the electrical force F with the Hooke's law restoring force k_0z . The equilibrium deflection,

$$z = \frac{1}{2k_0}\frac{\partial C}{\partial z}\left(V - \frac{\Delta\mu}{e}\right)^2, \quad (3.6)$$

which is a quadratic function of voltage. In addition to displacing the cantilever, the applied voltage will also change the cantilever's spring constant and thus its resonance frequency. To see this, the capacitive derivative, $\partial C/\partial z = C' + C''z + \underline{Q}(z^2)$,

is expanded in a series about $z = 0$. To first order, the electric force is linear in the cantilever displacement,

$$F \simeq \frac{1}{2}C'(V - \frac{\Delta\mu}{e})^2 + \frac{1}{2}C''(V - \frac{\Delta\mu}{e})^2 z. \quad (3.7)$$

It follows that the net restoring force, $F - k_0 z$, is linear in z , and may be described by an effective cantilever spring constant,

$$k = k_0 - \frac{1}{2}C''(V - \frac{\Delta\mu}{e})^2. \quad (3.8)$$

The mechanical resonance frequency f of the cantilever is determined from the spring constant and the effective mass m of the cantilever using

$$f = \frac{1}{2\pi} \sqrt{\frac{k}{m}}. \quad (3.9)$$

In all experiments discussed here, the voltage-induced change in the cantilever spring constant is small compared to k_0 . In this limit, the cantilever resonance frequency is given by

$$f(V) \simeq f_0 - \frac{f_0}{4k_0} C''(V - \frac{\Delta\mu}{e})^2. \quad (3.10)$$

The cantilever resonance frequency decreases quadratically with voltage, having a maximum at a voltage $V_{\max} = \Delta\mu/e$ determined by the difference in the chemical potentials between the sample and the tip. Since f_0 and k_0 are known, C'' can be determined from the curvature of the frequency-voltage parabola.

3.2.2 Organic Device with Two Co-planar Electrodes

The two-terminal device shown in Fig. 3.1 (b) was used to study metal-to-organic charge injection. Charge is injected from a grounded metal source electrode, flows through an organic film, and is extracted at a metal drain electrode

held at a voltage V_d . The process is designed to determine what the electric force microscope measures when it is placed over the film.

Before considering this question, a few remarks on the distinction between the electrostatic potential, chemical potential, and voltage are helpful. The electrochemical potential or voltage in the organic film is

$$V_s(x) = \phi(x) - \frac{\mu(x)}{e}, \quad (3.11)$$

where ϕ is the electrostatic potential and μ is the *local* chemical potential, given by

$$\mu(x) = \mu_0 + kT \ln \left\{ \frac{\gamma(x)n(x)}{n_0} \right\}. \quad (3.12)$$

Here n is the charge concentration, γ is the activity coefficient, and μ_0 and n_0 are the intrinsic chemical potential and concentration of free charges, respectively, in the bulk material. For simplicity, only one type of charge carrier is considered. Assuming a Maxwell-Boltzmann (infinite dilution) limit implies $\gamma = 1$. The current density at any point in the film is proportional to the concentration of free charges and the gradient in the electrochemical potential. In one dimension,

$$J = \frac{eD}{kT} n(x) \frac{dV_s}{dx}, \quad (3.13)$$

where D is the diffusion constant. Substituting Eqs. 3.11 and 3.12 into Eq. 3.13 gives, after some simplification,

$$J = e\mu n \frac{d\phi}{dx} + eD \frac{dn}{dx}. \quad (3.14)$$

The Einstein relation, $\mu = eD/kT$, is used to relate the diffusion constant to the mobility. The first term in Eq. 3.14 represents current due to drift of electrons in an applied field $E = -d\phi/dx$, and the second term is the current arising from diffusion of electrons from high concentration to low concentration. The steps leading to

Equation 3.14 make this clear, but both of these contributions to the current are already captured in Eq. 3.13. The important point is that the current measured is proportional to the gradient of the electrochemical potential (or voltage), not the electrostatic potential.

The Helmholtz free energy associated with charges below the tip is given by

$$A = \frac{Q^2}{2C} + \frac{Q}{e} (\mu_s(x) - \mu_t), \quad (3.15)$$

where $\mu_s(x)$ is written to emphasize that the local chemical potential varies in the film. The mechanical part of A has been left out for simplicity. With the sample under bias, it can be asserted that

$$\frac{\partial A}{\partial Q} = V - V_s(x). \quad (3.16)$$

The term V is the voltage drop through the external battery, and the term $-V_s(x)$ accounts for the IR drop between the source electrode and a point x in the film. The inclusion of both voltages is required to correctly account for the total voltage drop that the charge Q experiences in passing from the tip to a point below the tip in the sample. With this in mind, we construct the grand canonical free energy,

$$\Omega = A - Q(V - V_s(x)), \quad (3.17)$$

and find, after some simplification,

$$\Omega = -\frac{C}{2} \left(V + \frac{\mu_t}{e} - V_s(x) + \frac{\mu_s(x)}{e} \right)^2. \quad (3.18)$$

Considering Eq. 3.11, this may be written simply as

$$\Omega = -\frac{C}{2} \left(V + \frac{\mu_t}{e} - \phi_s(x) \right)^2, \quad (3.19)$$

from which it follows that

$$f \approx f_0 - \frac{f_0}{4k_0} C'' \left(V + \frac{\mu_t}{e} - \phi_s(x) \right)^2. \quad (3.20)$$

Thus, the voltage at which the cantilever frequency is maximum is an indicator of the value of the local electric potential $\phi_s(x)$. This is true in general, whether or not the sample to be measured is under bias.

When the drift current is larger than the diffusion current, the local charge density can be obtained directly from ϕ_s . Neglecting dn/dx in equation Eq. 3.14 gives

$$n(x) \simeq \frac{J}{e\beta D} \frac{1}{\phi'_s}. \quad (3.21)$$

Regions where this approximation is obviously problematic are near materials interfaces, where ϕ'_s can be very large due to the interface dipole, and, moreover, can be either positive or negative. In such a case, the drift-diffusion equation, Eq. 3.14, is reconsidered and rewritten as a first order differential equation for $n(x)$

$$\frac{dn}{dx} + e\beta\phi'_s n = \frac{J}{eD}. \quad (3.22)$$

If both sides of Eq. 3.22 are multiplied by $\exp(q\beta\phi)$ and integrate, we find the solution,

$$n(x) = e^{-\Delta\phi(x)e/kT} \left\{ n(0) + \frac{J}{eD} \int_0^x e^{\Delta\phi(x')e/kT} dx' \right\}, \quad (3.23)$$

in terms of the relative potential $\Delta\phi(x) \equiv \phi(x) - \phi(0)$. For an ideal current flowing in one dimension with constant cross sectional area, the charge density can be determined from the measured potential $\phi_s(x)$ and current density J using Eq. 3.23.

3.2.3 Organic Field-Effect Transistor with Trapped Charge

The force which the cantilever experiences was calculated in the experiment sketched in Fig. 3.2(a). A thin layer of pentacene sits on top of a dielectric layer above a gate. An amount of charge Q_T is transferred to the pentacene, leaving a

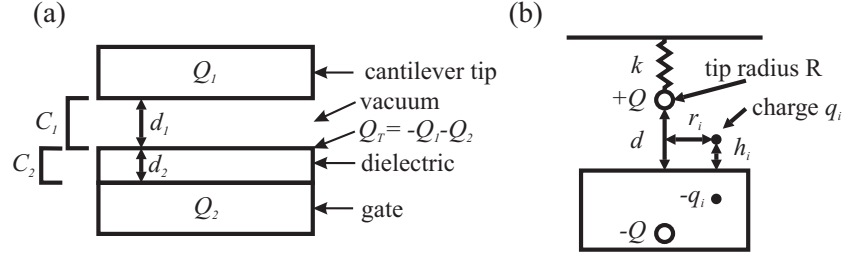


Figure 3.2: Cantilever sample interaction with trapped charge. (a) Parallel-plate model. Charge Q_T is trapped at the dielectric-vacuum interface. (b) Point probe model. In this model, the cantilever interacts with its image charge in the gate, a trapped charge q_i , and the trapped charge's image charge $-q_i$.

charge Q_1 on the tip, and a charge Q_2 on the gate, subject to the constraint of charge conservation,

$$Q_1 + Q_2 + Q_T = 0. \quad (3.24)$$

For a parallel-plate geometry, the Helmholtz free energy associated with a uniform layer of trapped charge is

$$A = \frac{Q_1^2}{2C_1} + \frac{Q_2^2}{2C_2} - \frac{Q_1}{e} \Delta\mu_1 - \frac{Q_2}{e} \Delta\mu_2 \quad (3.25)$$

where

$$\Delta\mu_1 = \mu_{\text{tip}} - \mu_{\text{pentacene}} \quad (3.26)$$

$$\Delta\mu_2 = \mu_{\text{gate}} - \mu_{\text{pentacene}} \quad (3.27)$$

Here C_1 is the capacitance between the tip and the pentacene, and C_2 is the capacitance of the dielectric between the pentacene and the gate. The thickness of the pentacene has been neglected. Considering that the charges Q_1 and Q_2 are not independent, determining the change of A with respect to the change of one

or the other is of interest. The difference in charge,

$$q = \frac{Q_1 - Q_2}{2}, \quad (3.28)$$

is also a convenient variable because it is directly related to the difference in voltage between the tip and the gate,

$$V_{\text{tip}} - V_{\text{gate}} = \frac{\partial A}{\partial Q_1} - \frac{\partial A}{\partial Q_2} = \frac{\partial A}{\partial q} = V, \quad (3.29)$$

which is held constant. In terms of q , the Helmholtz free energy takes the form

$$A = \frac{q^2}{2C} + q \left(\Phi_{\Omega} + \frac{\Delta\mu}{e} \right) + \frac{Q_T^2}{8C} + \frac{Q_T}{2e} (\Delta\mu_1 + \Delta\mu_2) \quad (3.30)$$

where the quadratic term depends on the equivalent series capacitance,

$$C = \frac{C_1 C_2}{C_1 + C_2}, \quad (3.31)$$

and the term linear in q depends on the difference in chemical potential between the tip and the gate,

$$\Delta\mu = \mu_{\text{tip}} - \mu_{\text{gate}}, \quad (3.32)$$

and an additional potential due to the trapped charge,

$$\Phi_{\Omega} = \frac{Q_T}{2} \left(\frac{1}{C_2} - \frac{1}{C_1} \right). \quad (3.33)$$

Differentiating Eq. 3.30 with respect to q gives the relation,

$$q = C \left(V - \Phi_{\Omega} - \frac{\Delta\mu}{e} \right). \quad (3.34)$$

Subtracting qV from Eq. 3.30 gives the grand canonical free energy

$$\Omega = -\frac{1}{2}C \left(V - \frac{\Delta\mu}{e} - \Phi_{\Omega} \right)^2 + \frac{Q_T^2}{8C} + \frac{Q_T}{2e} (\Delta\mu_1 + \Delta\mu_2) \quad (3.35)$$

which has a maximum at the voltage

$$V_{\Omega}^{\text{max}} = \frac{\Delta\mu}{e} + \Phi_{\Omega}. \quad (3.36)$$

The force on the cantilever is given by the derivative of Ω with respect to z ;

$$\begin{aligned} F &= -\frac{\partial\Omega}{\partial z} = \frac{1}{2}C' \left(V - \frac{\Delta\mu}{e} - \Phi_\Omega \right)^2 - C\Phi'_\Omega \left(V - \Phi_\Omega - \frac{\Delta\mu}{e} \right) - \frac{Q_T^2}{8C^2}C' \\ &= \frac{1}{2}C' \left(V - \Phi_F - \frac{\Delta\mu}{e} \right)^2 - \frac{1}{2} \frac{(C\Phi'_\Omega)^2}{C'} - \frac{Q_T^2}{8C^2}C'. \end{aligned} \quad (3.37)$$

Completing the square in Eq. 3.37, it is observed that a minimum force occurs at a voltage offset

$$V_F^{\min} = \frac{\Delta\mu}{e} + \Phi_F. \quad (3.38)$$

It should be emphasized that the voltage offset for the force is not the same as Φ_Ω , but is related to Φ_Ω through a derivative,

$$\Phi_F = \frac{1}{C'} \frac{d}{dz} (C\Phi_\Omega), \quad (3.39)$$

When $V = V_F^{\min}$, there remains an additional force on the cantilever,

$$F(V_F^{\min}) = -\frac{1}{2} \frac{(C\Phi'_\Omega)^2}{C'} - \frac{Q_T^2}{8C^2}C', \quad (3.40)$$

which is given by the last two terms in Eq. 3.37. A nonvanishing $F(V_F^{\min})$ implies a shift in the equilibrium position and effective spring constant of the cantilever which depends on Q_T , but not on V . In what follows, $F(V_F^{\min})$ was ignored; the focus was only on the voltage-dependent part of the effective cantilever spring constant since it is this which determines the curvature and voltage offset of the cantilever frequency-versus-voltage parabola.

The change in the spring constant is given by the derivative of (3.37),

$$\Delta k = k - k_0 = -\frac{\partial}{\partial z} \left[\frac{1}{2}C' \left(V - \Phi_F - \frac{\Delta\mu}{e} \right)^2 \right] \quad (3.41)$$

Carrying out the differentiation in Eq. 3.41, and completing the square, it is seen

that the resulting expression for Δk is isomorphic to Eq. 3.37,

$$\begin{aligned}\Delta k &= -\frac{1}{2}C'' \left(V - \Phi_F - \frac{\Delta\mu}{e} \right)^2 + C'\Phi'_F \left(V - \Phi_F - \frac{\Delta\mu}{e} \right) \\ &= -\frac{1}{2}C'' \left(V - \Phi_k - \frac{\Delta\mu}{e} \right)^2 + \frac{1}{2} \frac{(C'\Phi'_F)^2}{C''}.\end{aligned}\quad (3.42)$$

The maximum spring constant occurs at a voltage,

$$V_{\max}^{(k)} = \frac{\Delta\mu}{e} + \Phi_k, \quad (3.43)$$

however, such that the dependence on trapped charge is neither through Φ_Ω , nor Φ_F , but through the offset

$$\Phi_k = \frac{1}{C''} \frac{d}{dz} (C'\Phi_F) = \frac{1}{C''} \frac{d^2}{dz^2} (C\Phi_\Omega) \quad (3.44)$$

3.2.4 Nonuniform Distribution of Trapped Charge

In the preceding discussion it was assumed that the trapped charge is uniformly distributed, so that the tip-gate could be represented as a parallel plate capacitor. It is instructive to examine the voltage offsets Φ_Ω , Φ_F , and Φ_k for this geometry in more detail, by writing capacitances explicitly:

$$C_1 = \frac{\epsilon_0\alpha}{d_1 + z}, \quad (3.45)$$

$$C_2 = \frac{\epsilon_0\alpha}{d_2}, \quad (3.46)$$

where α is the plate area, and d_1+z and d_2 are the gaps between tip and sample, and sample and gate, respectively. The gap between the tip and the sample depends on the vibrational amplitude z , whereas the gap d_2 between the sample and the gate remains constant. See Fig. 3.2(a), where d_2 was scaled by the relative permittivity of the substrate. Substituting Eqs. 3.45 and 3.46 in Eqs. 3.33, 3.39, and 3.44, the

voltage offsets were found,

$$\Phi_{\Omega} = \frac{Q_T}{2\epsilon_0\alpha} (d_2 - d_1 - z), \quad (3.47)$$

$$\Phi_k = \Phi_F = -Q_T \frac{d_2}{\epsilon_0\alpha} = -\frac{Q_T}{C_2}. \quad (3.48)$$

Thus the minimum force and maximum spring constant occur at the same voltage, and each is a measure of the total amount of trapped charge. It is useful to note that the free energy is not unique. At constant voltage, the same force may be obtained from the derivative of an alternate free energy $\tilde{\Omega} = \Omega - \lambda V$, where λ is a constant. Choosing $\lambda = Q_T/2$ leads directly to a z -independent voltage offset

$$\Phi_{\tilde{\Omega}} = -\frac{Q_T}{C_2}, \quad (3.49)$$

from which Eq. 3.48 follows immediately. Eq. ref23 and Eq. ref24 are used to analyze charge trap experiments presented in later chapters.

When the distribution of trapped charge is non-uniform, an explicit expression for the Helmholtz free energy can be determined using the method of images. If the polarizability of the dielectric layer is neglected, the calculation is straightforward. In such a case it can be shown that the grand canonical free energy has the same form as Eq. 3.35, but in this case the offset voltage is given by

$$\Phi_{\Omega} = -\frac{Q_T}{2\epsilon_0\alpha} z + \Phi_{\Omega_0} \quad (3.50)$$

where the constant Φ_{Ω_0} is a weighted sum of the trapped charges q_i over the difference in their vertical separations d_{1_i} from the tip and d_{2_i} from the gate;

$$\Phi_{\Omega_0} = \sum_i \frac{q_i}{2\epsilon_0\alpha} (d_{2_i} - d_{1_i}). \quad (3.51)$$

Substituting Eq. 3.50 into Eqs. 3.39 and 3.44, the finding was that the voltage offsets,

$$\Phi_F = \Phi_k = \sum_i \frac{q_i}{2\epsilon_0\alpha} [(d_{2_i} + d_2) + (d_1 - d_{1_i})]. \quad (3.52)$$

for the force and spring constant are the same. It can be shown that the equality of Φ_F and Φ_k follows from the fact that both $1/C$ and Φ_Ω (Eq. 3.50) are linear in z for the case of a parallel-plate geometry.

3.2.5 Deviations from the Parallel Plate Geometry

To understand how the voltage offsets Φ_F and Φ_k change as a function of tip location in an electric force microscope measurement, it is important to consider a case in which the tip is much smaller than the feature size. The problem can be solved exactly in the point-probe limit, in which the tip is taken to be a small metal sphere of radius R which is suspended above the gate electrode at a height $d \gg R$. See Fig. 3.2(b). In this limit the grand canonical free energy takes the form,

$$\Omega = -\frac{1}{2}C \left(V - \frac{\Delta\mu}{e} - \Phi_\Omega \right)^2, \quad (3.53)$$

where the capacitance is that of a conducting sphere above a conducting plane,

$$C \simeq 4\pi\epsilon_0 R \left(1 + \frac{R}{2(d+z)} + \mathcal{O}\left(\frac{R}{d+z}\right)^2 \right), \quad (3.54)$$

and may be expanded as a power series to first order in R/d . The free energy offset,

$$\Phi_\Omega = \sum_i \frac{q_i}{4\pi\epsilon_0} \left(\frac{1}{\sqrt{(h_i + d + z)^2 + r_i^2}} - \frac{1}{\sqrt{(h_i - d - z)^2 + r_i^2}} \right), \quad (3.55)$$

is the Coulomb potential at the tip due to the trapped charges, located by their cylindrical coordinates (r_i, h_i) with respect to an axis through the tip, and their images at $(r_i, -h_i)$ in the gate electrode below. The polarization of the dielectric was again neglected. Substituting Eq. 3.54 into Eqs. 3.39 and 3.44, we find that the force offset

$$\Phi_F = \Phi_\Omega - d\Phi'_\Omega - \frac{2d^2}{R}\Phi''_\Omega \quad (3.56)$$

and the spring constant offset

$$\Phi_k = \Phi_\Omega - d\Phi'_\Omega + d^2\Phi''_\Omega + \frac{d^3}{R}\Phi'''_\Omega \quad (3.57)$$

are not necessarily the same. If the distribution of charge is uniform, then $\Phi'_\Omega = \Phi''_\Omega = 0$, and indeed, $\Phi_F = \Phi_k$, as is the case for a parallel plate capacitor. When the distribution is nonuniform, however, for small enough R , the derivative terms Φ'_Ω and Φ''_Ω in (3.56) and (3.57) will be enhanced by the factor d/R ($\gg 1$). In such a case, the voltage offsets for the force and spring constant,

$$\Phi_F \simeq -2\frac{d^2}{R}\Phi'_\Omega \quad (3.58)$$

$$\Phi_k \simeq \frac{d^3}{R}\Phi''_\Omega \quad (3.59)$$

will be largely determined by Φ'_Ω and Φ''_Ω , respectively.

3.3 Cantilever Response to Thermal Fluctuations

The noise in the electric force microscope is set by the response of the cantilever to random thermal fluctuations. The response of the cantilever follows the equation of motion for a damped driven harmonic oscillator. This section will outline the response of the cantilever to both coherent and incoherent driving forces. Coherent forces arise from external periodic driving such as a sinusoidal force from a piezo element placed beneath the base of the cantilever. Incoherent forces arise from sources such as room vibrations or thermal fluctuations.

The response of the cantilever is described by the equation of motion for a damped driven harmonic oscillator,

$$\ddot{x} + \frac{\omega_0}{Q}\dot{x} + \omega_0^2x = \frac{\omega_0^2F}{k} \quad (3.60)$$

where x is the position of the cantilever tip, ω_0 is the natural resonance frequency, Q is the quality factor, F is any applied force (coherent or incoherent), and k is the spring constant. A natural question to ask is what is the frequency dependence of the cantilever displacement for a given driving force. The two cases for the functional form of the driving force mentioned previously, coherent and incoherent, will be treated below.

Coherent Driving Force First, the case where the functional form of $F(t)$ is sinusoidal,

$$F(t) = F_0 \cos(2\pi ft). \quad (3.61)$$

The steady state response must also be periodic and have the form

$$x(t) = x_c \cos(2\pi ft) + x_s \sin(2\pi ft) \quad (3.62)$$

where x_c is the in-phase response and x_s is the out-of-phase response. The next step is to plug in the appropriate derivatives of Eq. 3.62 and Eq. 3.61 into Eq. 3.60 to get an expression for x_c and x_s .

First, taking the time derivative of the cantilever response gives:

$$\dot{x}(t) = -2\pi f x_c \sin(2\pi ft) + 2\pi f x_s \cos(2\pi ft). \quad (3.63)$$

The second derivative is:

$$\ddot{x}(t) = -4\pi^2 f^2 x_c \cos(2\pi ft) - 4\pi^2 f^2 x_s \sin(2\pi ft). \quad (3.64)$$

Note that,

$$\ddot{x}(t) = -4\pi^2 f^2 x(t). \quad (3.65)$$

The equation of motion can then be written as,

$$\left[x_c (f_0^2 - f^2) + \frac{f f_0 x_s}{Q} \right] \cos(2\pi f t) + \left[x_s (f_0^2 - f^2) - \frac{f f_0 x_c}{Q} \right] \sin(2\pi f t) = \quad (3.66)$$

$$\frac{f_0^2 F_0}{k} \cos(2\pi f t). \quad (3.67)$$

Matching the sine and cosine terms on both sides of the equation results in two simultaneous equations for x_c and x_s ,

$$x_c (f_0^2 - f^2) + \frac{f f_0 x_s}{Q} = \frac{f_0^2 F_0}{k} \quad (3.68)$$

and

$$x_s (f_0^2 - f^2) - \frac{f f_0 x_c}{Q} = 0. \quad (3.69)$$

Solving for x_c and x_s gives,

$$x_s = \frac{F_0}{k} \cdot \frac{f f_0^3 / Q}{(f_0^2 - f^2)^2 + f_0^2 f^2 / Q^2} \quad (3.70)$$

and

$$x_c = \frac{F_0}{k} \cdot \frac{f_0^2 (f_0^2 - f^2)}{(f_0^2 - f^2)^2 + f_0^2 f^2 / Q^2}. \quad (3.71)$$

This is the cantilever response to a coherent sinusoidal driving force. There are two interesting limits. The first is when the cantilever is driven with a DC force. Then,

$$x_c(0) = \frac{F_0}{k} \quad (3.72)$$

$$x_s(0) = 0. \quad (3.73)$$

This is Hooke's law. When the cantilever is driven by an AC force at its natural resonance frequency the drive is out-of-phase and Q times larger,

$$x_c(f_0) = 0 \quad (3.74)$$

$$x_s(f_0) = \frac{Q F_0}{k}. \quad (3.75)$$

As a practical matter, if the response is measured with a lock-in amplifier, then x_c and x_s are recorded in the x and y channels, respectively.

Incoherent Driving Force The problem of an incoherent driving force is examined. This is the case where the driving force is random in time and its functional form is not known. This problem is presented to explain the response of the cantilever to the random thermal vibrations associated with being at a temperature T . In order to proceed, we make only one assumption about the driving force, i.e. that the driving force has a flat power spectral density up to some high frequency limit and is 0 above that frequency, i.e. white noise. The response was calculated using the Fourier transform instead of the time domain signal. The Fourier transform of $x(t)$ and $F(t)$ are,

$$x(t) = \int_{-\infty}^{\infty} \hat{x}(f) e^{-i2\pi ft} df \quad \hat{x}(f) \sim [\text{m/Hz}] \quad (3.76)$$

$$F(t) = \int_{-\infty}^{\infty} \hat{F}(f) e^{-i2\pi ft} df \quad \hat{F}(f) \sim [\text{N/Hz}]. \quad (3.77)$$

These two equations can then be plugged into the equation of motion, Eq. 3.60.

$$\int_{-\infty}^{\infty} \left(-f^2 - \frac{i f f_0}{Q} + f_0^2 \right) \hat{x}(f) e^{-i2\pi ft} df = \int_{-\infty}^{\infty} \frac{f_0^2}{k} \hat{F}(f) e^{-i2\pi ft} df. \quad (3.78)$$

For this equality to be true, the following is necessary,

$$\hat{x}(f) = \frac{\hat{F}(f)}{k} \cdot \frac{f_0^2}{f_0^2 - f^2 - i f f_0 / Q}. \quad (3.79)$$

It is very important to be careful regarding Eq. 3.79. The Fourier transforms, $\hat{x}(f)$ and $\hat{F}(f)$ have units of [m/Hz] and [N/Hz], respectively. The physically relevant quantity for incoherent signals is the power spectral density defined by,

$$P_x(f) = \lim_{T \rightarrow \infty} \frac{1}{2T} (|\hat{x}(f)|^2 + |\hat{x}(-f)|^2) \quad (3.80)$$

and

$$P_F(f) = \lim_{T \rightarrow \infty} \frac{1}{2T} (|\hat{F}(f)|^2 + |\hat{F}(-f)|^2). \quad (3.81)$$

The resulting one-sided power spectral density is given by,

$$P_x(f) = \frac{P_F(f)}{k^2} \cdot \frac{f_0^4}{(f_0^2 - f^2)^2 + f^2 f_0^2 / Q^2} \sim [\text{m}^2/\text{Hz}]. \quad (3.82)$$

Eq. 3.82 is valid for any form of the noise spectral density, $P_F(f)$. But, in the case of a cantilever driven thermally, $P_F(f)$ can be considered flat and simplified to $P_F(0)$. This is true provided there are no mechanical vibrations near the cantilever resonance frequency. The power spectrum is then,

$$P_x(f) = \frac{P_F(0)}{k^2} \cdot \frac{f_0^4}{(f_0^2 - f^2)^2 + f^2 f_0^2 / Q^2} \sim [\text{m}^2/\text{Hz}] \quad (3.83)$$

Also, using Parseval's theorem, the one sided power spectrum can be used to find the rms-squared displacement of the cantilever by calculating the area under the power spectrum,

$$x_{\text{rms}}^2 = \int_0^\infty P_x(f) df. \quad (3.84)$$

Next, it is shown how the thermal response of the cantilever can be used as a simple, non-destructive method of determining the spring constant.

Spring Constant Determination The equipartition theorem states that each mode of the harmonic oscillator contains an average energy of $k_B T/2$ when coupled to a heat bath at temperature, T . Therefore,

$$\frac{1}{2} k \langle x^2 \rangle = \frac{1}{2} k_B T \quad (3.85)$$

where k_B is Boltzmann's constant and $\langle x^2 \rangle$ is the mean-square displacement of the cantilever. The spring constant is then

$$k = \frac{k_B T}{\langle x^2 \rangle}. \quad (3.86)$$

By integrating the measured power spectrum according to Eq. 3.84, the mean-squared displacement, $\langle x^2 \rangle$, can be determined, allowing for easy calculation of the spring constant.

The spring constant can be related to the power spectral density of the force by mathematically integrating Eq. 3.84,

$$\langle x^2 \rangle = P_x(0) f_0^4 \int_0^\infty \frac{df}{(f^2 - f_0^2)^2 + f^2 f_0^2 / Q^2} \quad (3.87)$$

$$= \frac{\pi}{2} P_x(0) Q f_0. \quad (3.88)$$

Minimum Detectable Force The minimum detectable force can be calculated by integrating the power spectral density of the force around a small bandwidth center about a frequency, f ,

$$F_{min}^2 = \int_{f-\Delta f/2}^{f+\Delta f/2} P_F(f) df. \quad (3.89)$$

Because it is assumed that the power spectral density of the force fluctuation is flat, the integral simplifies to,

$$F_{min}^2 = P_F(0) \Delta f \quad (3.90)$$

where Δf is the detection bandwidth. Using Eq. 3.82 and Eq. 3.88, the minimum detectable force is,

$$F_{min} = \sqrt{\frac{2k\Delta f k_B T}{\pi Q f_0}}. \quad (3.91)$$

3.4 The Electric Force Microscope – Components Overview

A block diagram of the major components of the electric force microscope is shown in Fig. 3.3. The components are discussed in greater detail in the sections that follow.

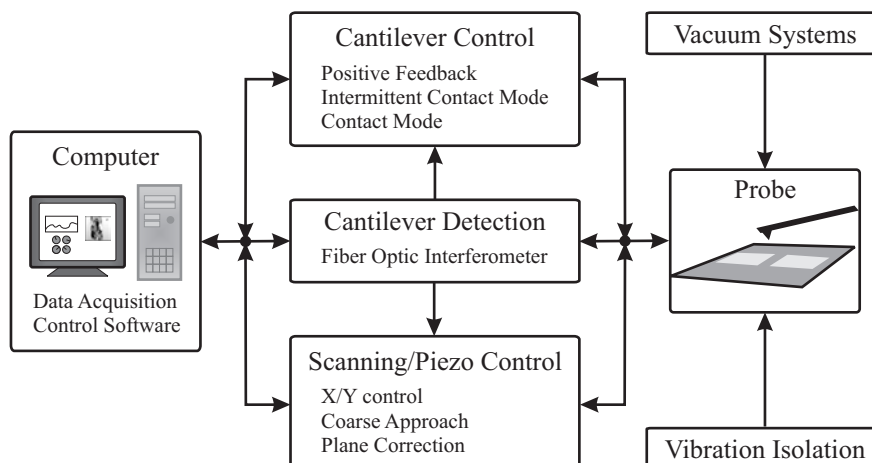


Figure 3.3: Block diagram for the electric including all the support instrumentation.

3.5 EFM - Peripheral Components

3.5.1 Vibration Isolation

As with any scanned probe instrument, adequate isolation from unwanted vibrations is necessary. The design for the vibration isolation was a consequence of many factors. First, the probe was to remain fixed in position and rigidly attached to the vibration isolation to avoid any damage to the sample or cantilever. Second, because the probe is a ~ 5 -foot long dip-stick design, the vibration isolation had to be tall to accommodate a dewar beneath it. Third, the laboratory is on the second floor and no pit for dewar could be made, reiterating the need for the vibration isolation to be tall.

A picture of the vibration isolation can be seen in Fig. 3.4. The vibration isolation consists of a Technical Manufacturing Corporation (TMC) built support structure – four large black 6" x 6" posts with five 2" x 4" horizontal support bars on three sides, one across the top of the front. The vibration isolation plat-



Figure 3.4: Picture of the EFM including the probe, vibration isolation, and vacuum pump.

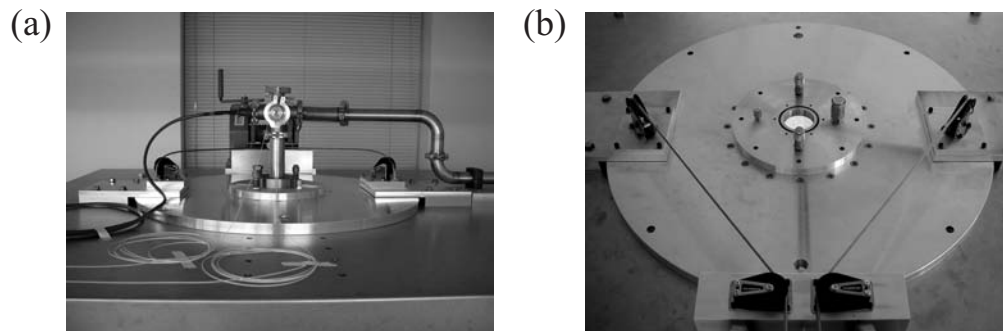


Figure 3.5: (a) Top of the vibration isolation. (b) The large diameter aluminum disks are the probe mounting plates on top of the vibration isolation.

form is an alternating stainless steel and wood laminate which provides excellent vibration isolation from both low and high frequencies. It is four inches thick and weighs approximately 2000 pounds. The tall columns that support the platform are roughly 8 feet tall and each leg has a footprint that is 12 inches square. Four air legs float the platform using compressed air at 60 psi supplied by the building. The compressed air is filtered and dried prior to entry into the air legs. Raising and lowering the plate is achieved simply by adjusting a pressure regulator.

There is a large hole, 28 inches in diameter, in the center of the platform which accommodates a separate mount for the probe and the dewar. Covering the large hole in the vibration isolation is a 30 inch diameter and 1 inch thick aluminum plate (see Fig. 3.5). The plate was made by Precision Cryogenics and includes bolt patterns for bolting the dewar and the probe to the vibration isolation. An intermediate aluminum plate, 12 inches in diameter, bridges the 30-inch plate to the probe itself. This smaller plate contains pressure relief valves and transfer line feedthroughs for the cryogen (see Fig. 3.5(b)). The probe is mounted directly to the smaller 12 inch plate.

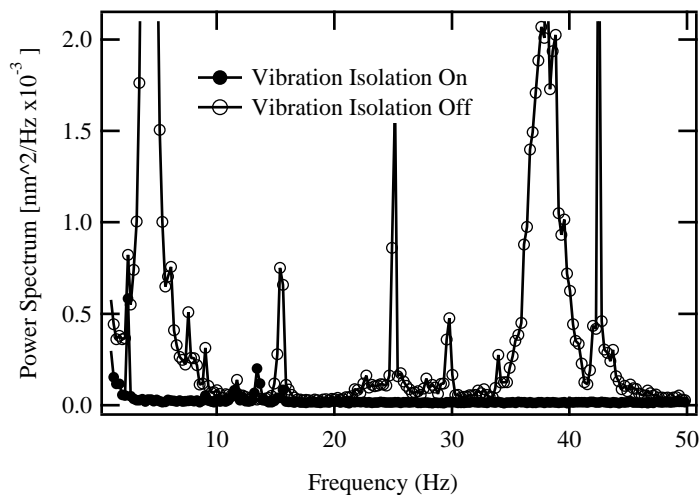


Figure 3.6: Power spectrum as measured by the motion of a cantilever touching a surface with and without the vibration isolation. Data is taken in a 1kHz bandwidth, but most of the motion is below 10Hz. With the vibration isolation on, the total motion is 0.06nm; with the vibration isolation off the total motion is 0.27nm.

As a test of the vibration isolation system, a cantilever was crashed into the sample surface and the vibration spectrum between the tip and the sample was measured. Fig. 3.6 shows the power spectrum of the motion between the cantilever and the sample out to 50Hz with the vibration isolation on and off. The test demonstrated a clear advantage of employing vibration isolation, as the vibrational noise with the air legs inflated was a factor of 5 times smaller than with the air legs deflated.

3.5.2 Electrical Connections and Wiring

This section covers the electrical connections from the electronics rack to the inside of the probe. It does not cover the connections to specific elements of the microscope head, such as piezos.

At the top of the probe head is an electrical connections block. This block uses various socket connectors, purchased from Samtec, Incorporated. The wires travel from this connection block to a heat sinking stage, where they are wrapped around a copper block and held into place using GE varnish. The wires are a phosphor bronze, 36 AWG cryogenic wire with a Formvar® insulation available from Lake Shore Cryogenics Incorporated (Model: Quad-Lead QL-36). It is a ribbon cable which ensures the best thermal sinking when wrapped around the copper block.

The wires are changed to a “Quad-Twist” cryogenic wire immediately after the heat sink and travel to the top of the probe. This wire, also from Lake Shore Cryogenics Incorporated (Model: Quad-Lead QT-36), consists of two sets of twisted pair, 36 AWG wire also with a Formvar® insulation. Both wires were chosen to minimize the heat loss of the probe head.

The vacuum feedthroughs for the wires consist of a military style 19-pin connector that has been soldered into a blank NW-40 vacuum flange. This type of connector is capable of reaching a vacuum of 10^{-6} Torr. There are two of these connectors mounted on the top of the probe to accommodate the 38 wires.

A cable consisting of ten individually shielded twisted pairs of wires carry the signals from the probe to the electronics rack. The shields are all tied together and grounded in only one location, on the rack side of the cable. The individual twisted pairs are then wired to a break-out box where each pair is connected to one floating BNC connector. The shields of the BNC connectors can be grounded individually for noise considerations.

3.5.3 Vacuum System

The system is placed under a vacuum of about 10^{-6} Torr using a Pfeiffer turbomolecular pump. All vacuum connections are made using NW-40 flanges. A 1 m flexible vacuum line connects the pump to an inertial dampening stage to halt vibrations from the pump from being coupled to the probe. This stage consists of a rigid vacuum tube that is embedded into a small concrete block that is resting in sand (see the black box on the right of Fig. 3.4). From this box, another flexible vacuum line goes to the heavy platform on the vibration isolation where it is rigidly attached with clamps. A clamp can be seen in Fig. 3.5(a) – the dark grey object on the far right, middle of the picture. From there, the vacuum line is connected to the probe with a valve. The top of the probe is a six-way NW-40 vacuum connector. This setup effectively eliminates any vibration noise from the vacuum pump from coupling to the probe. The whole system takes roughly one half hour to pump down.

3.5.4 Cryogenic System

The electric force microscope was designed to operate at variable temperatures from 4K to slightly above room temperature. Raising the temperature too high can melt the optical fiber cladding (150°C is too high). The probe is cooled by immersing the brass vacuum can directly into cryogen and cooling with an exchange gas.

A custom designed helium dewar is hoisted up to the vibration isolation using a Jeamar hand winch (background of Fig. 3.5(a)). The cabling and pulley system can be seen in Fig. 3.5(b) and are actually sailboat products. The pulleys are made by Schaefer Marine and have good smooth operation and strength.

The liquid helium dewar, built by Precision Cryogenics, is superinsulated with a 60 liter capacity and weighs about 150 lbs. The 60 liters of helium surprisingly add only 17 lbs. to the weight.

3.5.5 Computer Systems, GPIB and Data Acquisition

The microscope is controlled using a Dell Pentium III based computer system running Microsoft Windows XP Professional. The processor runs at 667 MHz and there are 512 MB of system memory. This is a system that could use upgrading to spare any agony that future students might endure with such a machine. Communication with instruments is performed through a GPIB bus controlled with a National Instruments PCI-GPIB board. The data acquisition is handled using a National Instruments DAQ board, model NI PCI-6259. It has a maximum acquisition rate of 1 MSamples/s on 32 channels and 4 digital output channels with 16-bit precision at the same rate. The input to the board is via a National Instruments break-out box, model BNC-2090, which facilitates easy connection to BNC cables. It runs in referenced single-ended mode, i.e. the center pin of each BNC cable is reference to the shield which is held at ground potential.

All of the control software is written with National Instruments LabView 7.1. A major benefit of LabView is that complicated software is relatively fast and easy to write. Although the execution of the software is slow compared to c-code, the speed is more than adequate for most of the necessary controls of a scanned probe microscope.

3.6 EFM - Core Components

3.6.1 Probe

The probe is housed in a ~ 5 foot long, 1 3/4 inch diameter vacuum can that can be seen in Fig. 3.7. Close-up pictures are also shown in Fig 3.7. The upper part of the probe is made of stainless steel. A brass can at the bottom is removable via a 1° vacuum seal. All of the electrical, optical and vacuum feedthroughs are at the top of the vacuum can, which is located above the vibration isolation platform. All vacuum connections are type NW-40.

Inside the vacuum can are located 3 rods that extend from the top of the vacuum can to just above the 1° seal. At the bottom of these rods is installed a six-inch long bellows above the 1° seal. The bellows has a relatively low resonant frequency of a few hertz with a load of about 0.5 kg. The longitudinal spring constant is roughly 100 N/m. The probe is attached to the bottom of the bellows via a hollow rod that extend through the 1° seal. The bellows provide a last line of defense against vibrations. The probe head can be seen in Fig. 3.8. The various parts of the probe head are discussed individually elsewhere in this document.

3.6.2 Fiber Optic Interferometer

The cantilever motions are detected using a fiber-optic interferometer which is compact and low noise. The electric force microscope uses a fiber-optic interferometer [13–15] to detect the displacement of the cantilever. The wavelength of the laser diode is $\lambda = 1310\text{nm}$, well below the bandgap of most organic semiconductors. The fiber-optic interferometer is compatible with ultrahigh vacuum [16]. In contrast to other detection schemes, such as beam deflection [17] or piezoresistance based

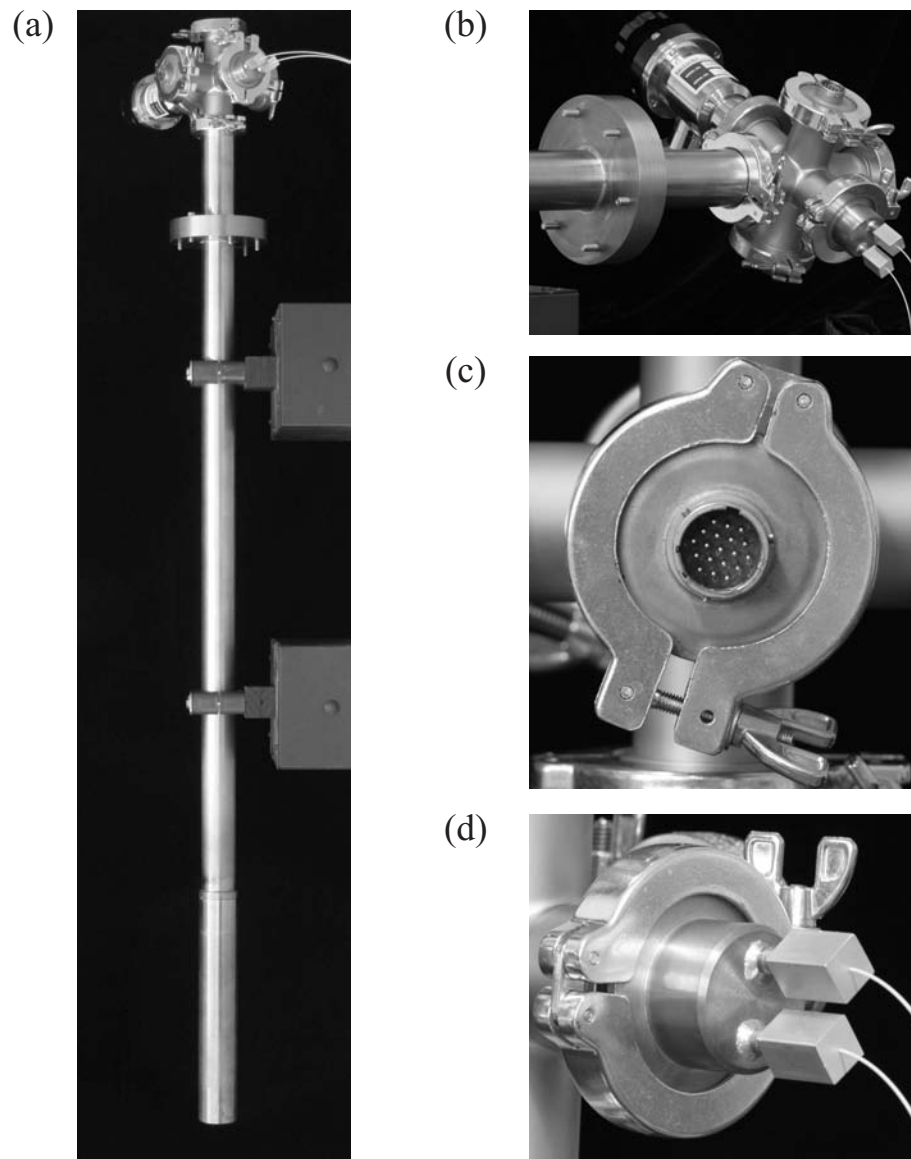


Figure 3.7: Picture of the EFM vacuum can housing the probe. (b) six-way NW flange with electrical and fiber feedthroughs, (c) close-up of the electrical feedthrough showing the 19-pin military connector, and (d) close-up of the fiber optic cable feedthrough.

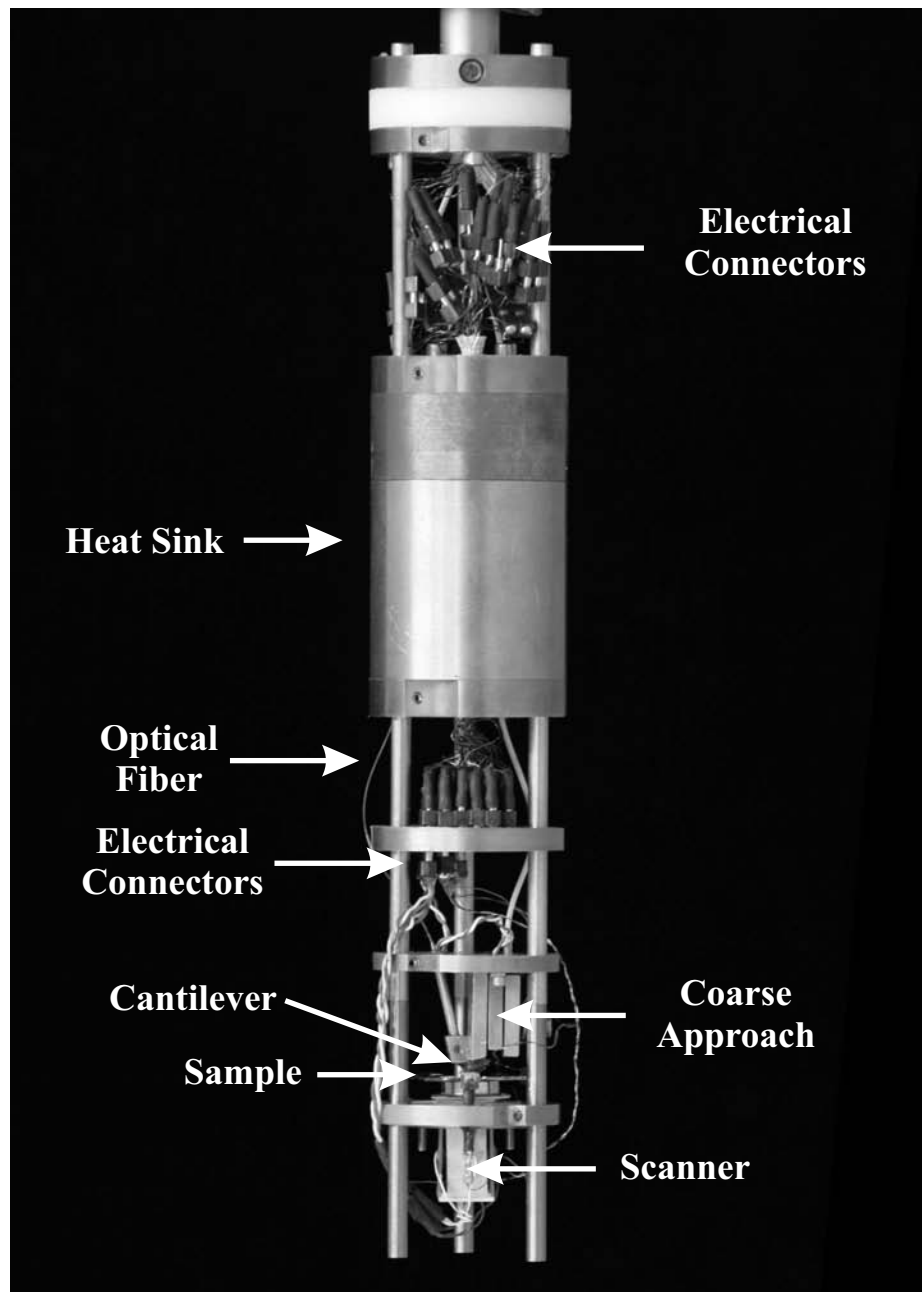


Figure 3.8: Picture of the probe head showing many of the integral components of the microscope.

detection [18,19], the fiber-optic interferometer measures displacements quantitatively. The fiber-optic cable is coupled into the microscope using a variation of the design used by Abraham *et. al.* [16,20,21].

The fiber-optic interferometer underwent many incarnations within the lab originating with components that operated using 780 nm wavelengths. As the communications industry moved towards longer wavelength, components for 780 nm wavelength became impossible to find. The decision was made to upgrade the interferometer to components using 1310 nm wavelengths, as parts were easier to find and less expensive. Fortuitously, this upgrade also moved the energy of the light well below the bandgap in these organic semiconductors, eliminating the possibility of exciting extraneous charge carriers with the interferometer.

A description of the operation, design, and performance of the 1310 nm fiber-optic interferometer follows. The fiber optic interferometer was first demonstrated by measuring the motion of a cricket's tympanic membrane [13]. The version implemented for this experiment is most similar to the design by Rugar *et.al.*, which is an all fiber-optic design [14,22].

The simplest way to understand the principle behind the fiber optic interferometer is just to follow the light that is emitted out the laser diode (see Fig. 3.9). Monochromatic light produced by a commercial Fabry-Perot laser diode (Laser Diode Incorporated, model # SCW 1301G-200FC with an angle polished connector) is sent down a single mode optical fiber (Corning 9/125 - the core is 9 μm in diameter and the cladding is 125 μm in diameter). An optical coupler is used which sends ten percent of the light down a fiber optic cable that is cleaved at ninety degrees and mounted above the cantilever with a working distance of about 50 μm . A block diagram of the optics is shown in Fig. 3.9. At the cleaved inter-

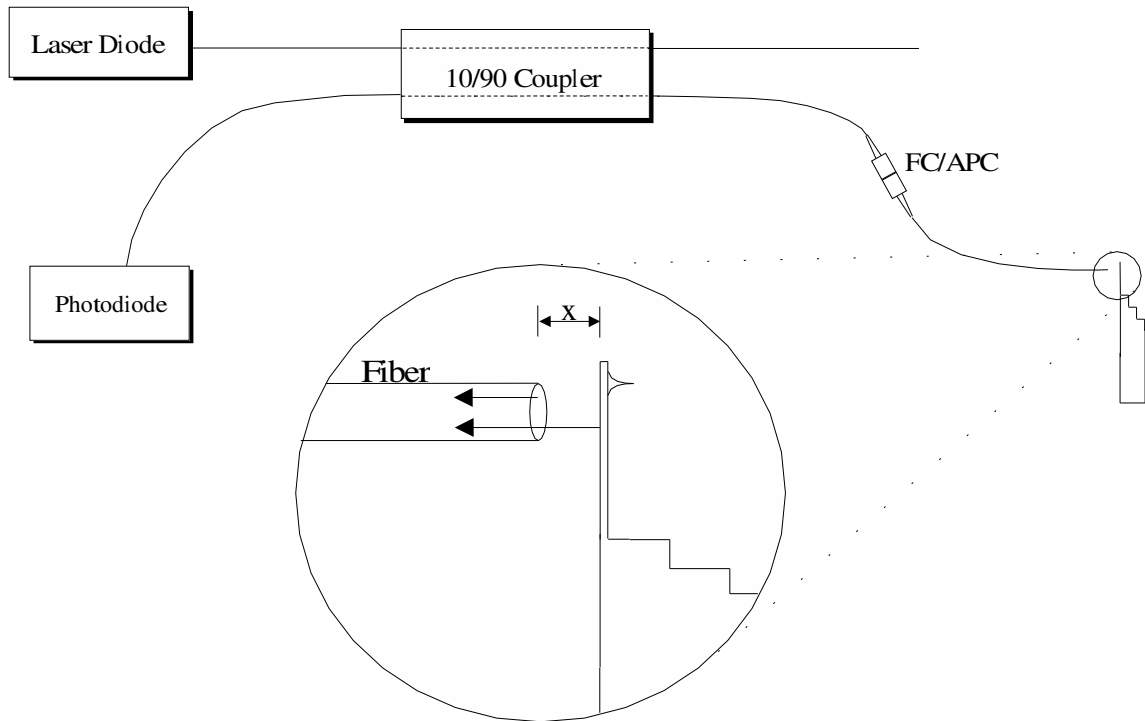


Figure 3.9: A block diagram of the fiber optic interferometer. Light from the laser diode is coupled into a 10/90 optical coupler. This light follows the fiber down to the cantilever and reflects back through the coupler and into the photodiode.

face, a portion of the light is reflected back through the fiber and some is partially transmitted. The transmitted portion reflects off the cantilever surface and returns through the fiber. The interference pattern from these two beams are monitored with a photodiode.

Cantilever Signal Derivation This section will describe the derivation of the basic functional form of the interference pattern from simple geometric and optical considerations. The two interfering beams are the beam bouncing off the cleaved end of the fiber and the beam bouncing off the cantilever and re-entering the fiber. The “path difference” that is commonly associated with interference patterns is generated by the distance between the cleaved end of the fiber and cantilever.

In order to determine the interference pattern, the first step must be to determine the electric field of the light coupled into the fiber from the laser. It is assumed that all beams are composed of plane waves. From introductory electrostatics, the time-averaged power contained in the plane wave traveling down the fiber is given by,

$$P_0 = \frac{1}{2} c \epsilon_r \epsilon_0 E_0^2 A \quad (3.92)$$

where P_0 is the power coupled into the fiber, c is the speed of light, ϵ_r is the dielectric constant of the inner core of the optical fiber, ϵ_0 is the dielectric of free space, E_0 is the electric field amplitude of the wave, and A is the total area of the inner core of the optical fiber. A typical value for P_0 is about 70 μW . The dielectric constant is not given in the specification sheet for the Corning fiber that is used (the approximation that $\epsilon_r = \sqrt{n}$ is assumed where $n(= 1.47)$ is the index of refraction for the core of the fiber. This approximation is called the Maxwell relation and holds true for materials that are not very magnetic. In this case

$\epsilon_r = 1.2$. The area, A , of the fiber core is easily calculated from its diameter; $A = \pi(4.5 \times 10^{-6})^2 = 6.7 \times 10^{-11} \text{m}^2$. Plugging these numbers into eq. 3.92 allows E_0 to be calculated:

$$E_0 = \sqrt{\frac{2P_0}{c\epsilon_r\epsilon_0 A}} \quad (3.93)$$

$$= \sqrt{\frac{2(70 \times 10^{-6} \text{ W})}{(3 \times 10^8 \text{ m/s})(1.2)(8.85 \times 10^{-12} \text{ C}^2/\text{Nm}^2)(6.7 \times 10^{-11} \text{ m}^2)}} \quad (3.94)$$

$$= 2.6 \times 10^4 \text{ V/m}. \quad (3.95)$$

This beam, with an electric field magnitude of $2.6 \times 10^4 \text{ V/m}$, will be incident of the cleaved end of the fiber at which point it will be partially reflected and partially transmitted. Again, introductory electrostatics can be used to calculate the resulting reflected and transmitted electric fields.

$$E_R = \left| \frac{n_1 - n_2}{n_1 + n_2} \right| E_0 \quad (3.96)$$

$$E_T = \left(\frac{2n_1}{n_1 + n_2} \right) E_0 \quad (3.97)$$

where E_R is the amplitude of the reflected wave, E_T is the amplitude of the transmitted wave, n_1 is the refractive index of the fiber core and n_2 is the refractive index of vacuum.

$$E_R = 0.2E_0 = 0.5 \times 10^4 \text{ V/m} \quad (3.98)$$

$$E_T = 1.2E_0 = 3.1 \times 10^4 \text{ V/m}. \quad (3.99)$$

The fact that the electric field of the transmitted wave increased in amplitude should not be of concern, because the medium changed from glass to vacuum such that the total energy stored in the two waves is conserved.

The focus now is on what happens to the wave that just left the fiber. It is no longer confined to the fiber core and therefore leaves the fiber at an angle

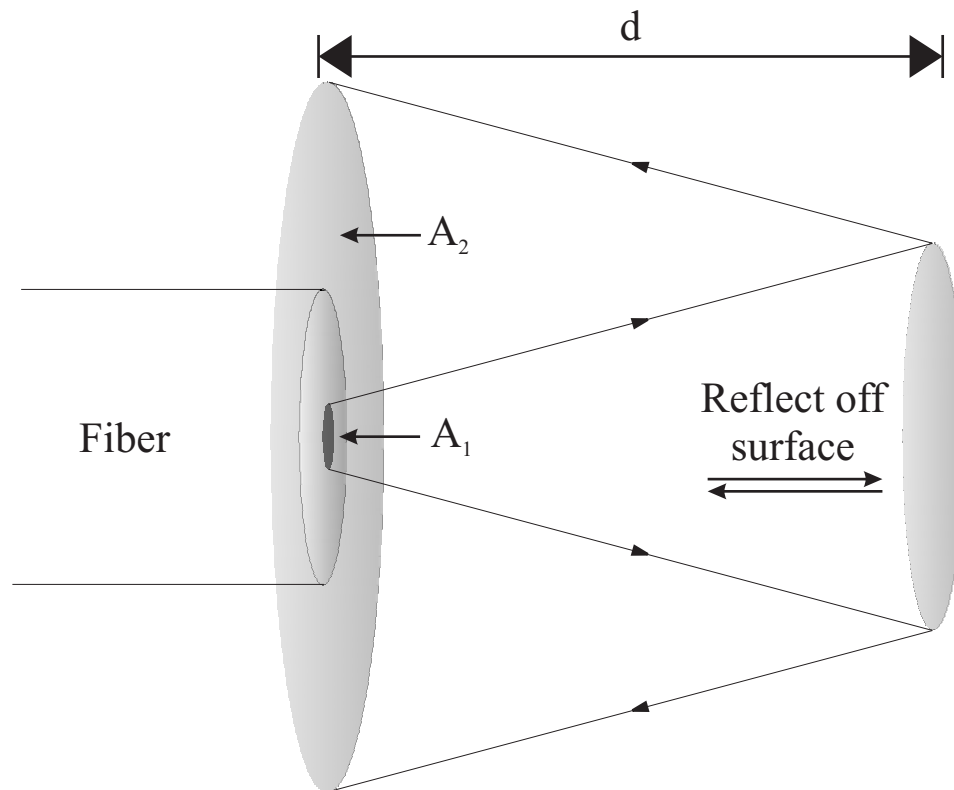


Figure 3.10: Representation of the light lost due to the escape angle out of the optical fiber.

(see Fig. 3.10). According to the specifications for the optical fiber, the numerical aperture is 0.15 which gives a light cone of 8.6 degrees at the cleaved end of the fiber ($NA = \sin \theta$, where θ is the maximum angle of the light cone). As the light travels away from the fiber, it loses intensity. It is assumed that when the light bounces off the cantilever, it reflects completely. Now the beam is traveling back towards the fiber. When the beam reaches the fiber it will have traveled a total distance of $2d$ and occupy an area given by:

$$A' = \pi (2d \tan(\theta/2))^2. \quad (3.100)$$

The fact that the distance, d , enters the equations is what gives the interferometer the ability to measure the cantilever displacements. It can be determined how the electric field falls off with the area by using eq. 3.93.

$$\frac{E_1}{E_2} = \sqrt{\frac{A_2}{A_1}}. \quad (3.101)$$

The above equation is used for the purpose illustrate that the electric field, E_1 and E_2 , falls off inversely with the two areas, A_1 and A_2 . Applying this to the beam bouncing off the cantilever and traveling back towards the fiber, the electric field amplitude can be calculated as,

$$E_T^- = \sqrt{\frac{A}{A'}} E_T = \sqrt{\frac{A}{\pi (2d \tan(\theta/2))^2}} E_T \quad (3.102)$$

where E_T^- indicates the transmitted beam immediately before it re-enters the fiber.

When this beam re-enters the fiber the electric field will again lose some amplitude according to eq. 3.97 where now n_1 is the refractive index of vacuum and n_2 is the refractive index of the optical fiber core. The electric field amplitude of this beam, after it has bounced off the cantilever and re-entered the fiber, will be

labeled E_C . After being transmitted back into the fiber,

$$E_C = 0.8 \sqrt{\frac{A}{\pi (2d \tan(\theta/2))^2}} E_T. \quad (3.103)$$

The beam that has just re-entered the optical fiber will interfere with the beam that bounced off the cleave. The interference pattern generated by these two waves will depend on their relative phases which will be calculated next.

To calculate the phase difference between the two interfering beams, it will be assumed that the electric fields are constant, i.e. the sine waves have constant amplitude. The two waves are both sinusoidal but differ in phase,

$$E_R(t) = E_R \sin 2\pi ft \quad (3.104)$$

$$E_C(t) = E_C \sin(2\pi ft + \phi) \quad (3.105)$$

where f is the laser frequency, t is time and ϕ is the phase difference. The value of ϕ depends on the distance between the end of the fiber and the cantilever, d . There is an additional phase shift of π for the beam that reflects off the cantilever. The extra distance traveled by the wave bouncing off the cantilever is twice the separation such that the path difference is $2d$. The phase shift can be written as,

$$\frac{\phi}{2\pi} = \frac{2d}{\lambda} + \frac{1}{2} \quad (3.106)$$

or

$$\phi = \frac{4\pi d}{\lambda} + \pi. \quad (3.107)$$

Determining the amplitude of the resulting electric field E_0 is aided by the use of a phasor diagram shown in Fig. 3.11. The law of cosines can be used to calculate the resulting electric field amplitude, E' , from the interference of the two waves

$$E'^2 = E_R^2 + E_C^2 - 2E_R E_C \cos\left(-\frac{4\pi d}{\lambda}\right). \quad (3.108)$$

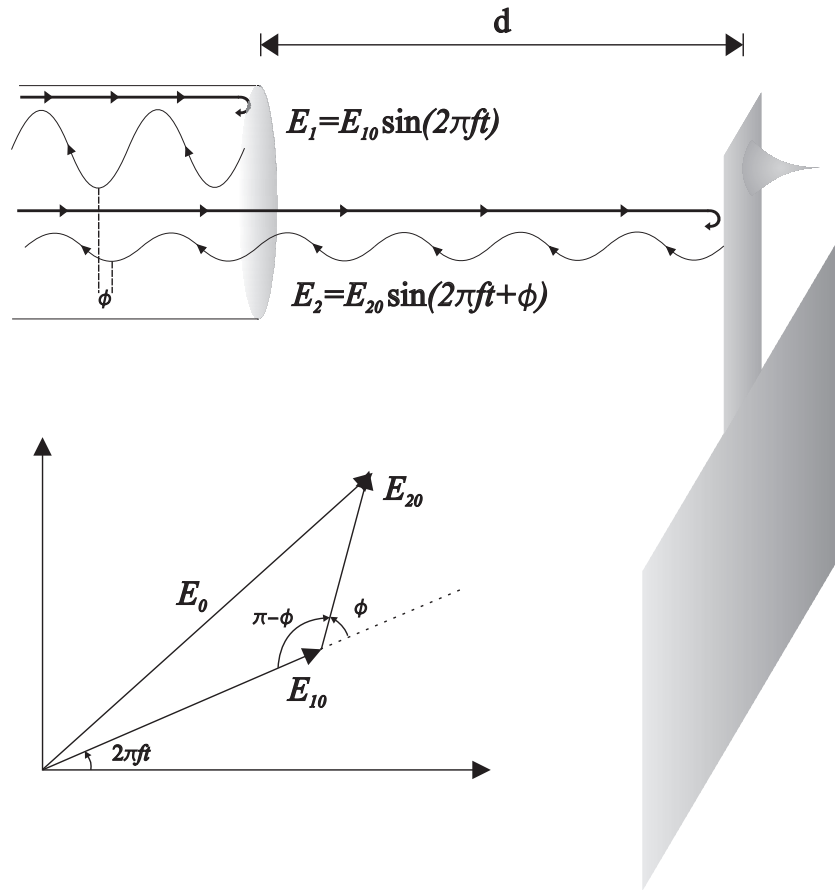


Figure 3.11: Phasor diagram for the interference pattern from the fiber-optic interferometer.

Eq. 3.92 can be used to calculate the output power, P' , (i.e. interference pattern) of the interferometer,

$$P' = \frac{1}{2} c \epsilon_r \epsilon_0 E'^2 A. \quad (3.109)$$

Fig. 3.12 shows a plot of Eq. 3.109 in two different regimes: Fig. 3.12(a) shows the power dependence on short separations and Fig. 3.12(b) shows the power dependence for longer distances.

These two plots capture many of the experimentally observed characteristics shown in Fig. 3.13 – the output power is within a factor of two of experimentally observed values. There is a DC offset that increases with decreasing separations, and there is a sharp decrease in the fringe visibility for small separations and a slower decrease in the fringe visibility for larger distances. It is particularly satisfying that the value of the output power is approximately correct.

The bumps in the decay seen in Fig. 3.13 are likely due to small angular motions of the coarse approach as it moves. The coarse approach is detailed in Sec. 3.6.4. There could also be regions of laser mode hopping, which is discussed below.

For cantilever motions, the interferometer must be “tuned” to the maximum sensitivity. The maximum sensitivity for small displacements ($\Delta d \ll \lambda/2$) is obtained by tuning the interferometer to the maximum slope of this intensity. This can be achieved two different ways: First, the distance can be varied, and second, the wavelength can be changed (e.g. by tuning the temperature of the laser diode). When tuned to the center of a fringe, the interferometer responds linearly, yielding a conversion factor between distance and intensity. The maximum slope of this function is

$$2E_R E_C \frac{4\pi}{\lambda}. \quad (3.110)$$

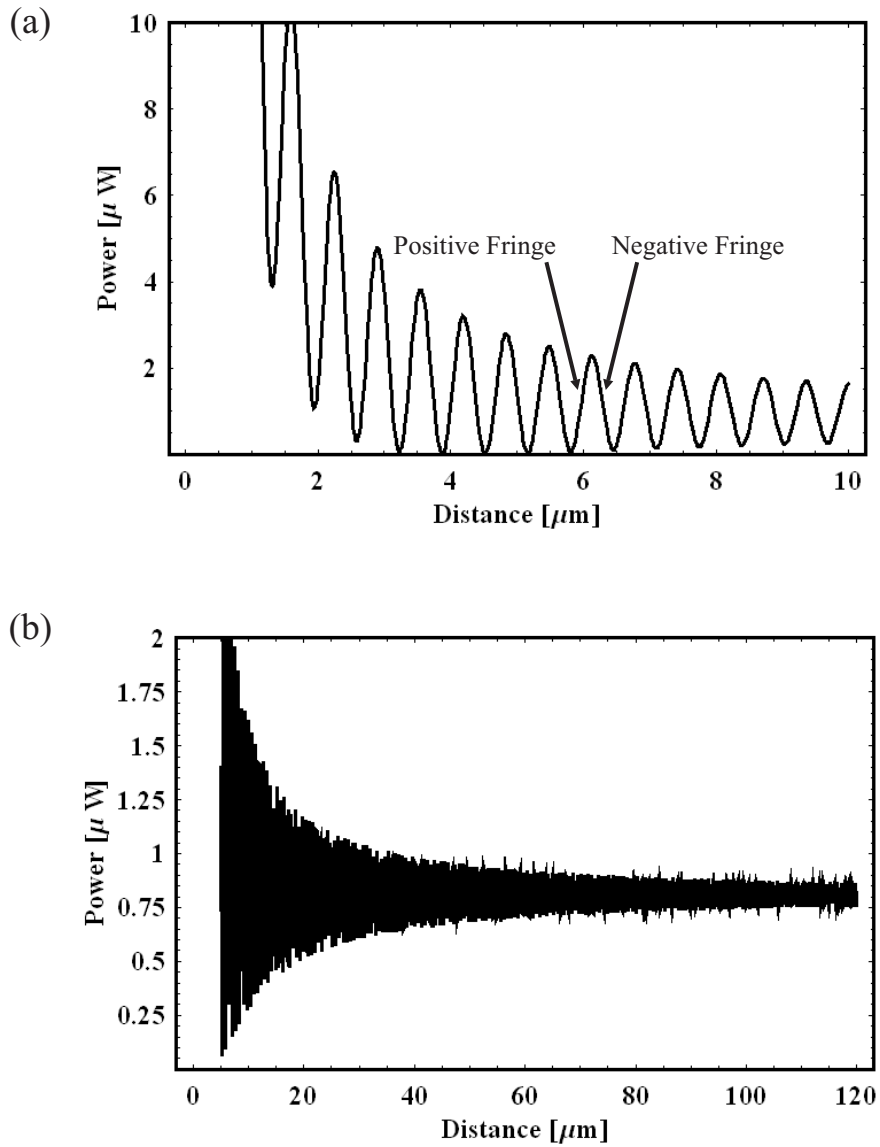


Figure 3.12: (a) Plot of the interference pattern for displacement close to the cleaved end of the fiber and (b) Plot of the interference pattern for a large displacement from the cleaved end of the fiber.

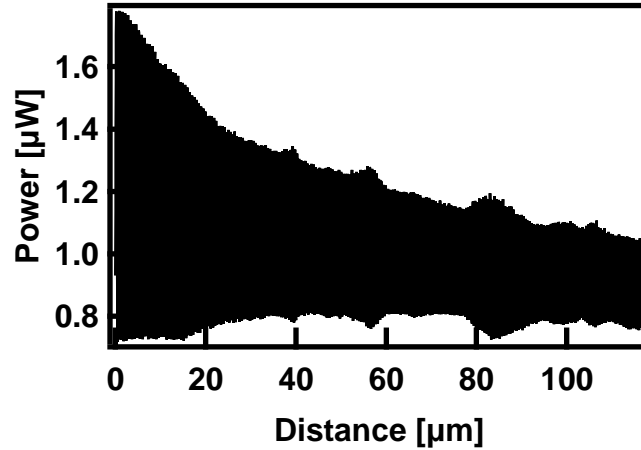


Figure 3.13: Plot of the interference generated by watching the coarse approach move away from the fiber.

As a practical matter, the the conversion factor between distance and interferometer voltage can be obtained by measuring this slope. Sweeping out at least one full fringe and using the measured peak-to-peak voltage (V_{pp}) from the photodiode output ($V_{pp} \Leftrightarrow 4E_{10}E_{20}$) yields the conversion factor,

$$\frac{2\pi V_{pp}}{\lambda}. \quad (3.111)$$

Varying the temperature of the laser diode is another way of tuning the interferometer to the sensitive region of the interferometer fringe. This is easily seen by considering the wavelength dependence of Eq. 3.108. The laser diode wavelength changes with temperature according to its temperature coefficient, $\Delta\lambda/\Delta T = 0.67 \text{ nm}/^\circ\text{C}$. Obtaining a complete fringe with a typical temperature sweep of the laser diode (50°C) requires a separation of $d = 50\mu\text{m}$.

Mode Hopping The fiber-optic interferometer can observe motions as small as $10\text{m}\text{\AA}/\sqrt{\text{Hz}}$. Unfortunately, mode hopping in the laser diode creates unwanted noise in the form of sudden shifts in the DC output of the photodiode. These DC

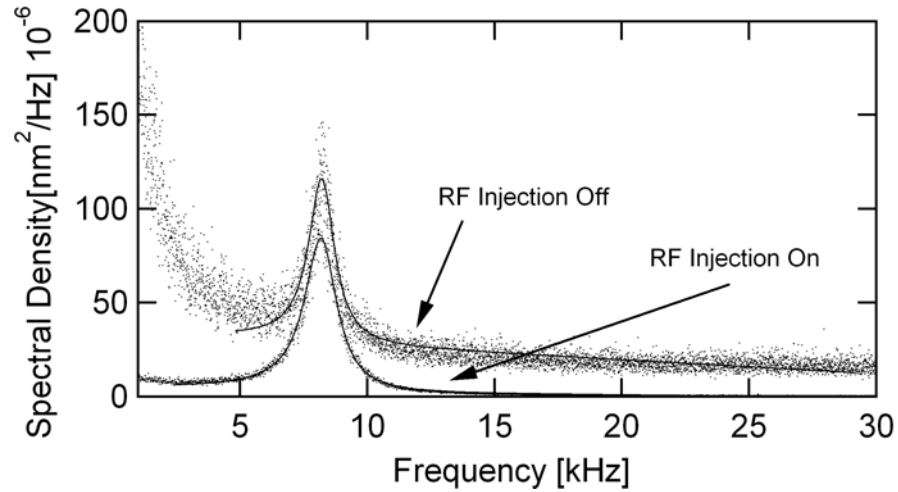


Figure 3.14: The spectral density of the thermal motion of a 1N/m cantilever with and without the RF injection used in the interferometer circuit.

jumps have a broad power spectrum that greatly affects the minimum detectable displacement, or noise floor, of the interferometer near the cantilever frequency. A solution to this problem has been successfully implemented on the suggestion of Dan Rugar, namely to inject a radio frequency (RF) modulation to the current driving the laser diode [22–24].

The RF is generated using a Mini-Circuits POS-300 which outputs a sine wave with typical values of 200 MHz at 10 dBm. This however is not a complete fix to the problem as there are temperature ranges of the laser diode that still produce a significant amount of noise. The noise always seems to be slightly less on a positive slope of the interferometer fringe. The effect of the RF frequency and power on the noise floor of the interferometer was characterized. The RF injection simply removes the adverse effects of mode hopping. The cantilever was pointed at a commercial Silicon Nitride cantilever with spring constant of 0.01 N/m with a separation of approximated 50 μm . The noise floor was calculated as a function

of RF power and RF frequency according to the procedure outlined at the end of section 3.3. For these measurements, the RF was sourced from an HP function generator (model HP8656B). The dramatic effect that the RF injection can have on the noise floor can be seen visually in the power spectral densities plotted in Fig. 3.14. Fig. 3.15(a) and Fig. 3.15(b) show plots of the interferometer noise floor as a function of injected RF frequency and power, respectively. In Fig. 3.15(a), the (+) sign indicated that the interferometer was tuned on the positive slope of the interferometer fringe; conversely, the (-) indicated being tuned to negative fringe. From the two plots it is clear that the best operating point is to have the RF injection frequency at ~ 200 MHz, the power at ~ 10 dBm, and the interferometer tuned to a positive fringe.

Figure 3.16(a) shows the interferometer output signal versus the temperature of the laser diode. Maximum sensitivity is achieved by tuning the temperature of the laser diode to the linear-response region of the curve [15]. By using RF current injection to eliminate mode-hopping instabilities in the interferometer's diode laser, the interferometer's noise floor (minimum detectable displacement) can be as good as $\sim 10 \text{ m}\mathring{\text{A}}/\sqrt{\text{Hz}}$ at a typical fiber-separation of $50 - 100 \mu\text{m}$. Figure 3.16(b) shows the interferometer output signal as a function of time for a cantilever whose peak-to-peak amplitude is larger than the linear-response of the interferometer (160 nm gives a 10% error). In each case the peak-to-peak voltage, V_{pp} , is the same and can be used to calibrate the cantilever displacement. In the linear response regime, the sensitivity is given by, $2\pi V_{\text{pp}}/\lambda$, where λ is the laser wavelength. The interferometer output for a cantilever undergoing only random thermomechanical motion is shown versus time in Fig. 3.16(c). The corresponding averaged power spectrum is shown in Fig. 3.16(d). The area under this power

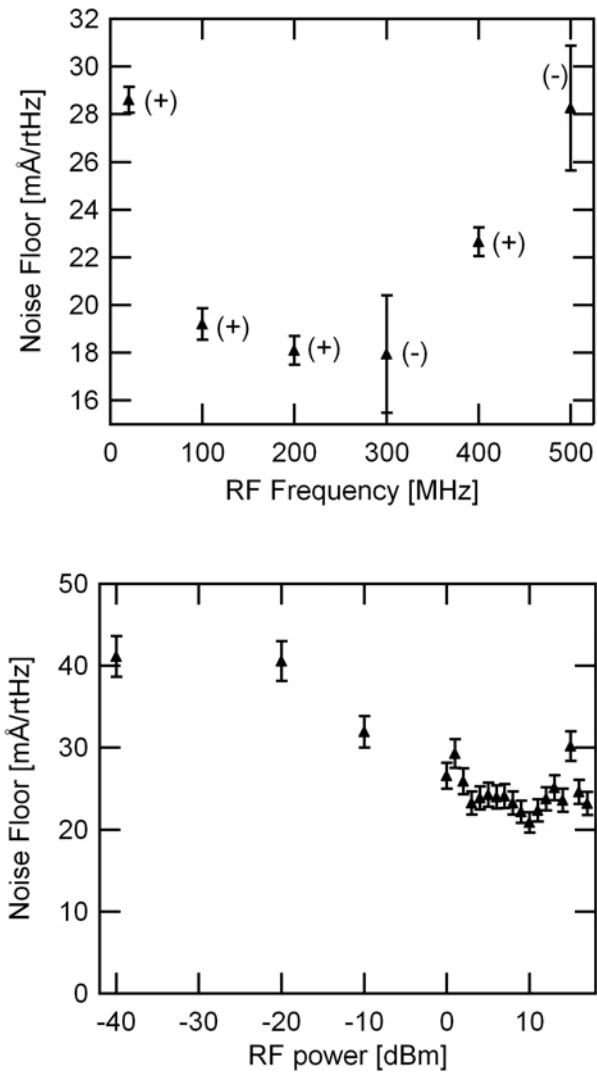


Figure 3.15: (a) The noise floor dependence on injected RF frequency with the RF power held fixed at 10dBm and (b) The noise floor dependence on injected RF power with the RF frequency held at 200MHz.

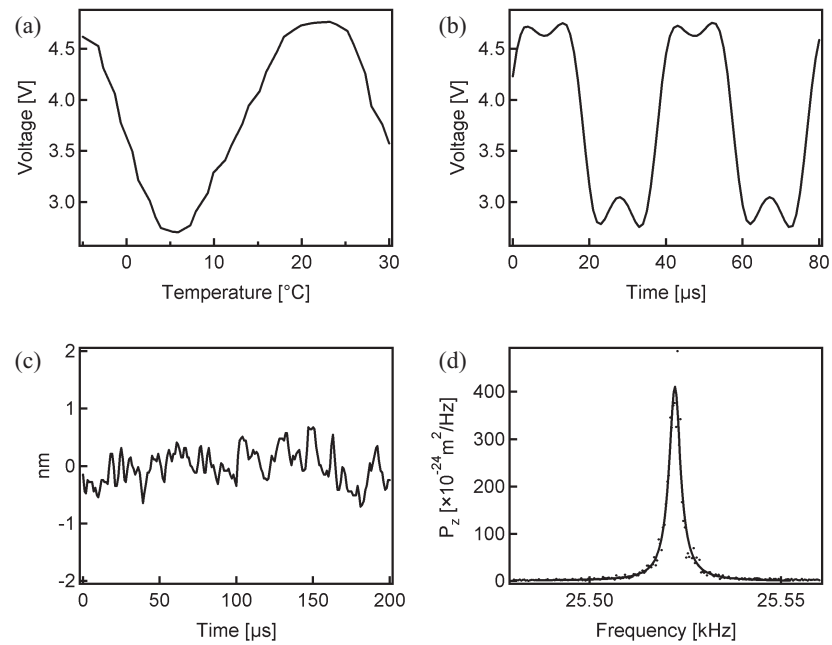


Figure 3.16: (a) Interferometer output signal versus laser diode temperature, (b) Interferometer output signal versus time for an over driven cantilever, (c) Thermal motion of a 1N/m cantilever, and (d) Power spectrum of the thermal motion of the cantilever.

spectrum, equal to $k_B T/k$, can be used to determine the cantilever spring constant if the cantilever's temperature is known [25].

Model	Description	Price
ILX Lightwave	Ultra low-noise current source	\$3,000
ILX Lightwave	Laser diode temperature controller	\$2,000
New Focus	Photodiode	\$1,500
Laser Diode	Fabry-Perot laser diode	\$2,000
Mini-Circuits	Bias-T for RF injection	\$100
Metrotek	10/90 Optical coupler with FC/APC pigtails	\$2,000
Mini-Circuits POS-300	RF source	\$80
ILX Lightwave	Laser Diode mount	\$1,500

3.6.3 Frequency Shift Detection

The force gradient between the cantilever and the sample surface is detected by measuring the resonance frequency [26] of the cantilever according to,

$$\frac{\Delta f}{f_0} = -\frac{1}{2k} \frac{\partial F}{\partial z} \quad (3.112)$$

where Δf is the frequency shift about the natural resonance frequency, f_0 , and z is the tip surface separation. The cantilever is self-oscillated near its resonance frequency with a positive feedback phased-locked loop (PLL). There have been two versions of the circuitry used to drive the cantilever and demodulate the frequency. The first is an implementation using an analog PLL that also demodulates the frequency. The second circuit is very similar except that the PLL is replaced with a comparator and the demodulation is done by a commercially available frequency

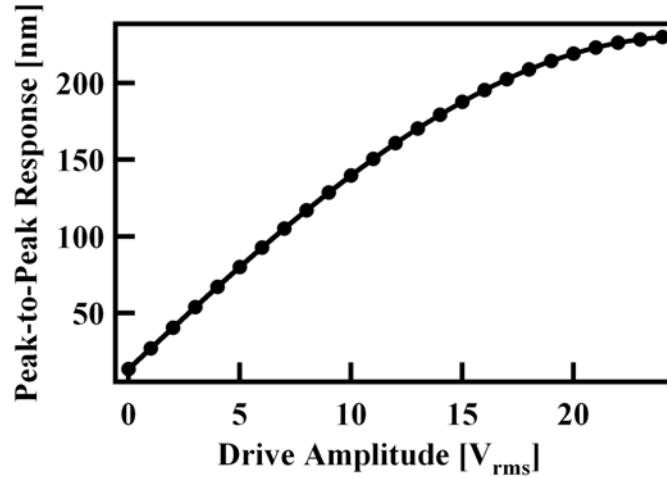


Figure 3.17: Cantilever response to drive piezo amplitude. Notice the non-linearity due to exceeding the linear range of the fiber optic interferometer.

counter. The cantilever is driven using a bender piezo that is mounted beneath the cantilever base. There are two small sapphire plates that electrically isolate the piezo from the coarse approach and the cantilever. The response of the cantilever on resonance to the drive amplitude of the piezo is shown in Fig. 3.17

Analog Positive-Feedback Circuit. An analog positive feedback circuit was first designed because the components are cheap and the possibility of modulating the frequency shift would be feasible. The circuit is shown in Fig. 3.18.

The input interferometer signal is AC coupled, then bandpass filtered with a simple LCR filter. The calculated transfer function of the LCR circuit is shown in Fig. 3.19 and is centered on the cantilever's resonance frequency. The filter has a Q of about 40 (adding a resistor lowers the Q). The width of the filter's resonance is much smaller than the width of the cantilever resonance in vacuum, i.e. the filter's Q is much smaller than the cantilever Q. The signal is routed to an LM565

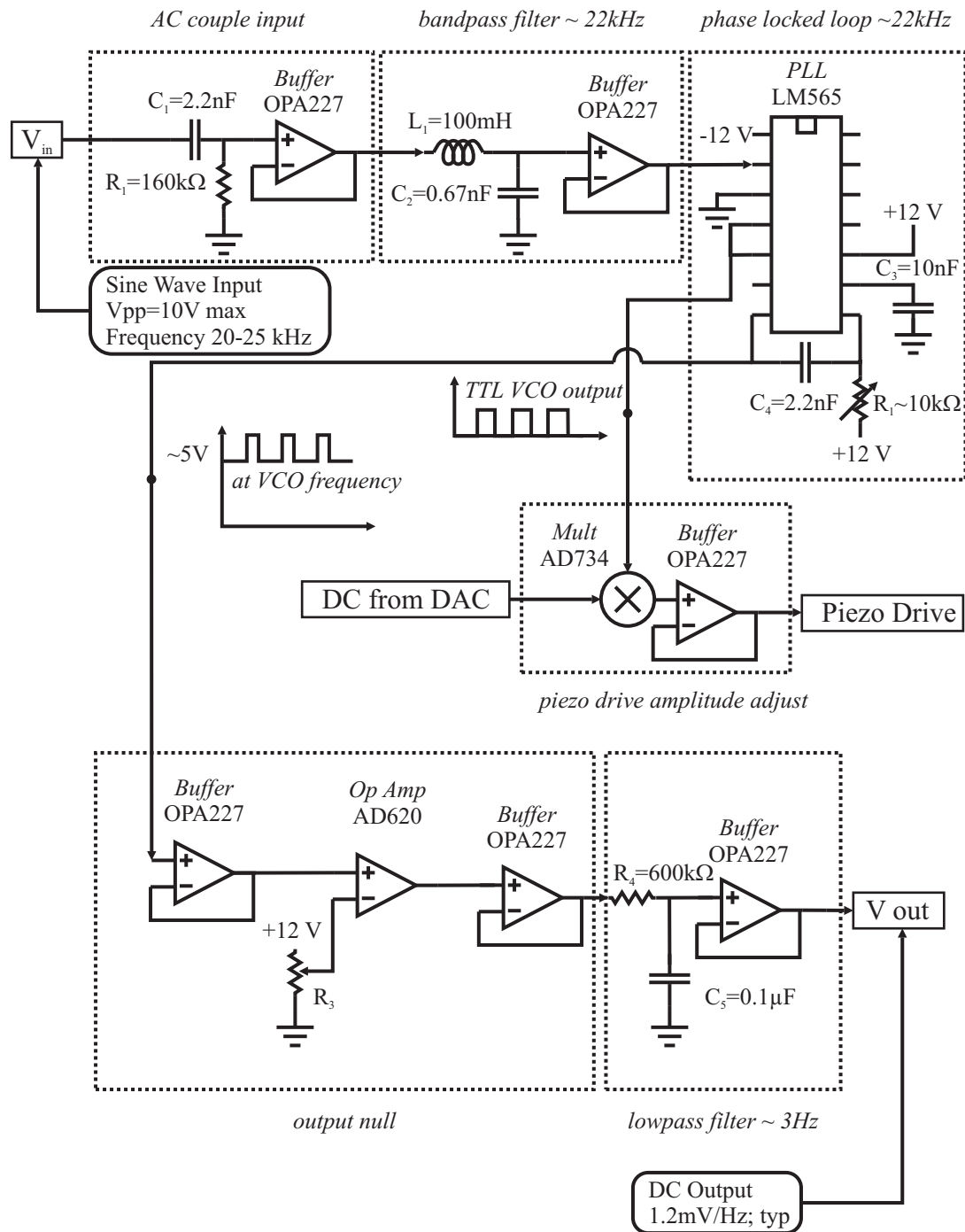


Figure 3.18: Analog frequency demodulation circuit.

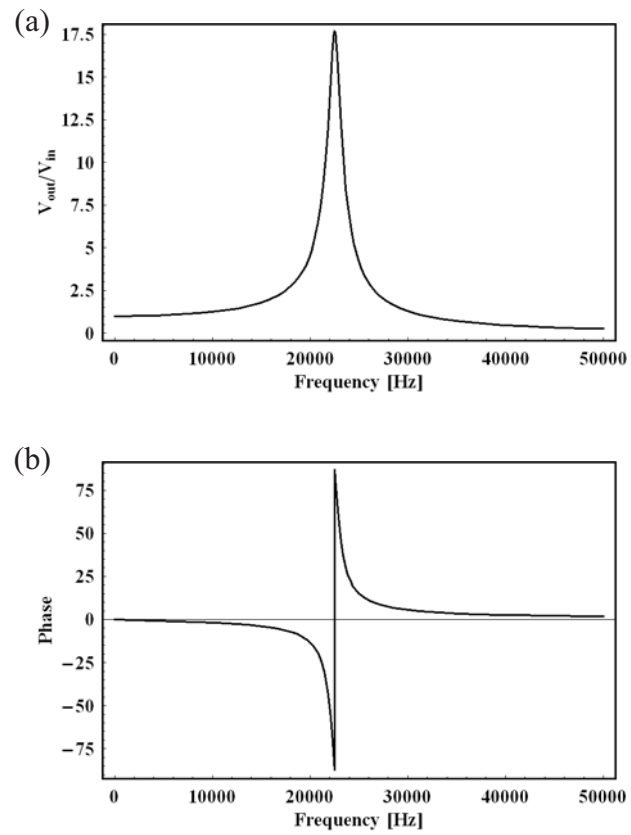


Figure 3.19: The gain (a) and the phase (b) of the bandpass filter used in the positive feedback circuit.

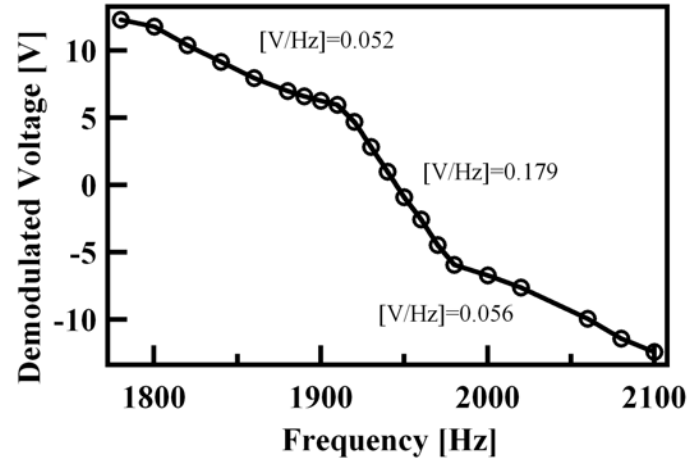


Figure 3.20: Sensitivity of analog frequency demodulation using a phase locked loop.

PLL, which determines the cantilever frequency. The free running frequency of the PLL is set near the cantilever frequency by R2 and C3. Once the PLL is locked, the voltage on the voltage controlled oscillator (VCO) follows the cantilever frequency. This voltage is a square wave at the cantilever frequency. A change in the cantilever frequency will cause both a duty cycle change and a DC offset in the square wave output. Low pass filtering the output and nulling provides a DC voltage proportional to the cantilever frequency. The proportionality constant has three regimes that can be seen in Fig. 3.20 and is also dependent on the free running frequency of the VCO. The VCO output is used to drive the cantilever. The VCO output is multiplied by a DC voltage, provided by the computer DAQ card, to control the amplitude of the cantilever driving force. It is tricky to get the PLL to lock onto the cantilever. The resistor, R2, must be adjusted by hand until the cantilever is driven with maximum response. The drift of this demodulated output over time is shown in Fig. 3.21. The drift of ~ 4 Hz peak-to-peak can be explained by considering the temperature coefficient of the LM565 PLL clock

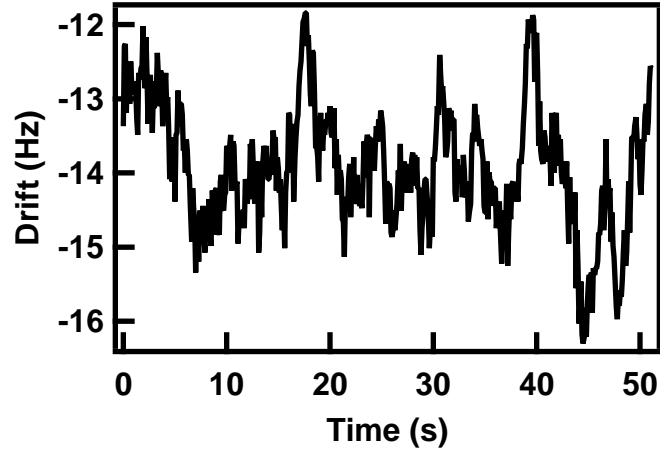


Figure 3.21: The drift in the analog PLL demodulated output.

which is $100\text{ppm}/^{\circ}\text{C}$. At a frequency of 21kHz the observed drift could be due to a temperature change of only 2°C . This performance is similar to that observed by Dürig et. al. with their analog PLL [27].

Positive feedback circuit using a frequency counter. The circuitry is essentially identical to the analog frequency shift detection scheme. The PLL is replaced with a digital comparator which creates a square wave at the cantilever frequency. The square wave is altered in the same fashion as with the analog circuit and sent to the cantilever drive piezo. The square wave is also sent to a Stanford Research Systems SR620 frequency counter. There is also the addition of a RC low pass filter placed on the input that serves to change the phase of the signal. The phase is adjusted so that the positive feedback is at a maximum. This assures that the drive is on resonance and that is 90° out of phase with the response.

The performance of this circuit is determined by measuring the jitter (standard deviation of the frequency) of the cantilever frequency within a given bandwidth. Fig. 3.22 shows the jitter versus gate time and bandwidth of the frequency counter.

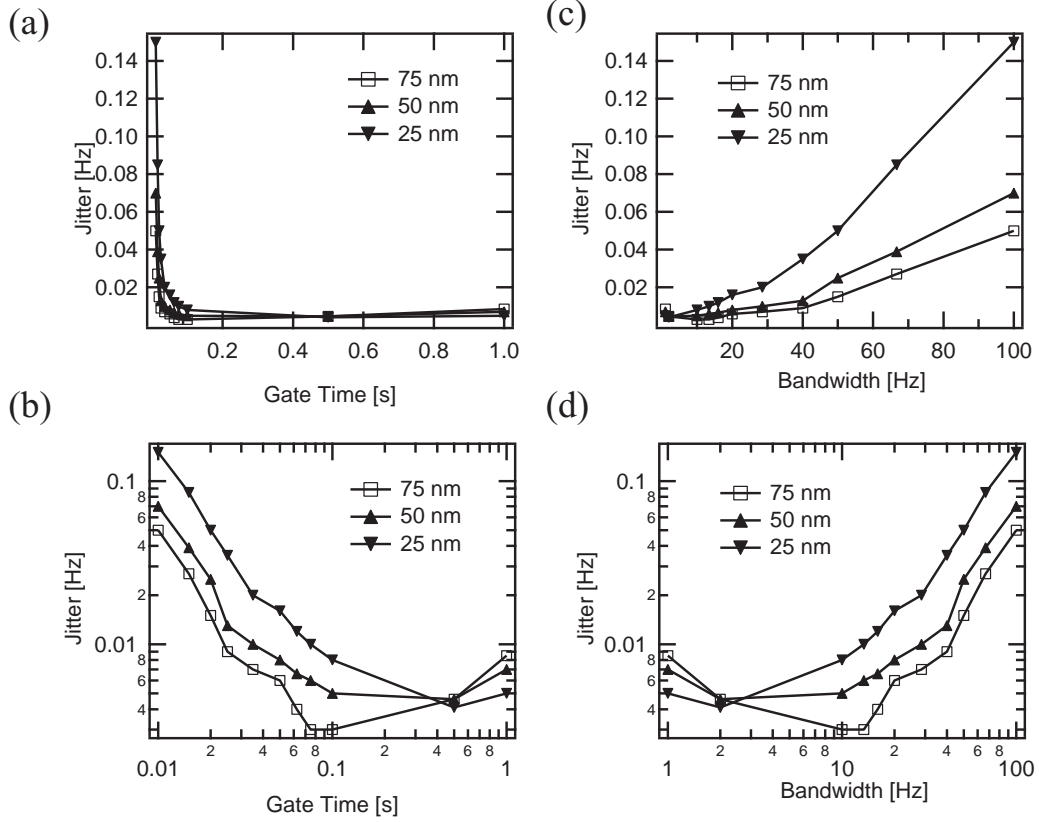


Figure 3.22: Plot of the frequency jitter versus gate time and bandwidth

The minimum detectable force gradient is given by [26],

$$\delta F'_{\min} = \sqrt{\frac{2kk_B T \Delta f}{2\pi f_0 Q \langle z_{\text{osc}}^2 \rangle}} \quad (3.113)$$

where $\langle z_{\text{osc}}^2 \rangle$ is the mean-square drive amplitude. The plots in Fig. 3.22 have a $1/\langle z_{\text{osc}} \rangle$ dependence suggesting that the positive feedback detection system is thermally limited.

3.6.4 Coarse Approach

The coarse approach was developed in the Marohn Lab at Cornell University, and the reader is directed to Silveira and Marohn for a more detailed description [28]. The main advantages of this design are its simplicity, reliability and there

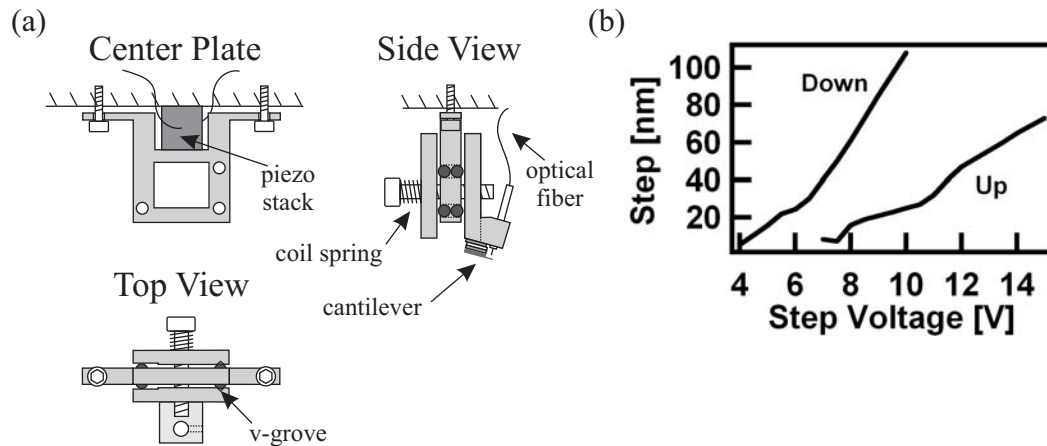


Figure 3.23: (a) Schematic views of the coarse approach mechanism. The upper left drawing shows only the center plate. The two other view show the coarse approach fully assembled. (b) The average step size versus the applied sawtooth voltage amplitude from both up and down motion.

are no requirements for glue, which makes it well suited for variable-temperature applications.

The coarse approach is diagramed in Fig. 3.23(a) and consists primarily of three sandwiched brass plates. The center plate is rigidly held down by leaf springs which allow small vertical movements by a small piezo (Fig. 3.23(a)). The outer two plates are sandwiched around the center plate and held in place through tension provided by a coil spring. The outer plates glide on small sapphire balls that are embedded in the center plate. On the left-inner side of the outer plate, two sapphire balls ride in a vertical v-groove which defines the glide direction. On the right side of the outer plate, one sapphire ball rides on a flat surface which defines the plane. A saw-tooth voltage is sent to piezo. The slow ramping portion of the saw-tooth voltage slowly pushes the inner and outer plates forward. This is the “stick” portion of the slip-stick motion. The sharp edge of the saw-tooth

voltage will quickly jerk the center plate backwards, but the outer plates will not follow. This is the “slip” portion of the slip-stick principle. Repeated application of the saw tooth voltage will move the plates forward in steps ranging from 5nm to > 100 nm depending on the amplitude and frequency of the saw tooth voltage. Movement in the opposite direction is achieved by simply reversing the saw tooth waveform, such that it begins with sharp jump followed by a slow ramp. It should also be noted that the coil spring is not compressed exactly the same each time the coarse approach is reassembled resulting in slight variations to the step sizes.

The fine motion is also handled by the coarse approach mechanism. The outer plates will track the movement of the center plate so long as it never breaks friction. This is normally true for motions at typical scanning speeds. To prevent accidentally taking a coarse step during scanning, a 150Hz low pass filter is used.

The coarse approach moves vertically in both directions from 4K to 300K.

The performance at room temperature is shown in Fig. 3.23(b) and is mainly characterized by the voltage amplitude of the sawtooth required to obtain a given step size. Notice from the plot in Fig. 3.23(b) that downward steps require slightly less voltage than upward steps. These voltages change slightly for each different experiment because the tension in the fiber and other wires connected to the coarse approach place a torque on the coarse approach plates that changes the friction. Too much torque on the plates can cause the coarse approach to stop moving all together. The optical fiber that monitors the cantilever motion is largely responsible for this torque. The jacketing on the fiber is carefully stripped off, ensuring that the polymer coating remains on and undamaged, for at least 10 cm above the end of the fiber. The result is that the fiber has adequate flexibility while maintaining its strength. Without the polymer coating the glass will become very

brittle.

When properly assembled, with no unnecessary torque applied to the plates, the coarse approach works very reliably. The fine approach also has sufficient scan range to compensate for any tilt in the sample and is stable.

3.6.5 Scanning

The scanning is divided into two parts: lateral scanning and vertical scanning. The sample is scanned in the x and y directions and the cantilever is scanned in the z -direction. The z -motion is handled by the coarse approach mechanism just described. The x and y motions are performed by a home built implementation of a scanner design introduced by Siegel *et al.* [29]. The design enables a larger scan range for a given length of the piezo than a traditional tube scanner.

To keep the whole microscope compact, a non-traditional scanner design was used instead of the traditional tube scanners. Tube scanners require exceedingly long tube piezo to achieve a scan range of 50 μm . The design introduced by Siegel *et al.* has the benefit of remaining compact while maintaining a large scan range. Instead of tube piezo, the design uses 4 “s bender” piezos, aptly named because they bend in a “s” shape. Two of the piezos move the scanner in the x direction while the other two move it in the y direction.

Each of the piezos is held together by three small, fragile macor pieces. Macor is chosen because it has a similar thermal expansion coefficient similar to piezo ceramic material and it is electrically insulating. One end of each of the two x piezos is glued to the top macor piece, which is rigidly attached to the microscope frame. One end of the x piezos is glued to this piece. The other end of the x piezos is glued to the second macor piece (as seen at the bottom of the scanner in

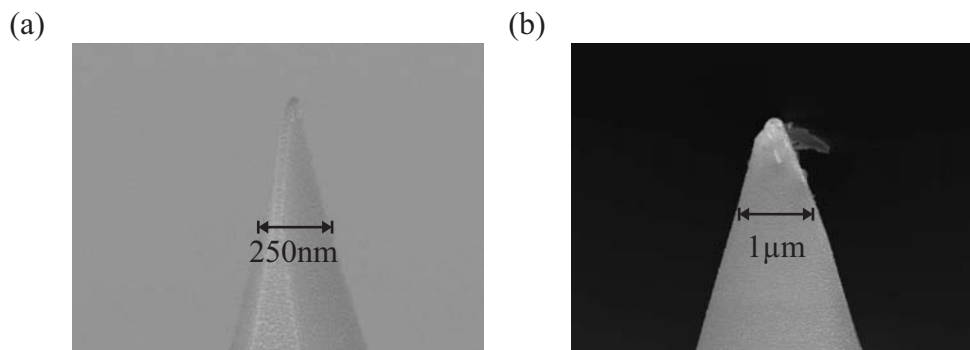


Figure 3.24: (a) The tip of the cantilever prior to use and (b) the cantilever tip after use, including several crashes into the surface.

Fig. 3.8). The bottom end of the y piezos are also glued to this piece. The top of the y piezos are glued to the third major piece on which the sample is mounted (can be seen at the top of the scanner in Fig. 3.8). The image of one glider chair mounted inside another chair illustrates the concept.

3.6.6 Cantilever

The central component of the microscope is the cantilever, which sets the force sensitivity as well as the spatial resolution. The force sensitivity is determined by the cantilever response to thermal fluctuations as described in Sec. 3.3. The cantilever used in the trap imaging experiments has a force constant of 1 N/m , a resonance frequency of $\sim 24 \text{ kHz}$, a quality factor of $Q \sim 10,000$ in vacuum. The cantilever is coated with a thin layer of platinum (with an iridium adhesion layer) and has a tip radius of about 50 nm . Crashing the tip (vertical deflection of about 100 nm) into the sample can have disastrous effects on the tip radius and the resolution. This can be seen by comparing the two SEM pictures of a cantilever before and after being used and crashed multiple times in Fig. 3.24. It is clear that care must be taken in controlling the cantilever's position in space, not allowing it

to crash into the surface.

3.7 Measurement Techniques

The microscope employs a commercial metal coated cantilever, works with the sample at room temperature and in the dark, and operates at high vacuum (10^{-6} mbar) for highest sensitivity. Instead of measuring the cantilever amplitude, whose response time can be deleteriously long (many seconds) in vacuum, we follow instead the cantilever resonance frequency, which responds instantaneously to changing electrostatic force gradients [26],

$$\Delta f = f - f_0 \approx -\frac{f_0}{4k} C'' (V_{\text{tip}} - \phi)^2 \quad (3.114)$$

Here f_0 is the natural resonant frequency of the cantilever and k is cantilever spring constant. The cantilever frequency depends on the voltage V_{tip} applied to the cantilever, on ϕ , the contact potential difference between the tip and the sample, and on $C'' = \partial^2 C / \partial z^2$, the second derivative of the tip-sample capacitance with respect to z , the tip-sample separation. The approximation used to derive Eq. 3.114 holds when electrostatic force gradients are small compared to the mechanical spring constant of the cantilever, which is the case here. Figure 3.25 shows a plot of cantilever resonance frequency versus tip voltage acquired at a point over the pentacene transistor gap with the source, drain, and gate grounded. The observed parabola was fit to Eq. 3.114 to obtain C'' and ϕ at that point. This procedure can in principle be repeated at each point to build up an image of C'' and ϕ . In practice we find that Δf is dominated by, depending on experimental conditions, either the variation in C'' or ϕ alone. This simplifies data acquisition and analysis considerably. For example, if C'' is constant, then we can infer the local contact

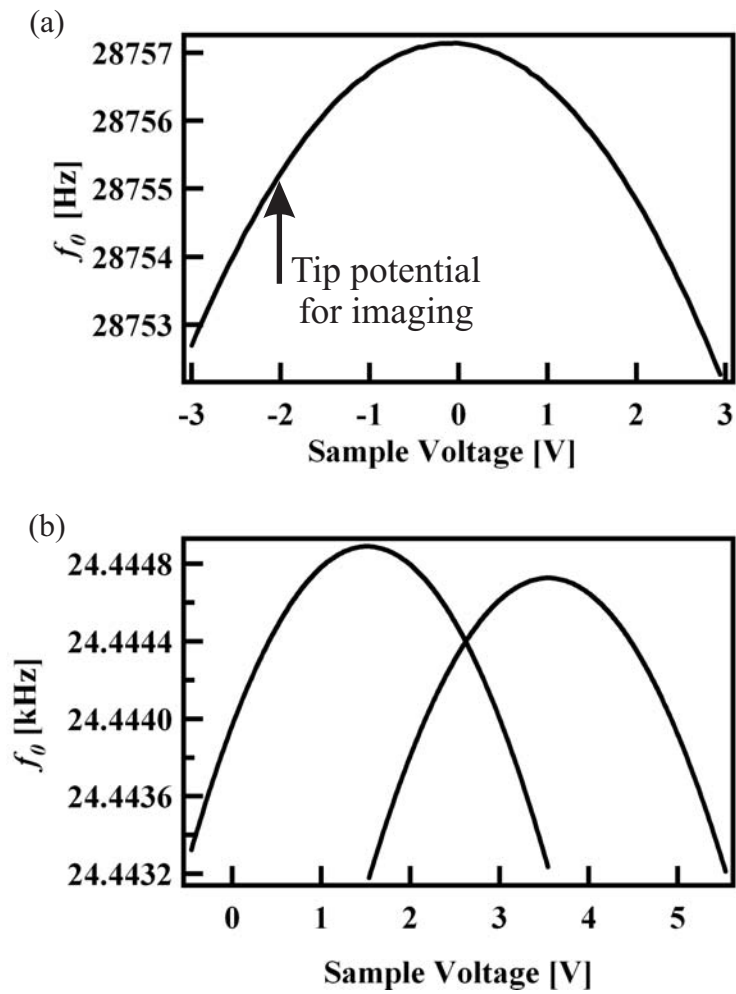


Figure 3.25: (a) The cantilever resonance frequency versus the tip-sample voltage. (b) The effect of a potential change on the sample.

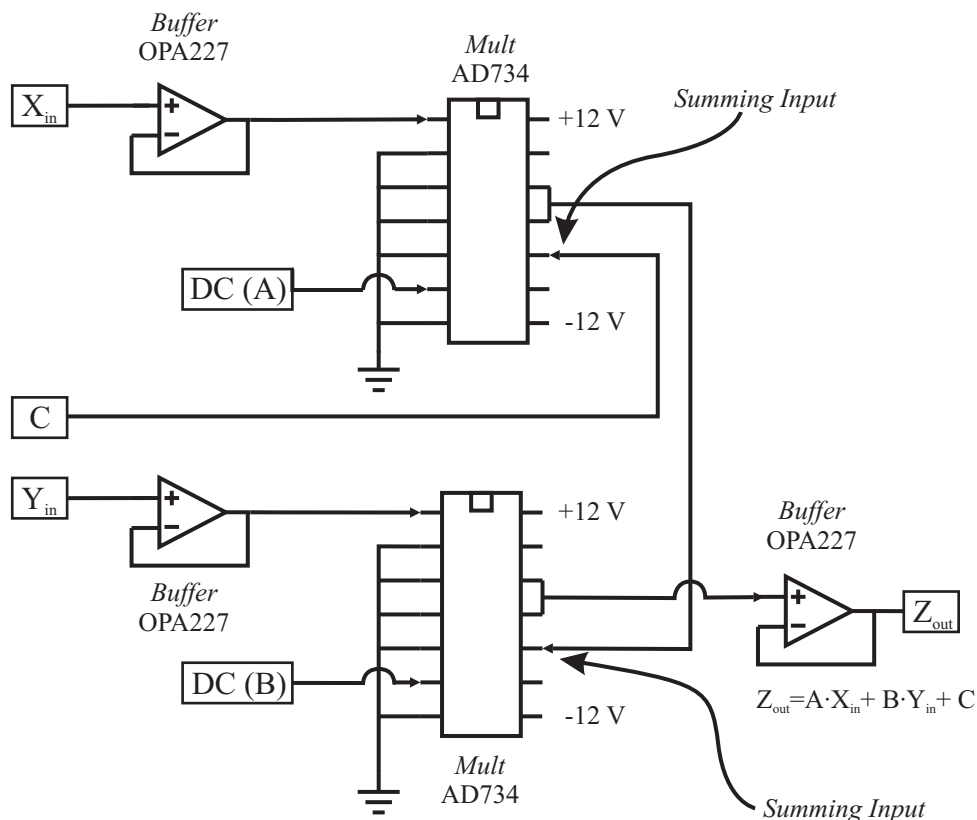


Figure 3.26: The circuit used to scan the tip in plane above the sample surface.

potential from an image of Δf acquired at constant V_{tip} using

$$\Delta\phi \approx \frac{\Delta f}{f_0} \frac{2k}{C'' V_{tip}}. \quad (3.115)$$

Imaging is done by fixing the tip voltage and recording the resonance frequency. Because of the bandwidth limitation of the frequency counter, the scan rate cannot be faster than 16Hz. Faster scanning is possible but then noise in the frequency increases. All EFM images are done in non-contact mode where the tip is scanned in a fixed plane above the surface. The plane is used to compensate for sample tilt and is either implemented in software or hardware. The circuit for the hardware implementation is shown in Fig. 3.26. This circuit simply determines a plane

according to the equation,

$$Z_{out} = A \cdot X_{in} + B \cdot Y_{in} + C \quad (3.116)$$

The coefficients, A and B , are DC voltages provided by the auxiliary outputs of the lock-in amplifier. The height above the sample surface is set by C . The scan coordinates, X_{in} and Y_{in} , are supplied by the DAQ card. All inputs are prior to any piezo amplifiers. The plane is determined by adjusting A and B until the scan appears flat. This circuit is quite easy to use and very stable.

References

- [1] G. Binnig, C. Quate, and C. Gerber, "Atomic force microscope," *Phys. Rev. Lett.*, vol. 56, no. 9, pp. 930–933, 1986.
- [2] L. Burgi, T. Richards, M. Chiesa, R. H. Friend, and H. Sirringhaus, "A microscopic view of charge transport in polymer transistors," *Synth. Met.*, vol. 146, no. 3, pp. 297–309, 2004.
- [3] E. M. Muller and J. A. Marohn, "Microscopic evidence for spatially inhomogeneous charge trapping in pentacene," *Adv. Mater.*, vol. 17, no. 11, pp. 1410–1414, 2005.
- [4] C. Schönenberger and S. Alvarado, "Observation of single charge carriers by force microscopy," *Phys. Rev. Lett.*, vol. 65, no. 25, pp. 3162–3164, 1990.
- [5] T. Krauss and L. Brus, "Charge, polarizability, and photoionization of single semiconductor nanocrystals," *Phys. Rev. Lett.*, vol. 83, no. 23, pp. 4840 – 4843, 1999.
- [6] T. Krauss, S. O'Brien, and L. Brus, "Charge and photoionization properties of single semiconductor nanocrystals," *J. Phys. Chem. B*, vol. 105, no. 9, pp. 1725–1733, 2001.
- [7] R. Ludeke and E. Cartier, "Imaging of trapped charge in SiO_2/Si and at the SiO_2/Si interface," *Appl. Phys. Lett.*, vol. 78, no. 25, pp. 3998–4000, 2001.
- [8] C. Schönenberger and S. F. Alvarado, "Probing single charges by scanning force microscopy," *Mod. Phys. Lett. B*, vol. 5, no. 13, pp. 871–6, 1991.

- [9] K. P. Puntambekar, P. V. Pesavento, and C. D. Frisbie, "Surface potential profiling and contact resistance measurements on operating pentacene thin-film transistors by kelvin probe force microscopy," *Appl. Phys. Lett.*, vol. 83, no. 26, pp. 5539–5541, 2003.
- [10] J. A. Nichols, D. J. Gundlach, and T. N. Jackson, "Potential imaging of pentacene organic thin-film transistors," *Appl. Phys. Lett.*, vol. 83, no. 12, pp. 2366–2368, 2003.
- [11] W. R. Silveira and J. A. Marohn, "Microscopic view of charge injection in an organic semiconductor," *Phys. Rev. Lett.*, vol. 93, no. 11, p. 116104, 2004.
- [12] W. Silveira, E. Muller, T. Ng, D. Dunlap, and J. Marohn, "High-sensitivity electric force microscopy of organic electronic materials and devices," in *Scanning Probe Microscopy, in press* (S. Kalinin and A. Gruverman, eds.), 2005.
- [13] A. D. Drake and D. C. Leiner, "Fiber-optic interferometer for remote sub-angstrom vibration measurement," *Rev. Sci. Instrum.*, vol. 55, no. 2, pp. 162–165, 1984.
- [14] D. Rugar, H. J. Mamin, and P. Guethner, "Improved fiber-optic interferometer for atomic force microscopy," *Appl. Phys. Lett.*, vol. 55, no. 25, pp. 2588–2590, 1989.
- [15] K. Bruland, J. Garbini, W. Dougherty, S. Chao, S. Jensen, and J. Sidles, "Thermal tuning of a fiber-optic interferometer for maximum sensitivity," *Rev. Sci. Instrum.*, vol. 70, no. 9, pp. 3542–3544, 1999.
- [16] D. Miller and N. Moshegov, "All-metal ultrahigh vacuum optical fiber feedthrough," *J. Vac. Sci. Technol. A*, vol. 19, no. 1, pp. 386–387, 2001.
- [17] M. Tortonese, H. Yamada, R. C. Barrett, and C. F. Quate, "Atomic force microscopy using a piezoresistive cantilever," in *1991 International Conference on Solid-State Sensors and Actuators, Jun 24-28 1991*, pp. 448–451, 1991.
- [18] G. Meyer and N. Amer, "Novel optical approach to atomic force microscopy," *Appl. Phys. Lett.*, vol. 53, no. 12, pp. 1045–7, 19.
- [19] S. Alexander, L. Hellemans, O. Marti, J. Schneir, V. Elings, P. Hansma, M. Longmire, and J. Gurley, "An atomic-resolution atomic-force microscope implemented using an optical lever," *J. Appl. Phys.*, vol. 65, no. 1, pp. 164–7, 1989.
- [20] E. R. Abraham and E. A. Cornell, "Teflon feedthrough for coupling optical fibers into ultrahigh vacuum systems," *Appl. Optics*, vol. 37, no. 10, p. 1762, 1998.

- [21] J. Butterworth, C. Brome, P. Huffman, C. Mattoni, D. McKinsey, and J. Doyle, “Demountable cryogenic feedthrough for plastic optical fibers,” *Rev. Sci. Instrum.*, vol. 69, no. 10, pp. 3697–3698, 1998.
- [22] T. Albrecht, P. Grutter, D. Rugar, and D. Smith, “Low-temperature force microscope with all-fiber interferometer,” *Ultramicroscopy*, vol. 42-44, no. Part B, pp. 1638–1646, 1992.
- [23] T. Heumier and J. Carlsten, “Detecting mode hopping in semiconductor lasers by monitoring intensity noise,” *IEEE J. Quantum Elect.*, vol. 29, no. 11, pp. 2756–2761, 1993.
- [24] N. Chinone, T. Kuroda, T. Ohtoshi, T. Takahashi, and T. Kajimura, “Mode-hopping noise in index-guided semiconductor lasers and its reduction by saturable absorbers,” *IEEE J. Quantum Elect.*, vol. QE-21, no. 8, pp. 1264–1270, 1985.
- [25] J. L. Hutter and J. Bechhoefer, “Calibration of atomic-force microscope tips,” *Rev. Sci. Instrum.*, vol. 64, no. 7, pp. 1868–1873, 1993.
- [26] T. R. Albrecht, P. Grutter, D. Horne, and D. Rugar, “Frequency-modulation detection using high- q cantilevers for enhanced force microscope sensitivity,” *J. Appl. Phys.*, vol. 69, no. 2, pp. 668–673, 1991.
- [27] U. Dürig, O. Züger, and A. Stalder, “Interaction force detection in scanning probe microscopy - methods and applications,” *J. Appl. Phys.*, vol. 72, no. 5, pp. 1778–1798, 1992.
- [28] W. R. Silveira and J. A. Marohn, “A vertical inertial coarse approach for variable temperature scanned probe microscopy,” *Rev. Sci. Instrum.*, vol. 74, no. 1, pp. 267–269, 2003.
- [29] J. Siegel, J. Witt, N. Venturi, and S. Field, “Compact large-range cryogenic scanner,” *Rev. Sci. Instrum.*, vol. 66, no. 3, pp. 2520–2523, 1995.

CHAPTER 4

CHARGE TRAP EXPERIMENTS

As discussed in Chapters 1, 2, charge trapping plays a central role in the performance of pentacene thin film transistors. The spatial distribution of traps has never been observed directly until this work. As mentioned previously there is circumstantial evidence that the traps are isolated at the grain boundaries. There are theories that indicate a more homogeneous distribution of traps states. The energy distribution, as studied by thermally stimulated current and deep-level transient spectroscopy, is thought to consist of several isolated energies, each with a gaussian distribution [1,2]. These are both bulk techniques and cannot determine the spatial locations corresponding to each of the trap energies. This chapter outlines an electric force microscope experiment that helps answer some of the questions regarding the spatial distribution of traps in a pentacene thin film transistor. This work has been published in *Advanced Materials* [3].

4.1 Sample Description

Bottom-contact pentacene thin film transistors were fabricated with recessed source and drain electrodes according to the procedures outlined in Chap. 2. The substrate geometry is shown in Fig. 4.1(a). The recessed electrodes provided a flat substrate and a constant height film that made electric force microscopy images easier to obtain.

Device substrates were fabricated beginning with a heavily p-doped Si wafer (0.001 – 0.003 Ωcm ; $\langle 100 \rangle$ orientation). A 325 nm-thick thermal oxide was grown as a gate dielectric. Source and drain electrodes were defined using optical photolithography. Prior to evaporating 5 nm of Cr and 70 nm of Au as the source and

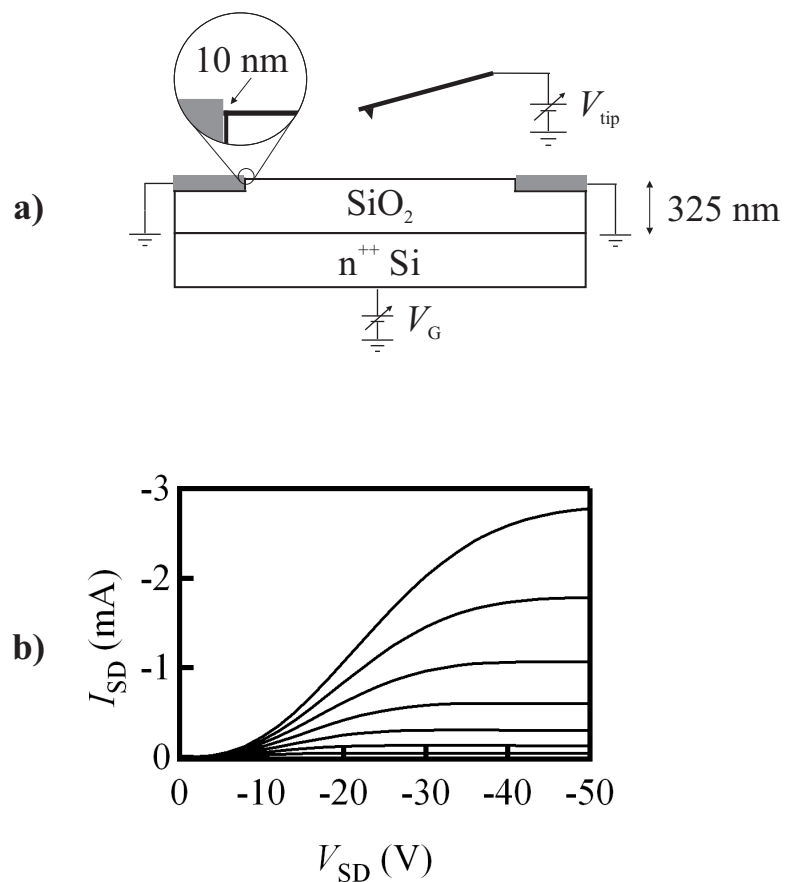


Figure 4.1: Pentacene thin film transistor. a) Schematic of the device substrate ($L = 6.5 \mu\text{m}$ and $W = 20.1 \mu\text{m}$). The zoomed-in feature shows the height difference between the gap and the recessed electrodes. Also shown is a metal coated cantilever for atomic and electric force microscopy. (b) Current-voltage characteristics. Here V_G ranges from 0 V to -50 V in 5 V steps.

drain electrodes, shallow trenches (60 nm) were etched in the SiO₂ to recess the electrodes. Immediately prior to the pentacene deposition, the device substrates were cleaned with acetone and isopropanol. Pentacene from Aldrich was used without further purification. A 50 nm layer of pentacene was thermally evaporated in high vacuum at a rate of 0.1 Å/s with the device substrate fixed at room temperature. The source and drain electrodes were composed of 34 interdigitated fingers with a gap length, L , of 6.5 μm. The resulting total width, W , of the transistor was 20.1 cm.

The current-voltage characteristics are shown in Fig. 4.1(b). The device shows typical transistor behavior with indications of poor contacts. The slow rise in I_{SD} with V_{SD} is an indication of poor contacts. The remaining characteristics are quite normal; the threshold voltage is $V_T \approx -10\text{V}$ and a mobility, calculated in the saturation regime, is $\mu_{\text{sat}} = 2 \times 10^{-2} \text{ cm}^2/\text{Vs}$. These values are typical of a bottom contact device prepared by evaporative deposition onto an untreated SiO₂ substrate [4].

Current voltage measurements were taken with Keithley source meters, model numbers 2400 and 6430. The entire current-voltage data set was taken in approximately 1 minute, with each I_{SD} vs. V_{SD} curve taking 5 – 15 s. Because good saturation is observed in the current-voltage characteristics of Fig. 4.1(b) on the timescale of 5 – 15 s, it can be concluded that the time required to occupy the majority of traps is comparable to this time or shorter. A charging time of 30 s is considered a sufficiently long trap-charging time in the EFM experiments.

A commercial cantilever (model number NSC21, MikroMasch) with a spring constant of $k = 1 \text{ N/m}$, resonant frequency of $f_0 = 24 \text{ kHz}$, and a quality factor of $Q = 10^4$ was employed in the EFM experiments. The motion of the cantilever is

detected using the fiber-optic interferometer described in Sec. 3.6.2. The interferometer operates at 1310 nm, a wavelength well below the bandgap of pentacene. The cantilever is driven at its resonant frequency by using the phase locked loop described in Sec. 3.6.3. The amplitude of the oscillating voltage sent to the piezo is held fixed. This amplitude is adjusted until the cantilever response reaches 15 nm – rms. The resonant frequency of the cantilever is measured with a Stanford Research Systems SR620 frequency counter.

4.2 EFM - Trap Detection Protocol

As described in Sec. 3.2, the presence of charge traps in pentacene is detected as a change in the contact potential. A simplified version is presented here for clarity. The tip-sample interaction is modeled as a parallel plate capacitor of the form metal1/dielectric/vacuum/metal2 (Fig. 4.2). Here “metal1” represents the gate, “metal2” the tip, and “dielectric” the SiO₂. For simplicity, the pentacene is neglected because its thickness is much smaller than that of SiO₂. Trapped charge at the SiO₂/pentacene interface will shift the apparent contact potential difference between metal1 and metal2 by an amount

$$\Delta\phi_{\text{trap}} \approx \frac{\sigma d}{\kappa\epsilon_0} \quad (4.1)$$

where σ is the planar charge trap density, d and κ are the thickness and dielectric constant of the dielectric layer, respectively, and ϵ_0 is the permittivity of free space. For all of the charge trap imaging experiments, the source and drain electrode are grounded. They act only as charge reservoirs for the trap states.

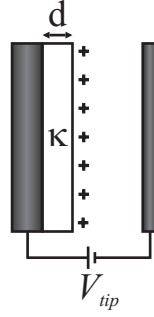


Figure 4.2: Simple model of the tip-sample interaction (see text for explanation). The + represents trapped charge.

4.3 Trap Imaging I

The first experiment follows the procedure sketched in Fig. 4.3. Fig. 4.3 (a) shows a band diagram of the gate electrode on the left and the pentacene thin film on the right. Three trap states are shown with energies below the Fermi level, ϵ_F , which have a narrow gaussian distribution. This diagram is purely a conceptualization. Because each of these levels is below the Fermi level, they are occupied by an electron and are neutral. As the gate voltage is decreased, the states in the pentacene film will be dragged upward along with the gate voltage (the convention used here is that a decrease in potential causes the bands to go up). When one of the trap states crosses the Fermi level, the electron will fall to the HOMO leaving the trap state occupied by a positively charged trap (see Fig. 4.3 (b)). As the gate voltage is lowered further (see Fig. 4.3 (c)), more traps states become occupied. Simultaneously, there is an accumulation of holes in the HOMO at the pentacene/insulator interface.

The gate voltage is decreased in small increments and an EFM image is taken at each gate voltage. When the trap states become occupied, the expectation is that the image will be dimpled with patches of charge corresponding to the

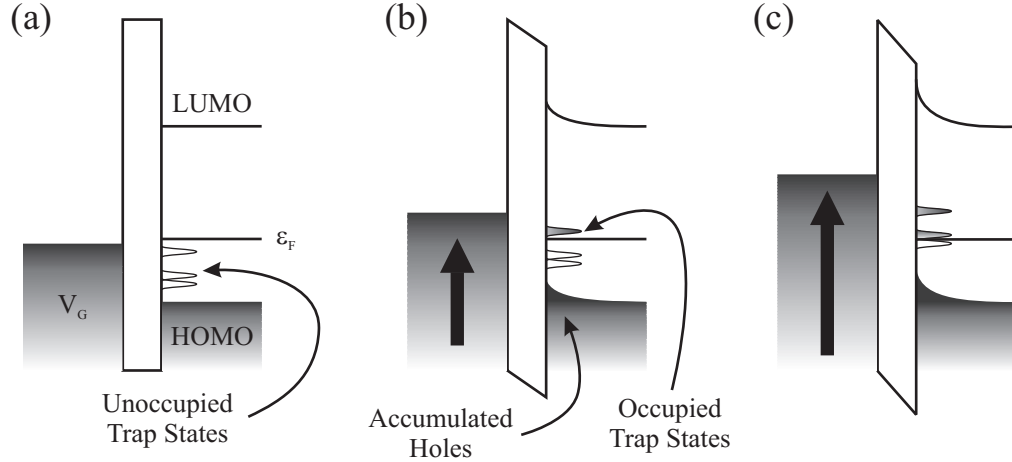


Figure 4.3: (a) The energy level diagram of the gate, SiO₂ and the pentacene semiconductor showing three unoccupied trap states. (b) A trap becoming occupied by decreasing the gate voltage. (c) Deeper trap state becoming occupied with further increase of the gate voltage.

trap locations. This, however, was *not* observed. A series of EFM frequency shift images, where the gate voltage is lowered in small increments, are shown in Fig. 4.4. The contrast observed in these images is not due to potential but to the topography of the pentacene thin film. There is *no* observable increase in the charge density due to trapped charge.

The flaw with this method of observing the charge traps is that it ignores the effect of the accumulation layer. The consequence of the accumulation layer is illustrated in Fig. 4.5

With source and drain grounded, we measured ϕ as a function of V_G (Fig. 4.5). If the tip and gate are behaving as a parallel plate capacitor, then ϕ should track V_G with a slope of one. This is indeed true when $V_G > 0$. When V_G is negative and below the threshold voltage ($V_T \approx -8\text{V}$), however, charge accumulates at the pentacene/SiO₂ interface and shields the tip from the gate, resulting in $\phi \approx 0$.

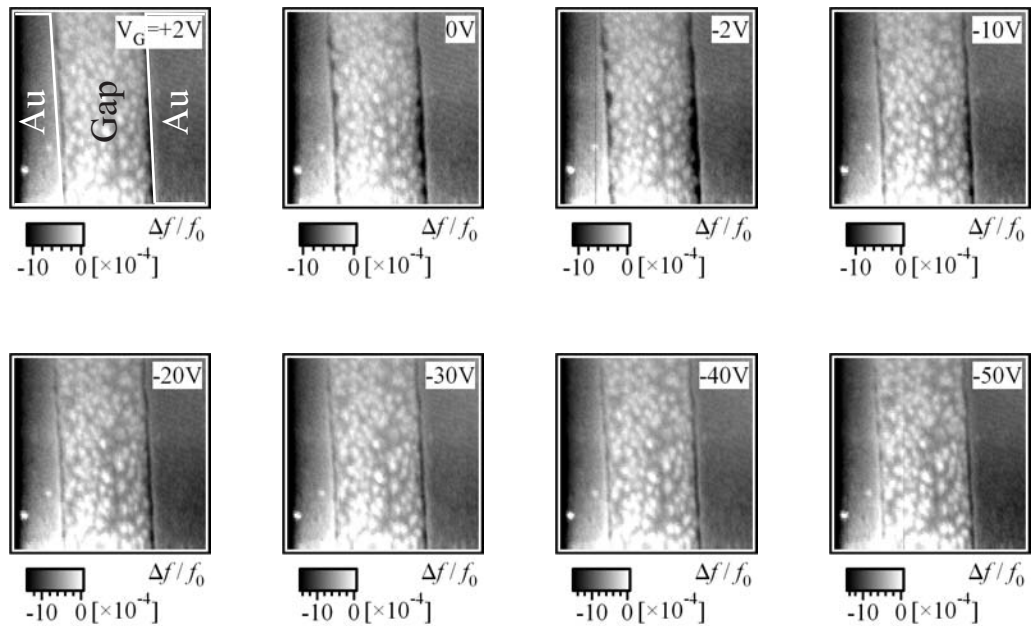


Figure 4.4: EFM images of the transistor gap using imaging protocol I with V_G ranging from +2 V to -50 V . There is no *apparent* increase in the charge density inside the device.

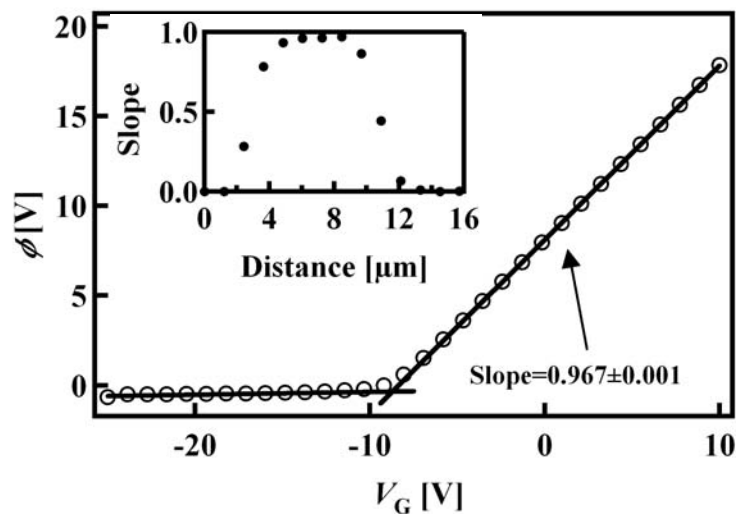


Figure 4.5: $\phi(x)$ versus V_G . The inset shows the slope at positive gate bias versus the tip position across the device gap.

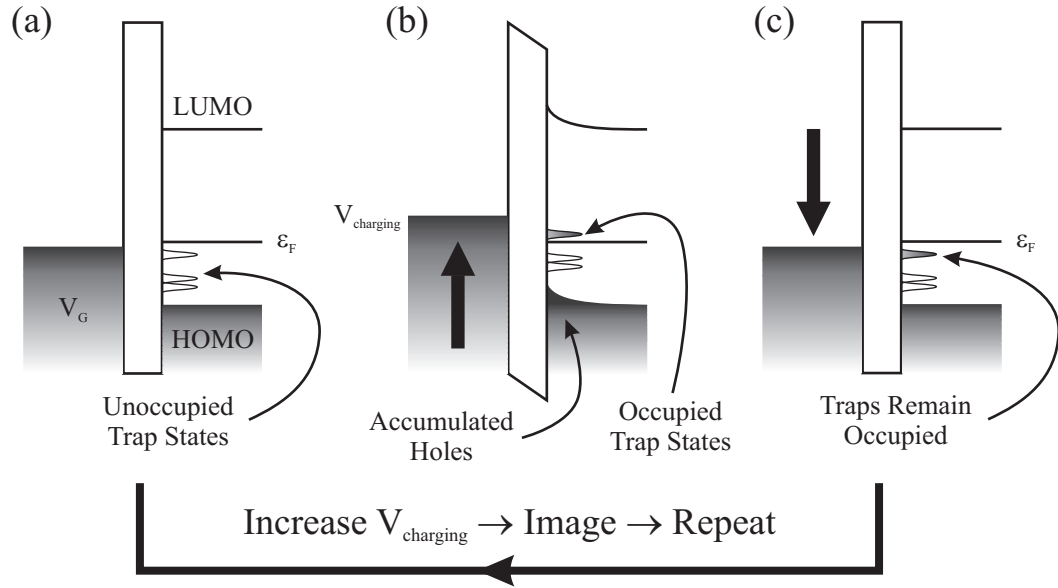


Figure 4.6: (a) Energy level diagram. (b) The traps are charged by increasing the gate voltage. (c) Gate voltage is lowered back to zero and the mobile, accumulated holes leave the device, but the trap charge remains.

(This can alternatively be explained using a model similar to that of Fig. 4.2, with “metal” now representing the pentacene accumulation layer. Since the traps reside in or near the accumulation layer, $d \approx 0$, and we expect $\Delta\phi_{\text{trap}} \approx 0$.) It is interesting to note that in Fig. 4.5, that the transistor threshold voltage is measured *locally*.

4.4 Trap Imaging II

The shielding by the mobile, accumulated holes masks any effect on the electrostatic potential or capacitance due to trapped holes and therefore an alternate approach to image traps was devised. Fig. 4.6 details the slight variation to the imagine protocol of Fig. 4.3. After setting gate voltage negative for 30 s to charge

the traps, the gate voltage was returned to zero before imaging. The gate voltage used to charge the traps is referred to as V_{charging} . Returning the gate voltage to zero has the affect of chasing out the mobile, accumulated holes, leaving only the trapped charge. The trapped charges are out of equilibrium and remain in the transistor channel for tens of minutes – enough time to collect an image. A series of images is shown in Fig. 4.7 where V_{charging} was decreased for each image. In contrast with Fig. 4.4, these images show a dramatic evolution in the cantilever frequency variation as V_{charging} is increased.

The image contrast in Fig. 4.7 arises predominantly from variations in contact potential. To determine this, a linescan (described in Sec. 3.7) is measured, finding ϕ and C'' along a representative line in the transistor gap (Fig. 4.8(a-b)). The location of this line is indicated in Fig. 4.7. Using Eq. 3.114 it is estimated that 85% of the variation in Δf observed along the line is due to the variation in contact potential. This can be seen qualitatively in Fig. 4.8(c) where Δf has been constructed from the measured $\phi(x)$ and $C''(x)$; the observed frequency tracks ϕ very closely. It is then justified to treat C'' as a constant and use Eq. 3.115 to compute the local contact potential ϕ from the measured cantilever frequency. The variation in ϕ is attributed to long-lived traps, since the observed variation in ϕ across the transistor gap is 1) less than 50 mV before the gate voltage is increased above the threshold voltage, 2) increases with V_{charging} , and 3) disappears after approximately 24 hours.

4.5 Trap Density

The trap density can be calculated *quantitatively* using Eqs. 3.114 - 4.1, the known k , κ , d , and V_{tip} , and the measured Δf , f_0 , and C'' . Fig. 4.9(b) displays

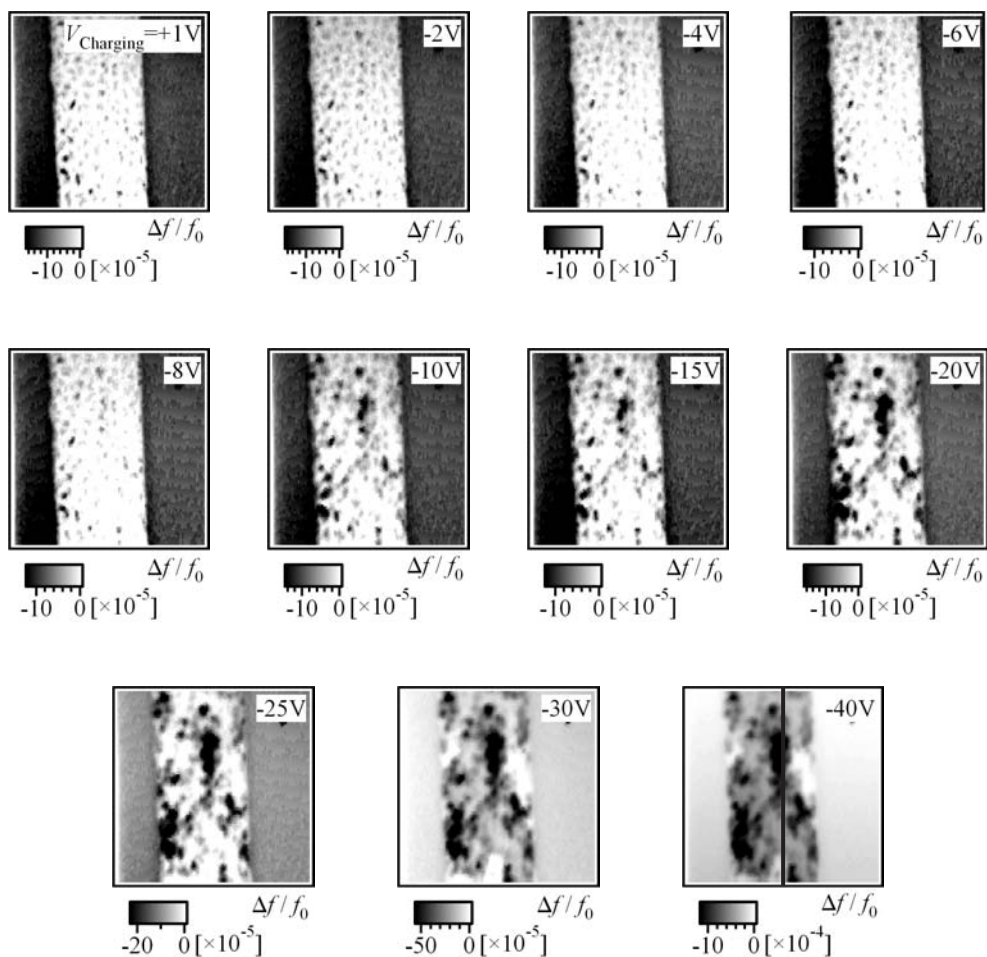


Figure 4.7: EFM images of charge trapping using imaging protocol II with V_{charging} ranging from +1 V to -40 V. The charge density increases dramatically after the threshold voltage ($V_T \sim -8$ V)

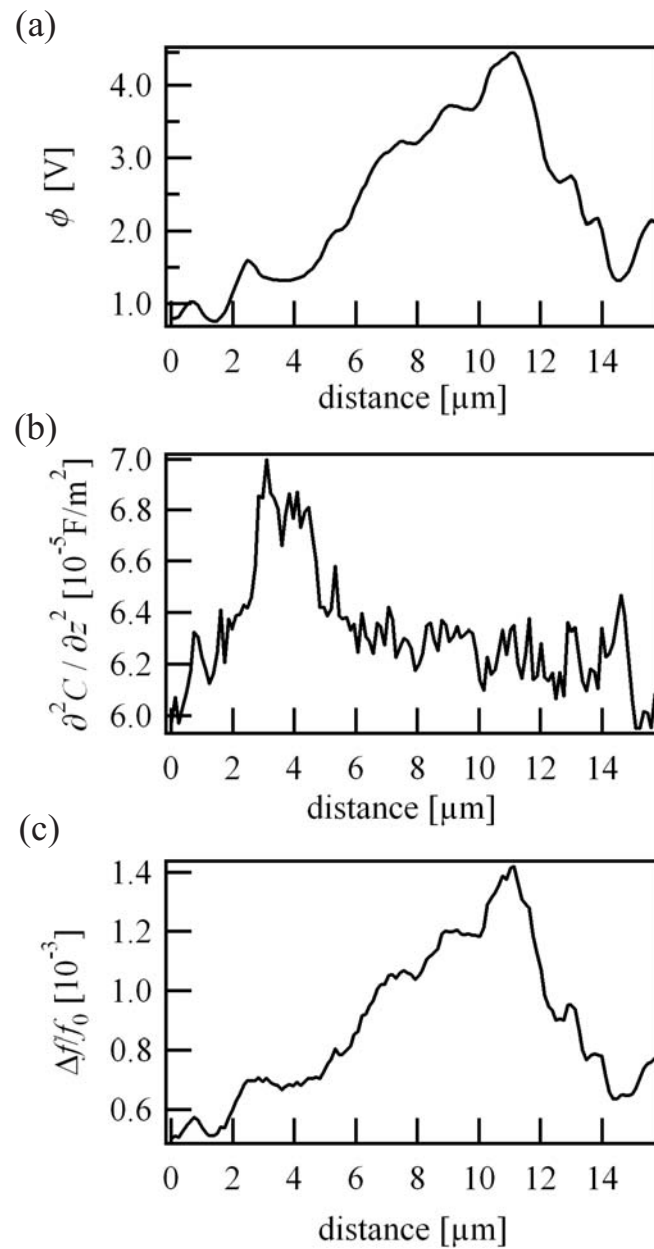


Figure 4.8: (a) The electrostatic potential, ϕ , and (b) the capacitance derivative, C'' along the representative line in Fig. 4.7. (c) The frequency shift calculated from ϕ and C'' using Eq. 3.114

histograms of trap density at various charging voltages. This data is obtained by selecting the points inside the transistor gap and making a histogram of the charge trap density of those points. The sharp peak in the histograms is from the metal electrode which is used to define the frequency-zero point for all the images, which can vary from image-to-image because of drift in the tip-sample separation. The distributions for the metal electrodes arises from capacitance variation, not trap density variation. The mean trap density at $V_{\text{charging}} = -30\text{V}$ is 1.6×10^{11} holes/cm², or about one hole per 2.5×10^3 pentacene molecules (assuming that the accumulation layer is one monolayer thick). Using an effective tip diameter of approximately 300 nm (the apparent EFM imaging resolution as estimated by the smallest feature seen in Figs. 4.7), the contact potential shift is calculated to be due to as few as ~ 3 trapped holes underneath the cantilever tip.

Interestingly, as the charging voltage increases, the trap distribution evolves from a Gaussian shape to a highly asymmetric distribution with a long exponential-like tail – a possible consequence of sites trapping charge at different rates. While a Gaussian distribution can arise from statistical fluctuations in the filling of a single well-defined trap energy level, an asymmetric distribution cannot. For a well-defined trap energy level, increasing the charging voltage would only increase the proportion of occupied trapped states. This would move the gaussian distribution to the left, but would not change its shape. The asymmetric distribution observed suggests an exponential density of trap energies, in qualitative agreement with transport studies [5–7].

Figures 4.7 and 4.9 are the central result of this experiment. The long-lived traps evident in Fig. 4.7 at higher charging voltages are clearly *not* homogeneously distributed in space, and large variations in trap concentration are observed on

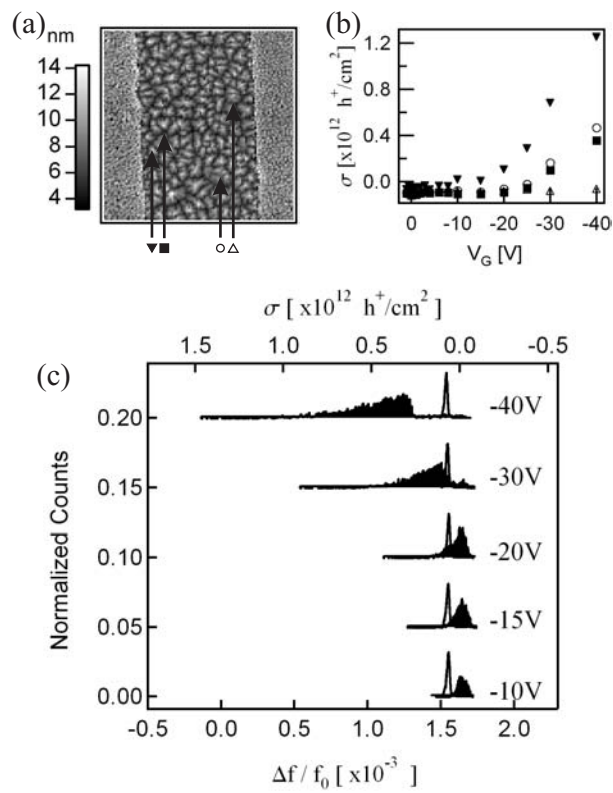


Figure 4.9: (a) Selected positions in the pentacene topography. (b) Trap density versus charging voltage at various positions in the pentacene device and (c) histograms of trap density at various charging voltages.

	Bulk Traps?	Grain Boundary Traps?
Reorganization Energy	<u>Unlikely</u>	<u>Possible</u> Chemical reactions which cause structural changes to the pentacene molecule are more likely at grain boundaries.
Polarization Energy	<u>Unlikely</u>	<u>Possible</u> Polarization energy is altered at interfaces.
Chemical Impurities	<u>Possible</u> Impurities present in the pentacene prior to deposition can introduce trapping sites.	<u>Possible</u> Chemical reactions involving the addition of H or O are more likely at the grain boundaries.

Figure 4.10: Summary of possible trapping theories and their association with either grain boundaries or bulk effects.

a ≥ 300 nm length scale. Fig. 4.9 (a) displays the trap density σ versus V_{charging} at selected points in the transistor gap. While trap density increases as a function of V_{charging} at most locations in pentacene, the amount of increase is simply not correlated with the apparent location of the grain boundaries, as generally supposed [7–9].

The findings can be used to eliminate a number of proposed trap candidates (summarized in Fig 4.10). Trapping at the grain boundaries near the buried pentacene/SiO₂ interface is not necessarily inconsistent with the data, since the grain boundaries at the buried interface need not correspond to the grain boundaries identified by AFM topography [10]. Nevertheless, trapping at buried grain boundaries is an extremely unlikely possibility since the observed charge traps simply do not appear to follow the shape expected of grain boundaries. Further electric force microscope studies with thinner pentacene samples will allow a direct connection, if it exists, between grain boundaries and charge traps.

The long-lived traps observed here cannot be due to bulk trapping at ran-

domly distributed chemical defects. Bulk traps should have well-defined energies, inconsistent with the observed trap concentration statistics. Above a threshold, trap concentration rises approximately linearly in voltage, consistent with a polaron (cation) trapping mechanism. Further studies will be needed to determine if a bipolaron (dication) trapping mechanism is present in these devices, as has been proposed by Northrup and Chabinye for hydrogen and oxygen related defects in pentacene [11, 12]. Varying the charging time might yield information about whether the holes trap singly or in pairs. The effect of a bipolaron mechanism can be observed through the rate of change of the source-drain current versus time. For a bipolaron mechanism, the current decay depends on the number of mobile holes squared, i.e. $dN_{trapped}/dt \propto N_h^2$, where $N_{trapped}$ and N_h are the number of trapped charges and the number of free holes, respectively.

Knipp *et al.* have found that trap depth is different for pentacene transistors fabricated on a rough versus a smooth silicon nitride dielectric, suggesting that traps are associated with perturbations in pentacene energetics arising from the dielectric [6]. It is tempting to draw a similar conclusion from the data for the pentacene/SiO₂ interface, because the observations imply that there are sites in polycrystalline pentacene near the SiO₂ interface *in addition* to grain boundaries that act as traps. Surprisingly, however, the ~ 300 nm length scale associated with charge trap domains in the images of Fig. 4.7 are much larger than the length scales associated with either pentacene topography (Fig. 4.9(a)) or SiO₂ topography (data not shown). It is hard to understand why the observed trapping domains are so large, if the dielectric/organic interface is determining the trap energies. Establishing a definitive connection between local chemical structure at the buried pentacene/dielectric interface will be challenging, since essentially no analytical

tools exist for determining local structure at a buried solid-solid interface. As a next step, it will be interesting to image traps in pentacene deposited on various dielectrics.

In conclusion, charge traps in polycrystalline pentacene are found to be distributed inhomogeneously but do not appear to be associated with grain boundaries. Using frequency-shift electric force microscopy to image traps is quite general and requires no assumptions about charge transport in either the bulk or at the contacts. In this study, traps which fill quickly (< 30 s) and empty slowly (> 20 min) are imaged. It is reasonable that 30 s is long enough to populate the majority of trap sites, since the current-voltage characteristics taken on this timescale show good saturation behavior, and the trap densities measured are comparable to what has been estimated by others [6]. While the implementation described here is naturally suited to imaging long-lived traps (≥ 20 min), studying shorter lifetime traps (≤ 1 s) should be possible by following the cantilever frequency as a function of time, point by point.

References

- [1] T. Sakurai, “Thermally stimulated current in the absence of optical-excitation in the annealing of tetracene and pentacene films,” *Phys. Rev. B*, vol. 40, no. 17, pp. 11817–11821, 1989.
- [2] Y. S. Yang, S. H. Kim, J. I. Lee, H. Y. Chu, L. M. Do, H. Lee, J. Oh, T. Zyung, M. K. Ryu, and M. S. Jang, “Deep-level defect characteristics in pentacene organic thin films,” *Appl. Phys. Lett.*, vol. 80, no. 9, pp. 1595–1597, 2002.
- [3] E. M. Muller and J. A. Marohn, “Microscopic evidence for spatially inhomogeneous charge trapping in pentacene,” *Adv. Mater.*, vol. 17, no. 11, pp. 1410–1414, 2005.
- [4] Y. J. Zhang, J. R. Petta, S. Ambily, Y. L. Shen, D. C. Ralph, and G. G. Malliaras, “30 nm channel length pentacene transistors,” *Adv. Mater.*, vol. 15, no. 19, pp. 1632–1635, 2003.

- [5] A. R. Völkel, R. A. Street, and D. Knipp, “Carrier transport and density of state distributions in pentacene transistors,” *Phys. Rev. B*, vol. 66, no. 19, pp. 347–355, 2002.
- [6] D. Knipp, R. A. Street, A. Volkel, and J. Ho, “Pentacene thin film transistors on inorganic dielectrics: morphology, structural properties, and electronic transport,” *J. Appl. Phys.*, vol. 93, no. 1, pp. 347–355, 2003.
- [7] S. Verlaak, V. Arkhipov, and P. Heremans, “Modeling of transport in polycrystalline organic semiconductor films,” *Appl. Phys. Lett.*, vol. 82, no. 5, pp. 745–747, 2003.
- [8] R. A. Street, D. Knipp, and A. R. Volkel, “Hole transport in polycrystalline pentacene transistors,” *Appl. Phys. Lett.*, vol. 80, no. 9, pp. 1658–1660, 2002.
- [9] D. Knipp, R. A. Street, and A. R. Volkel, “Morphology and electronic transport of polycrystalline pentacene thin-film transistors,” *Appl. Phys. Lett.*, vol. 82, no. 22, pp. 3907–3909, 2003.
- [10] K. P. Puntambekar, P. V. Pesavento, and C. D. Frisbie, “Surface potential profiling and contact resistance measurements on operating pentacene thin-film transistors by kelvin probe force microscopy,” *Appl. Phys. Lett.*, vol. 83, no. 26, pp. 5539–5541, 2003.
- [11] J. E. Northrup and M. L. Chabiny, “Gap states in organic semiconductors: hydrogen- and oxygen-induced states in pentacene,” *Phys. Rev. B*, vol. 68, no. 4, p. 041202, 2003.
- [12] R. A. Street, A. Salleo, and M. L. Chabiny, “Bipolaron mechanism for bias-stress effects in polymer transistors,” *Phys. Rev. B*, vol. 68, no. 8, p. 085316, 2003.

CHAPTER 5
ULTRATHIN PENTACENE TRANSISTORS AND FUTURE
DIRECTIONS

Simplifying the topography of the polycrystalline pentacene could aid in determining the role of the grain boundaries in trapping. Measuring the trap density at a single isolated grain boundary would be ideal. Performing this type of measurement using EFM has several requirements. First, the island size (i.e. the size of the grains) must be much larger than the resolution of the electric force microscope. This requires grains of at least $2 - 5 \mu\text{m}$ in diameter, which is slightly higher than was grown for the trap imaging experiment. Second, the pentacene film should only consist of 1-2 monolayers. Transistors with ultrathin films of pentacene have recently been fabricated [1–4]. Third, the transistor gap would have to be small enough to image with the electric force microscope. This chapter outlines the steps taken in attempt to meet these requirements.

The improvement of the grain sizes was achieved by decreasing the pentacene deposition rate to $0.03 - 0.05 \text{ \AA/s}$ and further cleaning the substrate surface. Prior to pentacene deposition, the substrate is MOS cleaned at the Cornell Nanofabrication Facility. Because metals are not compatible with the MOS clean chemicals, the bottom contact geometry had to be abandoned. The procedure to make top contacts is outlined later. Prior to the MOS clean, the substrate is cleaned with isopropanol and acetone. At this point, water would bead up on the surface of the substrate indicating a hydrophobic surface. After the MOS clean, water does not bead up, suggesting a hydrophilic surface – a quick indication that the MOS clean has been effective.

The cleaned substrates were taken immediately to the deposition chamber and

pumped down to a vacuum of 10^{-6} Torr. The samples are mounted on a heater stage. They are heated to 180°C for one hour and allowed to cool to 60°C . The cooling takes about 6 hours because they are in vacuum. The heating of the sample dries off the water and any organics that remain on the sample. The deposition is performed, at a rate of $0.03 - 0.05\text{\AA}/\text{s}$, with the sample temperature held fixed at 60°C . Depositing at an elevated temperature provides the pentacene molecules with more kinetic energy allowing them to move around more on the surface before sticking. An atomic force microscope image of representative samples are shown in Fig. 5.1. Fig. 5.1(a) shows a film that has approximately 80% coverage with island sizes around $2\ \mu\text{m}$. Fig. 5.1(b) shows a near-complete first monolayer of pentacene with grain sizes of about $4\ \mu\text{m}$. The beginning of the second layer can also be seen in Fig. 5.1(b). These films demonstrate that the grains can be made large enough for easy measurement with the electric force microscope.

The next requirement for making a transistor with these thin films was the largest challenge of this experiment. Because the cleaning process eliminated the option of using the bottom contact configuration, shadow masks had to be designed to define top contacts. The shadow mask had to produce contacts that are separated by a distance that is within the scan range of the electric force microscope (i.e. less than $\sim 30\ \mu\text{m}$). They also had to produce contacts that are wide enough that the sample could be aligned to the cantilever by hand looking through a microscope. The luxury of the interdigitated contacts is not feasible in the top contact configuration, so the sample must be aligned by hand. The contacts were designed to produce lengths of $10 - 60\ \mu\text{m}$ with a width of $750\ \mu\text{m}$.

The design was simply to etch two holes separated by a thin beam in a silicon wafer (see Fig. 5.2). The beam has a width that is equal to the transistor gap

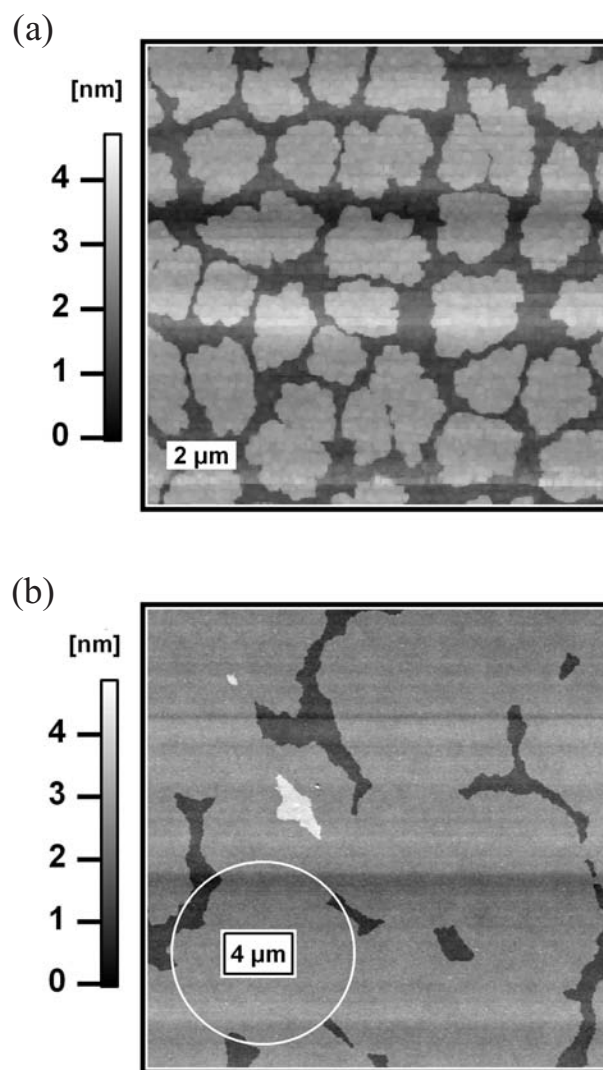


Figure 5.1: (a) Pentacene islands with a coverage of 80% and (b) with a near-complete monolayer.

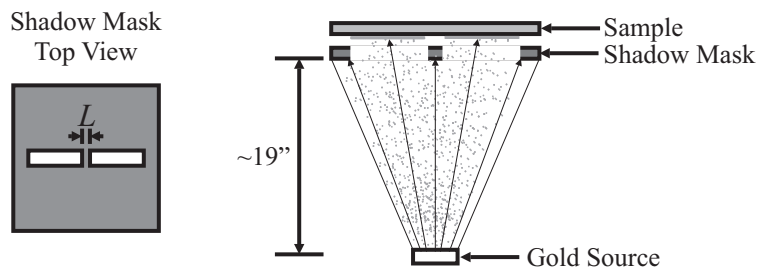


Figure 5.2: Schematic of the shadow mask design and the arrangement in the thermal evaporator.

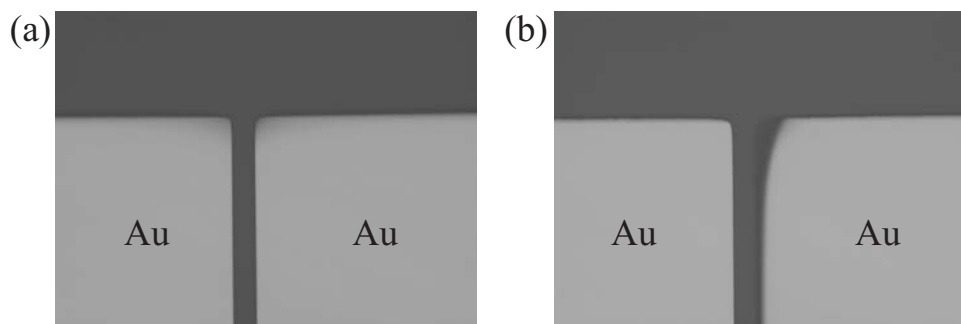


Figure 5.3: (a) The gold contacts produced from the shadow mask and (b) gold contacts where there is an angular misalignment of the mask and evaporation source

length. The wafer was clamped to the sample substrate containing the pentacene film and gold was evaporated through the shadow mask. Fig 5.3(a) shows one edge of the resulting contacts with a gap width of 20 μm .

It is important to align the shadow mask directly above the gold evaporation source. A horizontal mismatch of just two inches from directly above the evaporation source will produce the rounded-off corners seen in Fig 5.3(b).

Unfortunately, transistors made with the shadow mask on ultrathin films of pentacene did not work. Transistors with films in the range of 25 nm thick (about 17 monolayer) were successfully fabricated. The current voltage characteristics are

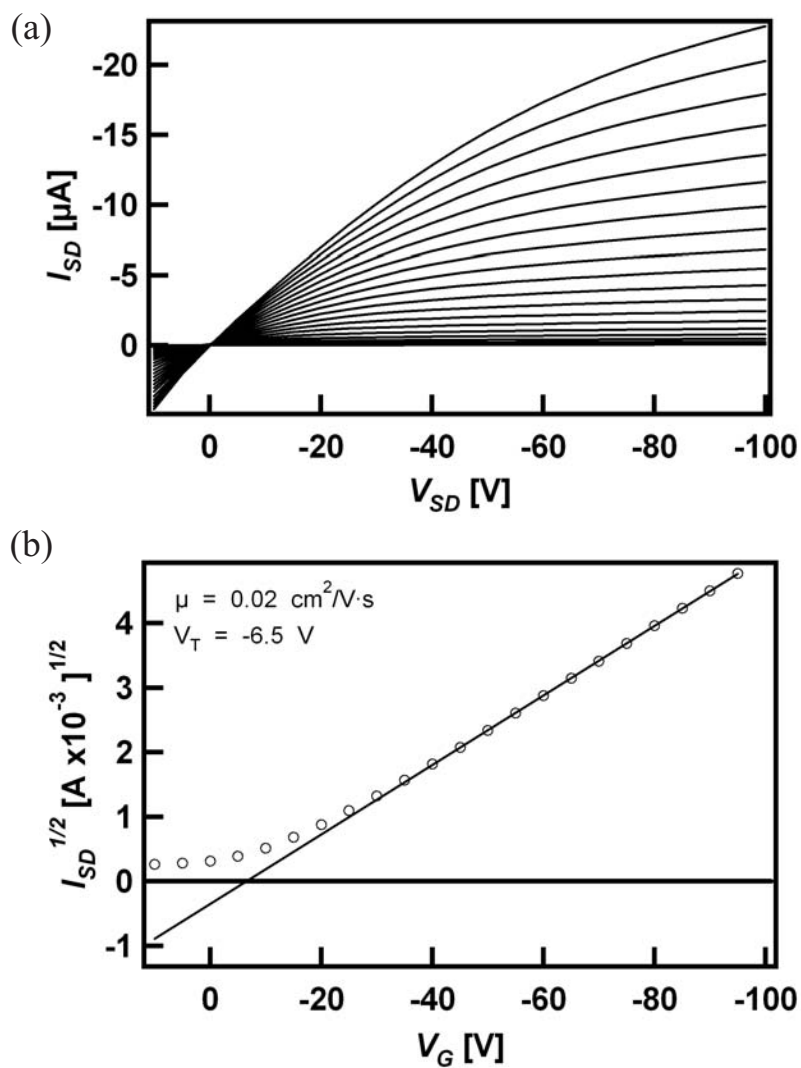


Figure 5.4: (a) Current-voltage characteristics for a pentacene(25nm thick) thin-film transistor with $W = 500\mu\text{m}$, $L = 30\mu\text{m}$ and an oxide thickness of $T = 340\text{nm}$. The gate voltage is goes from +10 to -100V in -5V steps. (b) The square root of the source-drain current at saturation versus the gate voltage. The mobility and threshold voltage is calculated from the saturation regime.

shown in Fig. 5.4. Fig. 5.4(a) shows the current voltage characteristics of a 25nm thick pentacene transistor. The mobility was calculated to be $0.02\text{cm}^2/\text{Vs}$ in the saturation regime, see Fig. 5.4(b). There are a couple of features that distinguish the top contact device from the bottom contact device. First, there is the notable difference in quality of the contacts based on the sharp initial rise of the source-drain current. And, second, the device does not reach saturation at the high gate voltages.

Transistors with gap lengths of $20\ \mu\text{m}$ were fabricated and met the requirement of being smaller than the scan range of the electric force microscope; however, the yield was small (less than 50%). Transistors with a gap lengths of $10\ \mu\text{m}$ were never successfully fabricated. All devices with this length were electrically shorted.

The fabrication of transistors that incorporate *both* ultrathin pentacene films and top contact transistors was elusive. Successful implementation and measurement of this type of transistor has the potential to answer many of the outstanding questions regarding the spatial characteristics of charge trapping in pentacene thin films. The thicker pentacene thin films investigated in Chap. 4 contained layers of pentacene that masked the grain boundaries of the first few layers. These ultrathin films would enable correlation between the spatial distribution of the charge trapping with the grains directly participating in the trapping.

The electric force microscope has proven to be an effective tool for measuring charge trapping in pentacene thin-film transistors. The spatial distribution of the charge trapping in pentacene has been shown to be inhomogeneous and not associated with the polycrystalline grain boundaries. Future EFM studies on ultrathin films to probe not only the spatial distribution of trapping, but also the energetic distribution could provide much details that could compliment the vast amount of

information already known about pentacene thin film transistors.

References

- [1] R. Ruiz, A. Papadimitratos, A. Mayer, and G. Malliaras, “Thickness dependence of mobility in pentacene transistors,” *Adv. Mater.*, *in press*, 2005.
- [2] S. Y. Jung and Z. Yao, “Organic field-effect transistors with single and double pentacene layers,” *Appl. Phys. Lett.*, vol. 86, no. 8, 2005.
- [3] M. Daraktchiev, A. von Muhlenen, F. Nuesch, M. Schaer, M. Brinkmann, M. N. Bussac, and L. Zuppiroli, “Ultrathin organic transistors on oxide surfaces,” *New J. Phys.*, vol. 7, 2005.
- [4] R. Ruiz, D. Choudhary, B. Nickel, T. Toccoli, K. C. Chang, A. C. Mayer, P. Clancy, J. M. Blakely, R. L. Headrick, S. Iannotta, and G. G. Malliaras, “Pentacene thin film growth,” *Chem. Mater.*, vol. 16, no. 23, pp. 4497–4508, 2004.

APPENDIX A

BOTTOM CONTACT RECIPE

Bottom contact devices are made using the following recipe. The items in bold are the actual procedures; they are followed by an short explanation or comment on the procedure.

- Layer 1
 1. **Liquid prime with P-20 (20% HMDS) primer. Apply over entire wafer, allow to remain 10 seconds, then spin dry at 4000 rpm for 30 seconds.** The liquid primer prepares the surface for better adhesion of the resist.
 2. **Spin S1813 resist at 4000 rpm for 30 seconds (gives about 1.6 μm thickness of resist.** Two pipets of resist is poured in the center of the wafer and spun as soon as possible. Not spinning the resist soon enough can dissolve the primer (CNF staff recommendation). Bubbles should be avoided.
 3. **Bake on hot plate at 115° Celsius for 90 seconds.** This is typically called a “soft bake” and is used to evaporate any remaining solvent in the resist.
 4. **Expose for 6 seconds on the EV620 contact aligner using only the mask defining the gate electrodes. Use the soft contact recipe.** The exposure time can vary depending on the current output of the UV lamp in the EV620. If your features are not pushing the limit of contact lithography (which is about 2 μm , then the exposure can be slightly longer. 10s is not unusual).

5. **Develop in 300 MIF for 60 seconds. Rinse thoroughly in DI water and dry with N₂.** CNF recently made available a tool that can do automatic developing. Just choose the right recipe and it will develop, rinse and dry. The resist will be washed away in any place where it was exposed to UV light from the EV620.
 6. **(optional) Hard bake for 60 seconds at 115°C, or 20-30 minutes in oven.** This step strengthens the resist and increases its selectivity in the etch processes.
 7. **Etch oxide on Oxford 80 RIE using the CHF₃/O₂ recipe.** This recipe etches at roughly 25 nm/min and has a etch ratio of 2:1 with resist.
 8. **Etch silicon on Oxford 80 RIE using the nitride CF₄ recipe**
This recipe etches roughly at 40 nm/min.
 9. **Strip resist with 1165 hot bath for 10 minutes, rinse thoroughly in DI water and dry with N₂.**
- Layer 2
 1. **Liquid prime with P-20 (20% HMDS) primer. Apply over entire wafer, allow to remain 10 seconds, then spin dry at 4000 rpm for 30 seconds.**
 2. **Spin S1813 resist at 4000 rpm for 30 seconds (gives about 1.6µm thickness of resist.)**
 3. **Bake on hot plate at 115°C for 90 seconds.**
 4. **Expose for 6 seconds on the EV620 contact aligner using the**

mask defining the source drain and gate electrodes. Use the soft contact recipe.

5. **Bake in the YES oven using Ammonia (NH₃).** This is process 2 which takes about 90 minutes. This is part of the image reversal step.
6. **Flood expose on the HTG contact aligner for 60 seconds (no mask).** This step completes the image reversal.
7. **Develop in MF 321 for 60 seconds. Rinse thoroughly in DI water and dry with N₂.**
8. **Descum for 5 minutes in the Branson barrel etcher.**
9. (optional - for recessed electrodes) **Etch oxide in Oxford 80 RIE using the CHF₃/O₂ recipe to a depth equal to how thick the metal electrodes will be.** This recipe etches at roughly 25 nm/min and has a etch ratio of 2:1 with resist.
10. **Evaporate 5 nm of chrome as an adhesion layer and 50nm of gold.** This can be done with either e-beam or thermal evaporation and a typical deposition rate is 1 Å/s.
11. **Strip resist in acetone for at least 4 hours.** May require overnight to remove all the gold. Rinse thoroughly in DI water and dry with N₂.

APPENDIX B
SHADOW MASK RECIPE

The shadow masks are fabricated using the following recipe.

1. **Start with a wafer that has 1 μm of thermal oxide.** The oxide on the bottom of the wafer will act as an etch stop for the deep etching step. The oxide on the top of the wafer is used for an etch mask.
2. **Deposit about 1 μm of PECVD oxide on the top of the wafer using the GSI.** This oxide also is part of the etch mask.
3. **Liquid prime with P-20 (20% HMDS) primer. Apply over entire wafer, allow to remain 10 seconds, then spin dry at 4000 rpm for 30 seconds.** The liquid primer prepares the surface for better adhesion of the resist.
4. **Spin S1813 resist at 4000 rpm for 30 seconds.** This results in about 1.6 μm thickness of resist.
5. **Bake on hot plate at 115°C for 90 seconds.** This is typically called a “soft bake” and is used to evaporate any remaining solvent in the resist.
6. **Expose for 6 seconds on the EV620 contact aligner using the shadow-mask mask.** Use the soft contact recipe.
7. **Develop in 300 MIF for 60 seconds. Rinse thoroughly in DI water and dry with N_2 .**
8. **(optional) Hard bake for 60 seconds at 115°C, or 20-30 minutes in oven.**

9. **Etch oxide on Oxford 80 RIE using the CHF_3/O_2 recipe.** This recipe etches at roughly 25 nm/min and has a etch ratio of 2:1 with resist. Leave any remaining resist on the wafer.

10. **Etch silicon in Uniaxis 770 using the “1thru” recipe.** The 1thru recipe etches Si at a rate of 2 $\mu\text{m}/\text{min}$. It etches: Resist at 35-40 nm/min, thermal oxide at 6 nm/min, and PECVD oxide at 11 – 12 nm/min. This step takes about 4 hours to complete. It is good to check the thickness near the end of the process using the profilometer. The time could be shortened by starting with a thinner wafer ($\sim 300 \mu\text{m}$ thick instead of a standard 500 μm thick wafer).